RESEARCH ON LIGHT HARVESTING LAYERS OF METAL HALIDE SOLAR CELLS

メタルハライド太陽電池の光吸収層に関する研究

GRADUATE SCHOOL OF LIFE SCIENCE AND SYSTEMS ENGINEERING
KYUSHU INSTITUTE OF TECHNOLOGY

A DISSERTATION
FOR THE DEGREE OF DOCTOR OF PHILOSOPHY

ZHAOSHENG HU

ENROLLMENT NO: 15899034

SUPERVISOR
PROFESSOR SHUZI HAYASE

Abstract

Metal halide material is the most promising semiconductor for photovoltaics. However, some serious issues on the solar cells have been pointed out. One is the expensive transparent–conductive oxide layered (TCO) glass and the other is toxic lead whose use is limited. In this thesis, studies are focused on the light harvesting layer with three aspects to try to remove expensive TCO layer, and reduce or replace Pb in the active layer in conventional SCs.

Firstly, efficient TCO-less back-contacted perovskite solar cells is developed to remove TCO layer. The cell is composed of glass substrate/ mesoporous TiO_2-PVK/porous-Ti (bottom electrode) & PVK/ ZrO_2-PVK nanocomposite/Gold (top electrode). Up to 3.9 % efficiency is obtained. The Ti with the native oxide on the surface enables the separation of the generated electron-hole pairs and the selective collection of the electrons. Meanwhile, the filled perovskite crystals inside porous pave the way to transport holes and then, collected by the gold top-electrode.

Secondly, in order to make perovskite film thin, silver-gold hetero-dimer is embedded in the active layer of solar cell, which can lead to excellent absorption because of the plasmon intercoupling effect. The incorporating random gold-silver hetero-dimer (diameter: 80 nm, gap-distance: 25 nm) in a 150 nm perovskite layer gives an excellent absorption, which equals the absorption for a common 350 nm perovskite film. These results show the possibility of reducing the light harvesting layer, especially to reduce the amount of toxic lead in perovskite-based devices.

At last, lead-based material is completely replaced with non-toxic bismuth based metal halide semiconductor. And we provide a novel solution-proceed preparation method by using HI assisted DMA solvent to completely dissolve BiI_3 powders. Meanwhile, solvent vapor annealing (SVA) with Tributyl phosphate (TBP) yields high quality, well arranged crystals of copper bismuth iodide. The high vapor pressure of TBP enables the whole low-temperature film preparation. The large grain size prepared from high precursor concentration enlarges the photoluminescence life time longer. 0.8 % efficiency is reported.

Table of Contents

1. Introduction

The driving force behind our rapid development of modern civilization strongly depends on the conversion of energy on earth, which is also regarded as the only universal currency. Humans have to rely on a series of energy conversion, including the conversion of oil to heat, electricity and photosynthesis, which convert solar energy into oxygen, biomass and so on. However, the increase of global population and industrialization lead to the exhaustive exploitation of the nonrenewable energy resources such as oil, carbon, coal, petroleum and natural gas, which face serious challenge. The estimated amount of the crude oil reaches more than 135 billion tons since 1850s the first year to start commercial drilling. Moreover, according to Intergovemment Panel on Climate Change (IPCC) report, the global warming by burning fossil fuels, carbons have increased the average temperature from 0.32 ^{0}C to 1.71 ^{0}C. Future climate will cause harmful effects such as sea level rising and deserts expanding. Therefore, some of these energy supplements have to be replaced with renewable energy sources, which are eco-friendly to environment. Solar cells are the most promising energy source, which directly convert solar energy from sun into electricity via the photovoltaic effect. The solar cell emerged in 1839 and have been applied in many places recently, and the price is sharply decreasing to 0.31$ in 2015.

1.1 General classification of solar cells

According to the solar cells (SCs) technology, SCs can be generally divided into three generations. The first generation is based on PN-junction and involved silicon wafer, of which power conversion efficiency is more than 25 %.[1] These silicon based SCs dominate and contribute to more than 87 % of global SCs market since silicon is the non-toxic, stable and abundant element. Additionally, silicon with energy band gap of about 1.12 eV (1107 nm cut-off light wavelength) covers almost the main whole solar spectrum. There are typically two types of silicon solar cells (SCs) including monocrystalline, polycrystalline silicon cells. Among them, monocrystalline SCs are most efficient, which use the mature growth technology. In order to reduce the cost, multi-crystals are used instead of single crystal. But their performance are always lower than that of single crystal.

Although the great achievement of power conversion performance is obtained for silicon SCs, the fabrication methods involved very expensive equipment and complex procedure motive the second generation SCs. They include amorphous silicon, copper indium gallium

selenide (CIGS) and Cadmium telluride photovoltaics (CdTe), where the typical performance is within the range of 10 – 20 %.[2-3] Compared to first generation, the absorber layer is thinner and amorphous silicon SCs are further more economic. Moreover, the thin-film also gives flexibility. CaTe SCs are also based on pn-junction, in which Cadmium sulphide behaves as the n-type material. This type SC represents the second largest commercial market after silicon SCs. Due to the low temperature coefficient of CdTe compared to silicon, the cell enables more than 66 ^{0}C working temperature and keeps lower than 8.5 % loss of efficiency, while silicon SCs will suffer more than 19 % loss. The above factors are beneficial for solving the rising global warming and wide industry application. The main disadvantage of CaTe SCs is to contain harmful Cd metal. Meanwhile, for amorphous silicon SCs, they always gives lower efficiency.

Although, compared to the first generation, the fabrication of second generation SCs is less expensive and easier. But they still need special conditions such as high vacuum, high thermal treatments, which consume extra energy. In addition, CIGS and CdTe involve rare and expensive elements on earth, which further limit their commercial applications. The above factors motive the emersion of the third generation, which are mainly based on organic materials such as small molecular or polymers. Besides organic photovoltaics, the third generation SCs include the dye sensitized solar cells (DSSCs),[4-5] whose studies started in the early 1990s. In DSSCs, the active material is dye molecules, which absorb the incident sun light. Unlike all solid state SCs, the organic solvent are included, in which iodide-triiodide redox couple is resolved. The best device efficiency so far is around 11 %. Another important third generation SCs are perovskite SCs especially $MAPbI_3$ based SCs. The boost efficiency of perovskite SCs within decades gives the most promising in economic SCs.

In order to overcome Shockley–Queisser limit (around 30 %) of theses single bandgap active material SCs, tandem cells with multi-layers are under intensive interest. In this type SCs, usually active layers are arranged with its energy gap to make sure short-wavelength region of the incident light can be absorbed before long-wavelength. This is because the transporting length for short-wavelength is relative shorter than long-wavelength. And the relative valence bands and conductive bands of the selected active materials should satisfy both smooth transportation of electrons and holes between all the interfaces. Besides the tandem SCs, the developed technology including hot-carrier effects, multiple-carrier ejection and frequency conversion are further studied to enhance the power conversion efficiency.

1.2 Metal halide materials and preparation methods

1.2.1 Materials

Figure 1 shows the typical structure of metal halide perovskite material. The perovskite represents the ABX_3, where A usually represents the monovalent cation including organic small cation Methylammonium (MA^+), Formamidinium (FA^+) and inorganic cation such as Cs^+, Ag^+ and so on, B is the metal cation (Pb^{2+}, Sn^{2+}, Sb^{2+}, Ge^{2+} and so on), X is the halogen anion (I^-, Cl^-, Br^-) or halide mixed. The perovskite crystal structure is of cubic and the structure stability can be characterized by Goldschmidt tolerance factor t,[6-8] which can be obtained as follows:

$$t = \frac{r_{A+}r_X}{\sqrt{2(r_B + r_X)}}$$

where r_A, r_X, r_B are the corresponding atom ionic radius. The perfect value is 1. And the range 0.8-1 is acceptable for perovskite structure, while too large or too small will not lead to perovskite structure. Large value is usually beneficial for material synthetization and film preparation. For the $MAPbI_3$, the tolerance factor is 0.92, which is very stable for the structure.

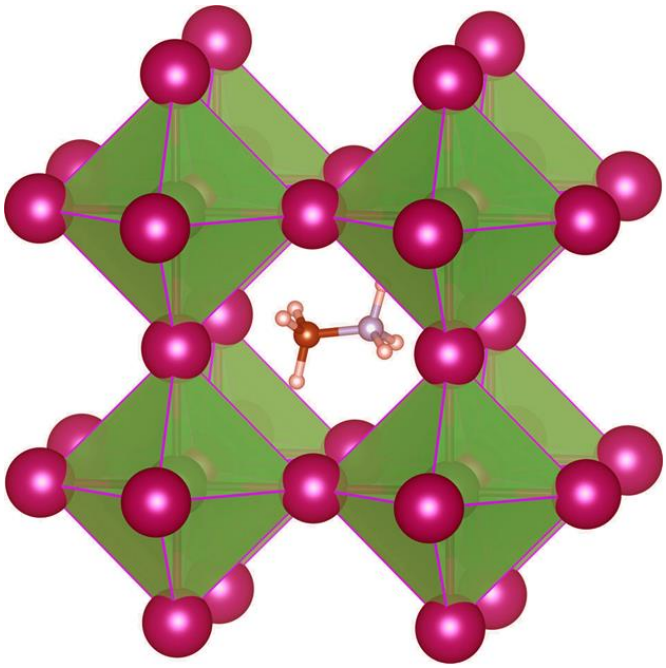

Figure 1. Schematic of the typical ABX_3 perovskite crystal structure.

Table 1 shows the recent reported metal halide materials including the perovskite materials with the detail energy gap and efficiency. Vacancy-ordered perovskite, double perovskite and two-dimension perovskite are also listed. Compared to the more than 21 % high efficiency of

lead based solar cells, lead-free materials including tin, bismuth, and antimony based photovoltaics give relative low efficiency. Among the lead-free materials, tin based SCs yield around 7 % efficiency, which is better than that of bismuth and antimony based SCs. In the absolute non-toxic materials (tin based compounds are unstable and show harmful in human health), bismuth based materials are the most promising candidates. However, considering their low efficiency, further development is needed.

Table 1. Recent reported metal halide materials

Family	Compound	Energy gap (eV)	Efficiency (%)
Perovskite	$MAPbI_3$	1.55	21[9]
	$MAPbBr_3$	2.18	7.11[10]
	$MASnI_3$	1.23	6.4[11]
	$FASnI_3$	1.22	9[12]
	$FAPbI_3$	1.49	20.6[13]
Vacancy-ordered perovskite	Cs_2SnI_6	1.26	6.94[14]
	Cs_2SnBr_6	2.7	0.04[15]
	Cs_2SnCl_6	3.9	0.07[15]
Two-dimensional perovskite	$Cs_3Bi_2I_9$	2.2	1.09[16]
	$MA_3Sb_2I_9$	2.14	0.5[17]
	$MA_3Bi_2I_9$	2.1	0.12[16]
	$Rb_3Sb_2I_9$	2.1-2.24	0.66[18]
Double perovskite	$Cs_2BiAgBr_6$	1.95	2.5[19]
	$Cs_2BiAgCl_6$	2.27	-
Others	$AgBi_2I_7$	1.87	1.22[20]
	$HDABiI_5$	2.1	0.027[21]

1.2.2 Preparation of thin-film of metal halide materials

1.2.2.1 Solution-proceed method

Planar films of halide materials are typically fabricated by one-step or two-step solution proceed methods.[22] The detail of a one-step method is shown in **Figure 2a**. First, samples are spin-coated of precursor solution of metal halide materials on the substrate. And then they are heated at proper temperature to completely remove the solvent. N,N-Dimethylmethanamide

(DMF), Dimethyl Sulfoxide (DMSO), Dimethylacetamide (DMA), Tetrahydrofuran (THF) and γ-butyrolactone (GBL) are employed as the solvent. After spin-coating, a saturated uniform complex film of organic solvent-metal halide material forms on the surface. After that, thermal heating is applied to completely remove solvent. It involves two stages of crystal growth. At first, seeds are formed on the surface of the substrates. And then, crystals grow larger. When the formed film morphology has pin-holes, solvent vapor annealing or anti-solvent method technology is applied for improving the film morphology.

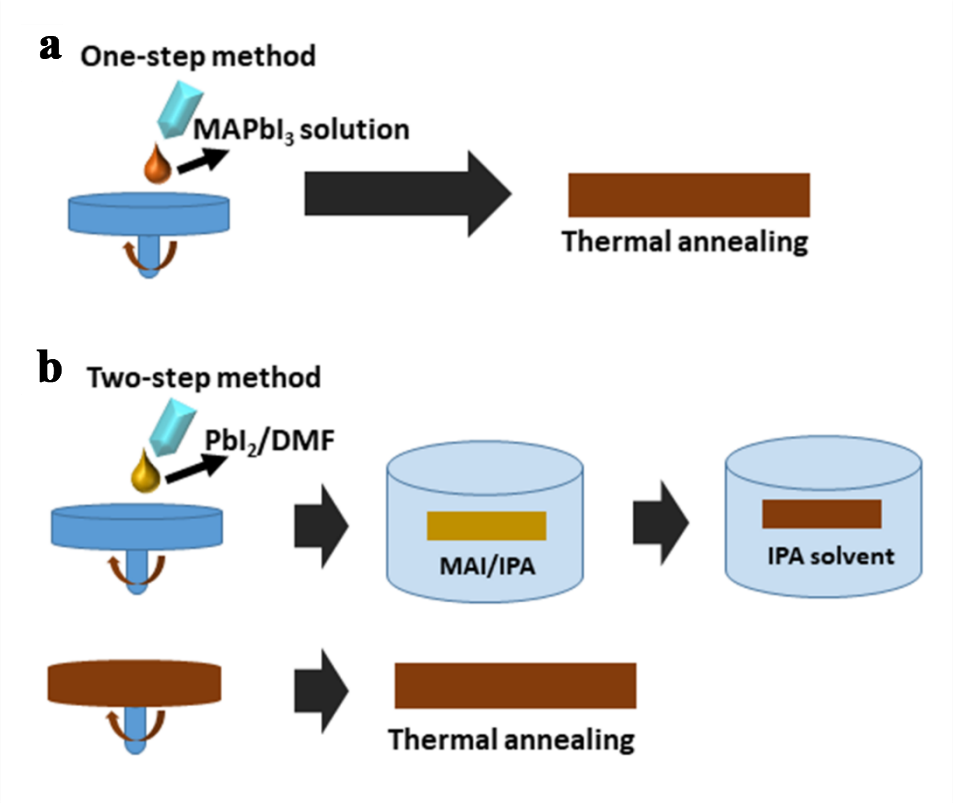

Figure 2. Schematic of one-step (a) and two-step (b) preparation method for $MAPbI_3$.

Figure 2b shows a two-step method in detail. After the spin-coating of the inorganic metal based participant (PbI_2) on a substrate, the sample is put on the hotplate to remove solvent. Then, the sample is immerged in the other participant solution (CH_3NH_3I/IPA) and wait for enough time (20s) to transform to $MAPbI_3$. After that, it dipped into the solvent to remove the extra MAI and spun. Finally, the sample is heated to remove all the solvent. It must be noted the solvent for the second participant should not dissolve the first layer. For $MAPbI_3$ film, PbI_2 is usually dissolved in DMF, while MAI in IPA. PbI_2 and $MAPbI_3$ have low solubility in IPA.

To overcome the poor morphology and coverage, anti-solvent technology is one of the most frequently used approach applied in one-step method,[23-25] which optimize as-prepared film before heating. **Figure 3** shows the anti-solvent method process. The whole process can be divided into two time-steps during the spin-coating. The prepared solution was dropped on the substrate and spun for enough time to cover the whole surface and then the anti-solvent is casted on the surface in one shot during the spinning, which will extract the solvent and make the film thin. The chosen anti-solvent for the anti-solvent method is the solvent which have excellent miscibility with the solvent of the as-prepared solution and meanwhile has very low solubility of the metal halide material.

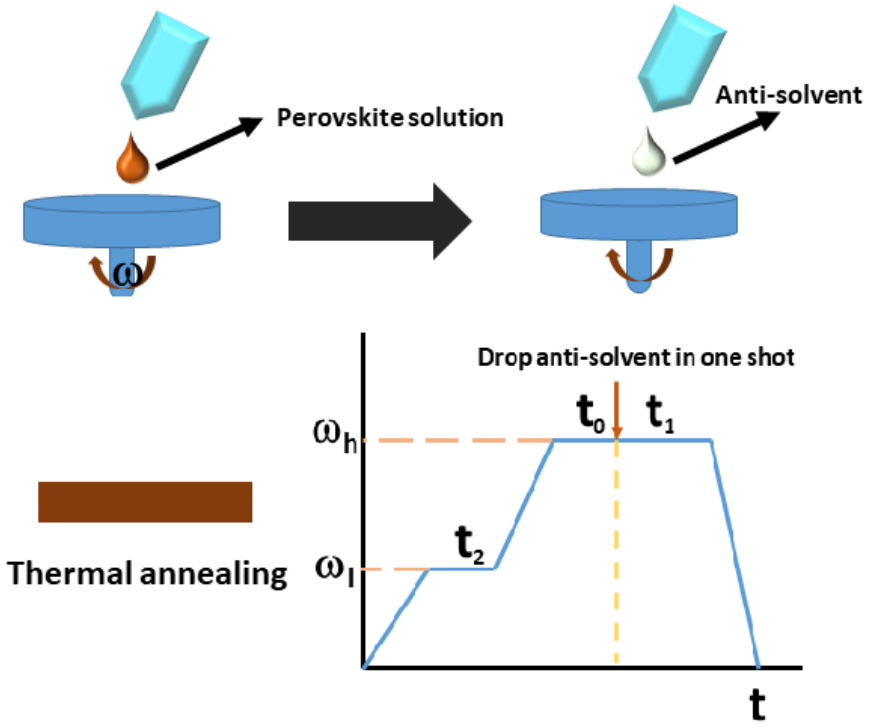

Figure 3. Schematic of anti-solvent technology to improve morphology of film.

This technology will form super saturated complex intermediate film without almost no extra mobilized solvent compared to the as-prepared film via one-step method. It leads to dense uniform seeds on the surface, which is beneficial for uniform dense high quality crystals. Generally, the size and density of the formed seeds strongly depends on the chosen anti-solvent, of which boiling point and miscibility are the two main factors. A series of anti-solvent for metal halide material are reported, which include trifluorotoluene, toluene, dichloromethane, esters and chlorobenzene. Taking ether for example, its low boiling point yields very poor coverage for $MAPbI_3$. It is mainly due to the too fast evaporation and solvent extraction. The

selection of useful anti-solvent should consider the confliction between the extraction and crystal growth. And different metal halide material and different solvent have different optimum anti-solvent.

Another frequently applied technology to improve the surface morphology and increase the grain size of the growth film of metal halide material is solvent vapor annealing method (SVA). SVA method is reported to improve the morphology mainly by suppressing the fast crystallization. As shown in **Figure 4,** sample is put on a holder in a container and surrounded with solvent vapor. Sometimes, for high boiling-point solvent, vapor is generated by thermal heating.

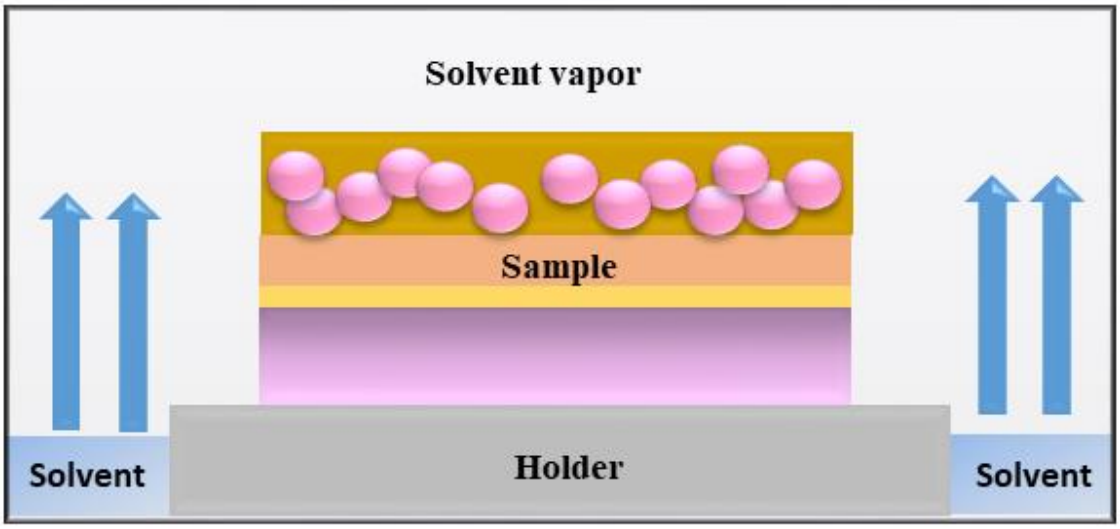

Figure 4. Schematic of solvent vapor annealing method.

The solvent vapor can greatly enlarge the grains to several micrometers without pin-holes. In addition, for co-solvent (more than two solvents), it overcomes the varied evaporation rate of each individual solvent with different boiling point, when using the traditional thermal annealing. For example, co-solvent of DMF (boiling point: 153 ^{0}C) and DMSO (boiling point: 189 ^{0}C) is frequently used to completely dissolve the MAI and SnI_2 during the fabrication of $MASnI_3$ devices.[26-27] And their different boiling points lead to different evaporation speeds during thermal annealing.

The selected solvent for SVA replaces and extracts the remained solvent of the as-prepared film via miscibility. Therefore, to obtain the best effect, the selection of solvent should consider the vapor pressure, boiling point and miscibility.

There are lots of other factors to influence the quality and morphology of the grown film such as vapor annealing time, temperature and the amount of solvent.[28]

1.2.2.2 Physical preparation method

To improve the gran size and morphology of the grown film, physical preparation method vapor assisted growth is recently reported.[29] Unlike the vapor of solvent in SVA, high temperature is needed to evaporate the solute. As shown in **Figure 5,** after spin-coating of PbI_2 precursor solution and following thermal annealing, a uniform PbI_2 film forms on the substrate. And then, the sample is put into an oven surrounded by MAI vapor, which is generated by heating MAI up to 200 ^{0}C.

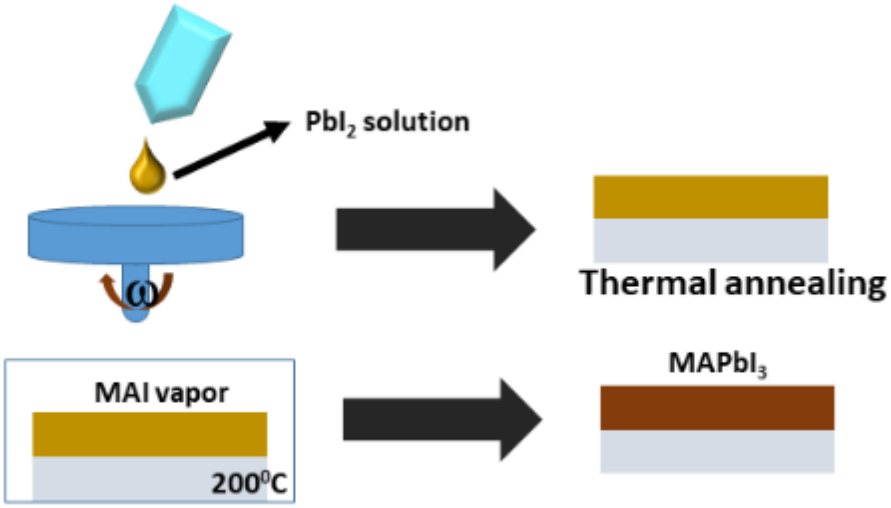

Figure 5. Process of physical method (vapor-assist growth method) to grow high quality $MAPbI_3$ films.

The MAI vapor is introduced to interact with PbI_2 and finally yields $MAPbI_3$.[29] Meanwhile, the whole reaction and the sample should be kept in such high temperature for enough time to complete the crystallization. Such high thermal energy will greatly enlarge the diffusion of nucleation, fuse neighbor grains and rearrange the crystal growth direction. Compare to solution-proceed methods, this vapor assisted growth method usually involves extreme conditions such as high-vacuum or high-temperature equipment, which limit their applications.

1.3 Structure and principle of metal halide solar cells

The structure of planar metal halide solar cells are mainly divided into four types structures. **Figure 6a, 6c** show the typical planar structure with and without porous scaffold. Conventional

planar devices are composed of transparent conductive oxide (TCO)-glass/ electron transport material (ETM)/ perovskite with mesoporous layer / hole transport material (HTM)/ electrode (gold or silver). Incident light is introduced from TCO/ETM side.

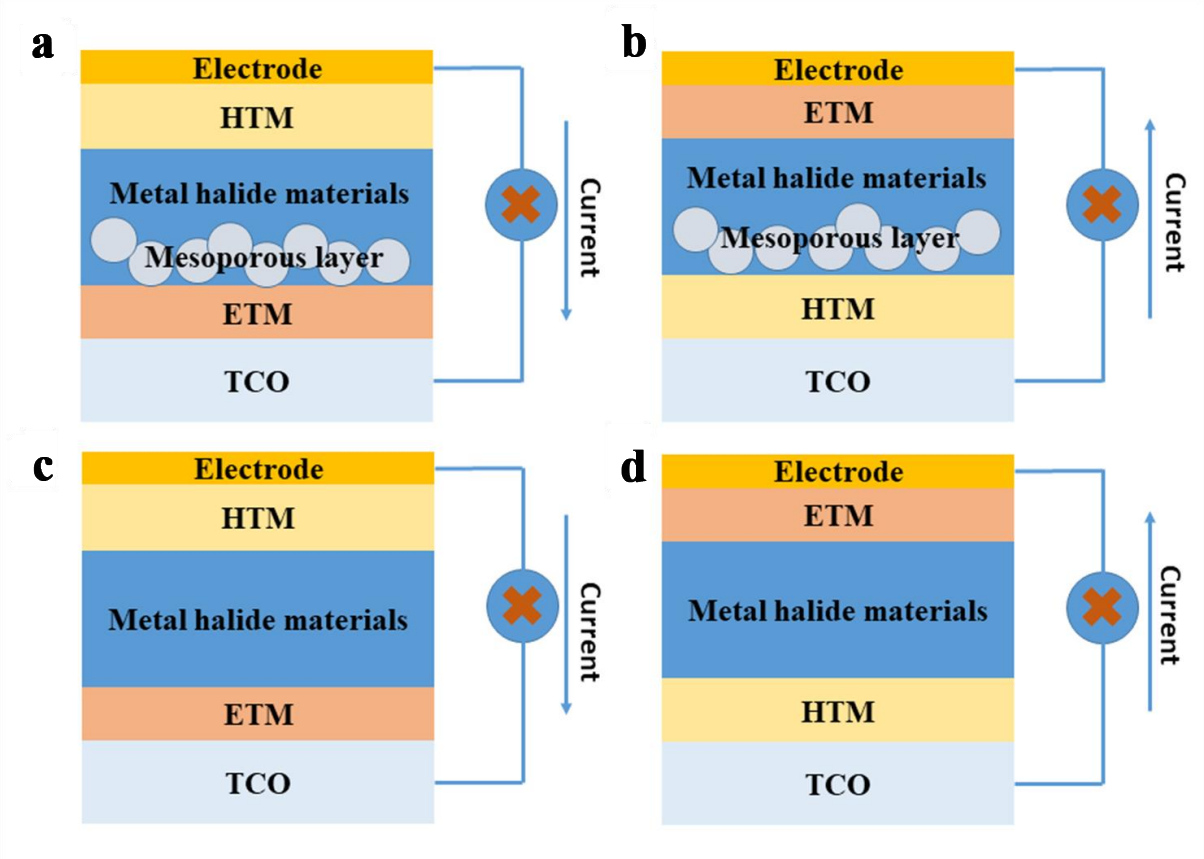

Figure 6. Schematic of devices structure, (a) and (c) are the normal planar SCs with and without mesoporous layer, while (b) and (d) are the inverse planar structure with and without mesoporous layer.

Figure 6b, 6d show the invers planar structure with and without porous scaffold. Inverse planar devices are composed of FTO-glass/ hole transport material (HTM)/ perovskite with mesoporous layer / electron transport material (ETM)/ electrode. Incident light is introduced from TCO/HTM side. The main difference between typical structure and invers structure is the opposite direction of the generated electric current, when exposed to sun light.

Figure 7 gives the energy diagram of the frequently used TCO/HTM/ETM materials. Usually, TiO_2, ZnO, SnO and PCBM act as ETM, while NiO, Spiro-OMeTAD, PEDOT:PSS and CuI are utilized as HTM. There are two frequently used TCO including Indium tin oxide (ITO) and Fluorine-doped tin oxide (FTO). The embedded mesoporous layer are nano-particles made of metal oxide materials including HTM or ETM materials. This mesoporous layer is not

only used as a skeleton to fill the grains of metal halide material but also acts as selective layer to immediately transport the generated carriers.

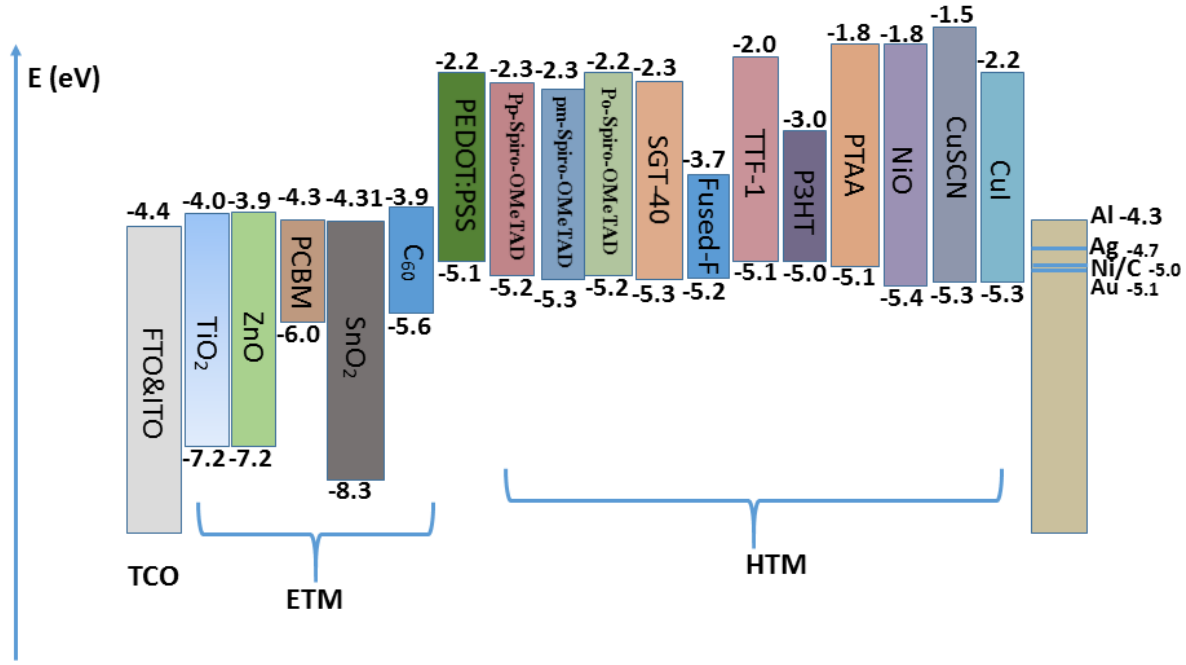

Figure 7. Energy diagram of the recent used TCO, HTM and ETM materials.

The transmittance of TCO layer directly determines the amount of light to the light harvesting layer. The recently reported metal nano-mesh and nanowire provide alternatives. These kinds of TCO enable more flexibility than conventional ones. But the transmittance are relative low. Gold and silver are the frequently used back-electrode. And silver has higher conductivity than gold, while gold is more stable than silver since silver is easily to be oxidized, especially the thin silver layer. Spiro-OMeTAD used as HTM gives high performance. The additives including lithium-bis-trifluoromethanesulfonyl-imide (LiTFSI) and tert-butylpyridine (TBP) are commonly used as additives to increase the carrier concentration.[30]

The mechanism of carriers collection is shown in **Figure 8.** Sun light is introduced from TCO and harvested by metal halide material, which converts light energy and generates hole-electron pairs. Electrons diffuse in perovskite layer, selective separated by ETM layer and finally collected by TCO layer. Hole carriers are transported though HTM layer and collected by the back-electrode.

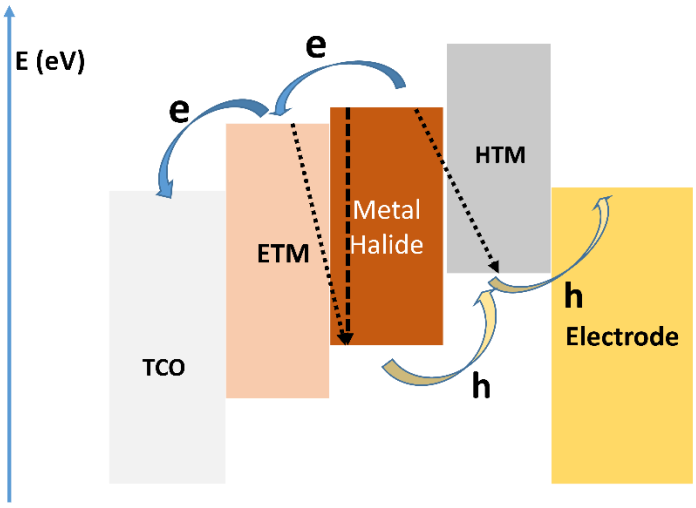

Figure 8. Schematic of energy diagram of devices. Solid lines show the transportation of the generated carriers, while dash lines show the possible recombination within device.

During the carrier transportation and generation, there exist three kinds of recombination of electrons and holes inside perovskite and at the interfaces. The defect density in perovskite crystals provides a trap-assisted recombination. And the defects at interfaces of ETM/ metal halide and metal halide/ HTM also recombine the generated carriers during their transportations. All these undesired kinds of recombination significantly affect the performance of devices. So, engineering of interfaces such as reducing the difference of valence bands of metal halide/ HTM or conductive bands of ETM/ metal halide are under intensive interest, which can realize the smooth carrier-transportations. In addition, improving the film quality of HTM and ETM are also beneficial for reducing the recombination.

1.4 Objective of this study

Although, metal halide solar cells, especially $MAPbI_3$ perovskite solar cells have gained excellent performance, there still exist two main issues. One is the relative expensive TCO layer and the other is the toxic lead in $MAPbI_3$ solar cells. The objective of this thesis is focusing on the optimization of light harvesting layer in three aspects aiming to solve these issues. First, a novel TCO-less back-contacted SCs by incorporating nanomesh like porous Ti electrode in active layer is provided to completely remove the expensive TCO layer. This structure overcomes the energy loss of incident light when transporting through TCO. Second, an efficient ultra-thin perovskite device by inter-coupling of the embedded hetero-dimers is given, which greatly reduce the amount of toxic lead in $MAPbI_3$ solar cells. At last, a bismuth based material is developed to completely replace the harvesting layer of lead based solar cells.

References

1. Green, M. A., The path to 25% silicon solar cell efficiency: history of silicon cell evolution. *Progress in Photovoltaics: Research and Applications* **2009,** *17* (3), 183-189.

2. Panthani, M. G.; Akhavan, V.; Goodfellow, B.; Schmidtke, J. P.; Dunn, L.; Dodabalapur, A.; Barbara, P. F.; Korgel, B. A., Synthesis of CuInS2, CuInSe2, and Cu (In x Ga1-x) Se2 (CIGS) nanocrystal "inks" for printable photovoltaics. *Journal of the American Chemical Society* **2008,** *130* (49), 16770-16777.

3. Feurer, T.; Reinhard, P.; Avancini, E.; Bissig, B.; Löckinger, J.; Fuchs, P.; Carron, R.; Weiss, T. P.; Perrenoud, J.; Stutterheim, S., Progress in thin film CIGS photovoltaics–Research and development, manufacturing, and applications. *Progress in Photovoltaics: Research and Applications* **2017,** *25* (7), 645-667.

4. Gong, J.; Sumathy, K.; Qiao, Q.; Zhou, Z., Review on dye-sensitized solar cells (DSSCs): Advanced techniques and research trends. *Renewable and Sustainable Energy Reviews* **2017,** *68*, 234-246.

5. Fan, K.; Yu, J.; Ho, W., Improving photoanodes to obtain highly efficient dye-sensitized solar cells: a brief review. *Materials Horizons* **2017,** *4* (3), 319-344.

6. Kieslich, G.; Sun, S.; Cheetham, A. K., An extended tolerance factor approach for organic–inorganic perovskites. *Chemical science* **2015,** *6* (6), 3430-3433.

7. Goudochnikov, P.; Bell, A. J., Correlations between transition temperature, tolerance factor and cohesive energy in 2+: 4+ perovskites. *Journal of Physics: Condensed Matter* **2007,** *19* (17), 176201.

8. Li, C.; Lu, X.; Ding, W.; Feng, L.; Gao, Y.; Guo, Z., Formability of ABX3 (X= F, Cl, Br, I) Halide Perovskites. *Acta Crystallographica Section B: Structural Science* **2008,** *64* (6), 702-707.

9. Saliba, M.; Matsui, T.; Domanski, K.; Seo, J.-Y.; Ummadisingu, A.; Zakeeruddin, S. M.; Correa-Baena, J.-P.; Tress, W. R.; Abate, A.; Hagfeldt, A.; Grätzel, M., Incorporation of rubidium cations into perovskite solar cells improves photovoltaic performance. *Science* **2016**.

10. Rao, H.-S.; Chen, B.-X.; Wang, X.-D.; Kuang, D.-B.; Su, C.-Y., A micron-scale laminar MAPbBr3 single crystal for an efficient and stable perovskite solar cell. *Chemical Communications* **2017,** *53* (37), 5163-5166.

11. Noel, N. K.; Stranks, S. D.; Abate, A.; Wehrenfennig, C.; Guarnera, S.; Haghighirad, A.-A.; Sadhanala, A.; Eperon, G. E.; Pathak, S. K.; Johnston, M. B., Lead-free organic–inorganic

tin halide perovskites for photovoltaic applications. *Energy & Environmental Science* **2014,** *7* (9), 3061-3068.

12. Shao, S.; Liu, J.; Portale, G.; Fang, H. H.; Blake, G. R.; Brink, G. H. t.; Koster, L. J. A.; Loi, M. A., Highly Reproducible Sn‐Based Hybrid Perovskite Solar Cells with 9% Efficiency. *Advanced Energy Materials* **2018,** *8* (4), 1702019.

13. Bi, D.; Tress, W.; Dar, M. I.; Gao, P.; Luo, J.; Renevier, C.; Schenk, K.; Abate, A.; Giordano, F.; Correa Baena, J.-P.; Decoppet, J.-D.; Zakeeruddin, S. M.; Nazeeruddin, M. K.; Grätzel, M.; Hagfeldt, A., Efficient luminescent solar cells based on tailored mixed-cation perovskites. *Science Advances* **2016,** *2* (1), e1501170.

14. Lee, B.; Stoumpos, C. C.; Zhou, N.; Hao, F.; Malliakas, C.; Yeh, C.-Y.; Marks, T. J.; Kanatzidis, M. G.; Chang, R. P., Air-stable molecular semiconducting iodosalts for solar cell applications: Cs2SnI6 as a hole conductor. *Journal of the American Chemical Society* **2014,** *136* (43), 15379-15385.

15. Kaltzoglou, A.; Antoniadou, M.; Kontos, A. G.; Stoumpos, C. C.; Perganti, D.; Siranidi, E.; Raptis, V.; Trohidou, K.; Psycharis, V.; Kanatzidis, M. G., Optical-vibrational properties of the Cs2SnX6 (X= Cl, Br, I) defect perovskites and hole-transport efficiency in dye-sensitized solar cells. *The Journal of Physical Chemistry C* **2016,** *120* (22), 11777-11785.

16. Park, B. W.; Philippe, B.; Zhang, X.; Rensmo, H.; Boschloo, G.; Johansson, E. M., Bismuth based hybrid perovskites A3Bi2I9 (A: methylammonium or cesium) for solar cell application. *Advanced Materials* **2015,** *27* (43), 6806-6813.

17. Hebig, J.-C.; Kühn, I.; Flohre, J.; Kirchartz, T., Optoelectronic properties of (CH3NH3) 3Sb2I9 thin films for photovoltaic applications. *ACS Energy Letters* **2016,** *1* (1), 309-314.

18. Harikesh, P.; Mulmudi, H. K.; Ghosh, B.; Goh, T. W.; Teng, Y. T.; Thirumal, K.; Lockrey, M.; Weber, K.; Koh, T. M.; Li, S., Rb as an alternative cation for templating inorganic lead-free perovskites for solution processed photovoltaics. *Chemistry of Materials* **2016,** *28* (20), 7496-7504.

19. Greul, E.; Petrus, M.; Binek, A.; Docampo, P.; Bein, T., Highly stable, phase pure Cs2AgBiBr6 double perovskite thin films for optoelectronic applications. *Journal of Materials Chemistry A* **2017,** *5* (37), 19972-19981.

20. Kim, Y.; Yang, Z.; Jain, A.; Voznyy, O.; Kim, G. H.; Liu, M.; Quan, L. N.; García de Arquer, F. P.; Comin, R.; Fan, J. Z., Pure Cubic‐Phase Hybrid Iodobismuthates AgBi2I7 for Thin‐Film Photovoltaics. *Angewandte Chemie International Edition* **2016,** *55* (33), 9586-9590.

21. Fabian, D. M.; Ardo, S., Hybrid organic–inorganic solar cells based on bismuth iodide and 1, 6-hexanediammonium dication. *Journal of Materials Chemistry A* **2016,** *4* (18), 6837-6841.
22. Burschka, J.; Pellet, N.; Moon, S.-J.; Humphry-Baker, R.; Gao, P.; Nazeeruddin, M. K.; Grätzel, M., Sequential deposition as a route to high-performance perovskite-sensitized solar cells. *Nature* **2013,** *499* (7458), 316-319.
23. Cohen, B.-E.; Aharon, S.; Dymshits, A.; Etgar, L., Impact of antisolvent treatment on carrier density in efficient hole-conductor-free perovskite-based solar cells. *The Journal of Physical Chemistry C* **2015,** *120* (1), 142-147.
24. Paek, S.; Schouwink, P.; Athanasopoulou, E. N.; Cho, K.; Grancini, G.; Lee, Y.; Zhang, Y.; Stellacci, F.; Nazeeruddin, M. K.; Gao, P., From Nano-to Micrometer Scale: The Role of Antisolvent Treatment on High Performance Perovskite Solar Cells. *Chemistry of Materials* **2017,** *29* (8), 3490-3498.
25. Park, N.-G.; Grätzel, M.; Miyasaka, T.; Zhu, K.; Emery, K., Towards stable and commercially available perovskite solar cells. *Nature Energy* **2016,** *1* (11), 16152.
26. Fujihara, T.; Terakawa, S.; Matsushima, T.; Qin, C.; Yahiro, M.; Adachi, C., Fabrication of high coverage MASnI 3 perovskite films for stable, planar heterojunction solar cells. *Journal of Materials Chemistry C* **2017,** *5* (5), 1121-1127.
27. Yokoyama, T.; Cao, D. H.; Stoumpos, C. C.; Song, T.-B.; Sato, Y.; Aramaki, S.; Kanatzidis, M. G., Overcoming short-circuit in lead-free CH3NH3SnI3 perovskite solar cells via kinetically controlled gas–solid reaction film fabrication process. *The journal of physical chemistry letters* **2016,** *7* (5), 776-782.
28. Xiao, Z.; Dong, Q.; Bi, C.; Shao, Y.; Yuan, Y.; Huang, J., Solvent Annealing of Perovskite-Induced Crystal Growth for Photovoltaic-Device Efficiency Enhancement. *Advanced Materials* **2014,** *26* (37), 6503-6509.
29. Ma, T.; Zhang, Q.; Tadaki, D.; Hirano-Iwata, A.; Niwano, M., Fabrication and Characterization of High-Quality Perovskite Films with Large Crystal Grains. *The Journal of Physical Chemistry Letters* **2017,** *8* (4), 720-726.
30. Nguyen, W. H.; Bailie, C. D.; Unger, E. L.; McGehee, M. D., Enhancing the hole-conductivity of spiro-OMeTAD without oxygen or lithium salts by using spiro (TFSI) 2 in perovskite and dye-sensitized solar cells. *Journal of the American Chemical Society* **2014,** *136* (31), 10996-11001.

2. Mechanism and characterization

2.1 Crystallization of metal halide materials

The whole film growth shows a very complex procedure from molecular (zero-dimension) to film (three-dimension). The general mechanism behind the thin-film growth of metal halide material on substrate via nucleation and crystal size growth processes is shown in **Figure 1**. The dropped solution disperses on the substrate surface. After the traditional treatment such as spin-coating, the solution on the surface become saturated. Metal halide material molecules favor on the surface, and then move and collide to form the initial clusters. Because of the energy unfavorable of such small size, these clusters tend to grow in size with the supplement of solute molecular and finally reach a critical size[1-4]. The formed seeds are initially located randomly on the surface and finally cover the whole surface, of which density and average size strongly depends on the involved energy such as thermal energy and solubility. Meanwhile, seeds generally grow random crystals and arrange randomly. Therefore, additional energy is necessary to increase the order such as temperature or the introduced chemical bond of the solute molecular with the substrate.

The removal of the solvent will further increase the collision of seeds and grow larger and larger as the surface energy decrease with size. The generated grains form initial islands, which will be connected and fused with each other to become the final film. Random arranged crystals, the undesired defects and pin-holes sometimes appear inside the film. Meanwhile, the final grain size strongly affects the carriers mobility (including electrons and holes), lifetime and influence the photoelectric properties. To make uniform and high quality film, additional energy such as increasing the annealing temperature is necessary. At last, the completely removal of solvent yields the final film.

Generally, there are lots of factors that determine the final morphology and properties of the crystal growth. First, the surface of the substrate should be enough wettable to the solution. And the average absorbing energy of molecular and surface should be lower than the interaction between molecules. Thereby, the formed collides will be favorable to locate on the surface and form uniform dense seeds. Second, the material should have enough tolerance to overcome the produced stress within crystals. Third, the speed of removing solvent during the

whole process should enable enough time for molecular self-assembly as the surface diffusion length l is dependent on the available diffusion time t. It is shown as follows:

$$l = \alpha\sqrt{\Gamma t}$$

where Γ is the jump-hopping rate, a is the average path length for each jump.

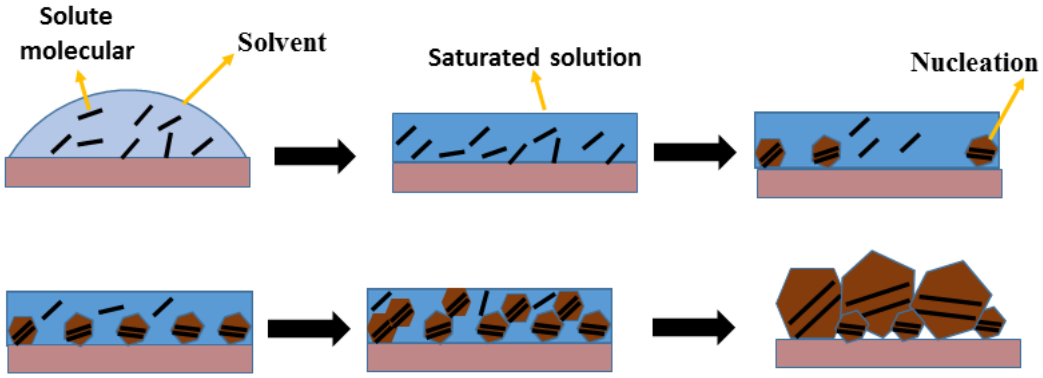

Figure 1. Schematic of crystallization process of metal halide material thin-film.

The surface-roughness of the final film is a very important physical parameter, which someway depends on the initial nucleation and the metal halide material properties. The small critical size of the formed seeds tends to form small grains, which is unfriendly with the carrier diffusion length and mobility. And high concentration (solubility) usually yields dense initial seeds on the surface, which turns to be smooth and high coverage continuances thin film. On the other hand, the material with low solubility but large critical size of seeds turns to be large grains but discontinued ununiformed film. Therefore, the optimization of solubility and critical size of seeds are very important to obtain high coverage and large grains of the growth film.

2.2 Mechanism of spin-coating process

Spin-coating is a low-cost, highly reproducible film preparation method, which utilizes centrifugal force to disperse precursor solution.[5-7] And meanwhile, the evaporation of solvent during the process leads to the intermediate film. **Figure 2** shows the general spin-coating process and schematic of the spin-coater. Usually, the differential pressure between outside and inside produced by continuous pumping strongly attached the sample on the holder. It provides enough frictional force to overcome the centrifugal force on the sample especially for the asymmetric location under high spinning speed.

Generally, there are two steady speeds during the spinning.[1,8] After dropping enough solution, the angular velocity of the sample accelerate from zero to the low-steady speed ω_l and maintain for t_2 time. The generated centrifugal force on the solution spread and flat solution on the whole surface. Subsequently, the high centrifugal force induced by the high angular velocity ω_h at next stage further shrink and thin film for t_1 time, which meanwhile gives time to evaporate solvent and finally leave a uniform film.

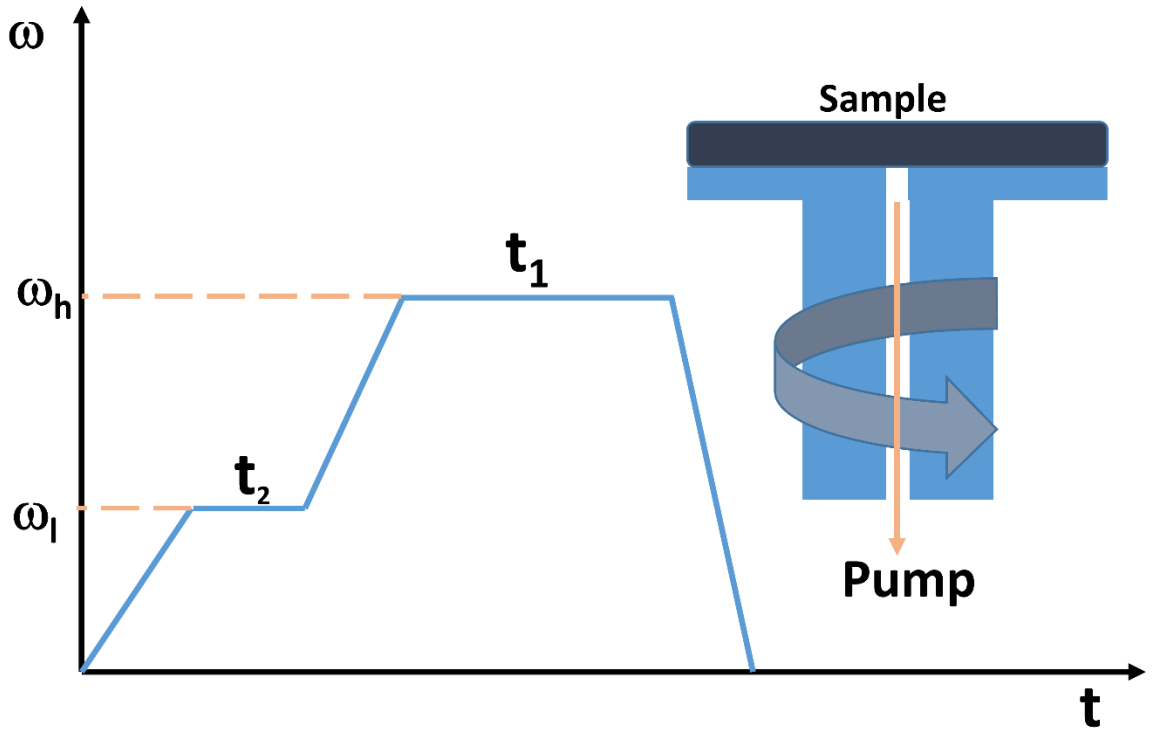

Figure 2. Schematic of spin-coater and spin-coating process.

There are many factors to influence the thickness and uniformity of the prepared film. Higher spinning speed and longer time treatment will make the film thinner, which is approximately known as the invers of square root of angle velocity.

$$h \propto {}^{1}/_{\sqrt{\omega}}$$

The frequently used low-spinning speed at the first stage is about 500 rpm, while the high-spinning speed at the second stage is within the range 1-8 k rpm, of which uniform, good quality film can be relatively easily achieved. According to the above equation, the final thickness is within the range 0.7-0.25 of that at the first stage. For 1M $MAPbI_3$ solution, 500 rpm/ 6 k rpm usually leads to around 350 nm perovskite film.

In addition, thickness of the final film is as a function of the precursor concentration and strongly depends on the properties of the solution including solvent evaporation rate,[9] viscosity. The thickness of the film is also influenced by the surrounding atmosphere including the room temperature and humidity near the substrate, which affect the evaporation rate of the solution during the spinning. Generally, the precise thickness are varied with solution of different materials even with same precursor concentration. To obtain uniform film, relative steady atmosphere such as low airflow surrounding the sample should be maintained during the whole spinning. The acceleration during spinning especially at the first stage depending on t_2 and ω_1 is another factor to influence the final film. Generally, the spinning acceleration is linear with differential angle velocity. The acceleration strongly determine the amount of remaining solute since most of the dropped solution is casted out when acceleration starts. In addition, twisting force generated by this acceleration improves the dispersion of solution in tangential direction.

Surface tension of precursor solution on the substrate is another factor to affect the final film, which determines the spreading speed of solution during spinning. In addition, both the properties of substrate and solution give the surface tension. And wettable surface is necessary for good film, while too high speed of solution lead to inadequate volume of solute. **Figure 3** shows three kinds of undesirable films. As in **Figure 3a,** bubbles like spots on wafer surface of sample is usually induced by air bubbles in the spread solution after dropping or by the dirt or the defect surface on the uncleaned sample. In addition, **Figure 3b** shows that too high evaporation rate or velocity always leads to stripe like sample, which can be also induced by too high acceleration or too fast spinning. The uncompleted coverage situation in **Figure 3c** is mainly caused by the not enough volume of the scatted solution. In addition, the unbalance location of sample will lead to inhomogeneous film. **Figure 3d** gives the desired perfect sample. The thickness of the inside region near the center is slightly thinner than outside.

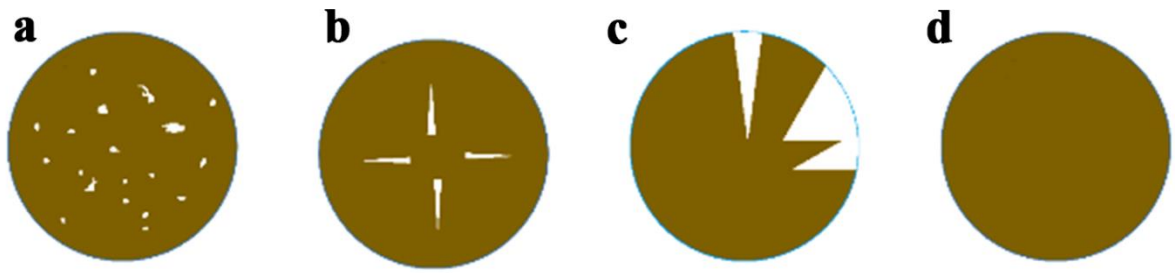

Figure 3. (a) Bubbles like spots, (b) stripe like, (c) large-uncovered areas and (d) perfect final film.

2.3 Morphology characterization

It is very important to study the morphology of the grown film, especially the grains to precisely control the preparation process. Moreover, morphology affects other physical properties as well as the final power conversion efficiency of devices. [9-11]

Optical microscope is frequently used to roughly observe the uniformity, pinholes and coverage. This type of microscope as the mature observation microscope utilizes a series of lenses and visible light to magnify the details on the surface. Optical images yielded from traditional optical microscope are usually generated via photosensitive cameras. The recent integrated charge-coupled device (CCD) enables the digital photos, which can be dynamically captured and put on the screen during the observation. The ocular and objective lens in the machine determine the actual magnification value. Precisely, the product of them gives the final magnification value. Until now, the maximum 1 k is given by 10x and 100x for ocular and objective lens respectively. The resolution of the optical microscope can be calculated by $r = \lambda/2NA$, which is determined by the wavelength of incident light and the microscope numerical aperture (NA). Therefore, it cannot tell the fine detail, which is smaller than approximate 0.2 um. It is around half of the shortest visible wavelength 400 nm (NA=1 the best).

As nano poly-crystals are usually obtained in the typically prepared metal halide material film, sub-1 um microscope is needed to further observe the detail morphology of crystals. Scanning electron microscope (SEM), which can detect around 1 nm at most, is frequently used. The interaction of the atoms near the surface of sample with the high energy electron beam generated by electron gun and accelerated by high bias voltage generally yields five main types of signals such as Auger elections, secondary electrons (SE), back-scattered electrons (BSE), cathodoluminescence (CL) and transmitted electrons. For SEMs, images come from the signal of the collection and analyzation of SE. Since, the wavelength of high energy electrons is very short, ultra-high resolution around 1nm details can be revealed. In addition, BSE, which is scattered from the location deep inside the measured sample, is related to the atomic number. Therefore, it can give the detail elements distribution of the measured sample.

To observe and analyze the morphology of the surface, films should be electrically conductive enough and prepared on the conductive substrate or stick on the holder with conductive glue to avoid the over cumulative electrons on the sample. And for the unconducive sample, SEM produces unclear image and the electron beam will probably damage the focused

surface. Sometimes, unconducive samples are coated with thin gold layer on the surface by thermal evaporation to yield clear SEM image. As the wavelength of the generated electrons limit the final resolution, high voltage is needed for high resolution images.

Although, high resolution can be obtained by SEM, the details around 1nm or sub-1nm of the sample is not clear. Another microscope called Scanning Tunneling Microscope (STM) is needed.[12-16] STM can even roughly tells individual atoms on the surface. Moreover, unlike the needed vacuum condition in SEM, TEM can work in both vacuum and varied ambient condition including liquid and air. It is also available under high temperature. The mechanism behind STM is electron quantum tunneling. When the distance between conductive tip and the surface of the sample is very small and a voltage bias is applied between them, electrons can be allowed to tunnel and form the tunneling current signal. Usually, the conductive tip is very sharp and only several atoms exist on the top. This tunneled current is strongly determined by the distance. Therefore, morphology on the surface is observed. And to obtain the image, the conductive tip is moved across the surface (fixed the sample) or the sample is moved (fixed the tip) with very tiny step-width. The disadvantage is the needed very clean, stable sample. And the whole equipment is under extreme situation including perfect balance with very tiny vibration.

2.3 Optical properties

2.3.1 Absorbance, transmittance and reflectance

Figure 4 shows the absorbance of film, which demonstrates the energy loss of the incident light when through materials, and its relationship with intensity of incident light I_0 and the transmitted intensity I_t is represented as follows:[17-21]

$$A_\lambda = -log_{10}\,(I_0/I_t)$$

There is a relationship between the thickness of the measured film and the absorbance, which is expressed by the Beer-Lambert Law, $A \propto \epsilon b$, where ϵ, b are the molar absorptivity, path length of the measured film respectively. According to the equation, absorbance is directly proportional to light transmitted length (directly determined by the film thickness). Zero thickness gives the same I_0 and I_t, which leads to zero absorbance, while long enough thickness (∞) make all incident light are absorbed and zero I_t is observed, which leads to infinity A_λ value.

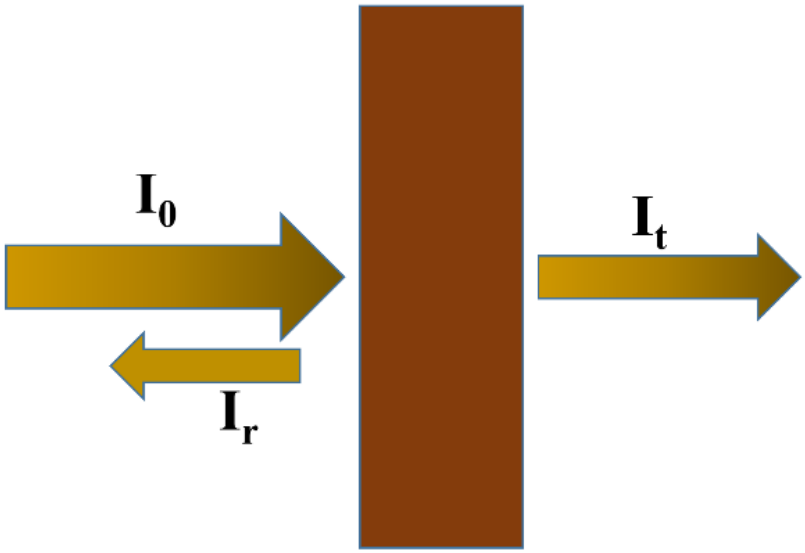

Figure 4. Absorbance, reflectance and transmittance of film.

Additionally, the energy bandgap of material can be directly determined from its absorbance via Tauc plot. This plot is the calculated curve between optical energy (hv) and $(\alpha hv)^r$, where r, a are the constant of photon transition, the absorption coefficient of the calculated material respectively. Generally, the material with direct bandgap, r=2 is used, while ½ for indirect bandgap. Moreover, r is 2/3 or 1/3, which means the measured material has the forbidden direct and indirect transitions respectively. The linear region shown on the plot demonstrate the onset value, which is the expected optical bandgap. Transmittance T and reflectance R can be obtained by the following equations:

$$\begin{cases} T = I_t/I_0 \\ R = I_r/I_0 \end{cases}$$

Therefore, the relationship between absorbance and transmittance is given as follows:

$$A_\lambda = 2 - log 10\%T$$

It provides an easy method to calculate the absorbance from the transmittance. Since the incident energy is the sum of reflected and transmitted energy for nondispersive materials, $I_0 = I_r + I_t$, thus $R = 1 - T$. The interface and the dielectric constant of the materials strongly affect the reflectance. For absorber materials, the absorbed light energy by material should be considered.

2.3.2 Photoluminescence of materials

Photoluminescence (PL) phenomenal is that materials after absorbing photons emit light. As shown in **Figure 5,** after absorbing the incident light (higher energy than band gap), electrons at ground state will jump from a low energy level in valence bands to a high energy level in conductive bands leaving a hole in the valence bands. And then, electrons and holes will go back to the conductive band and valence band respectively through internal non-radiative transition. Then the recombination of them emit the light. The wavelength of the emitted light is associated with the energy bandgap structure of the material. There are two PL spectrums including steady state PL and time-resolved PL. Steady state PL shows the intensity of the emitted light with the particular wavelength of the incident light, while the time-resolved PL give the emission delay with the time after absorbing photons. It must be noted that the exited wavelength should be shorter than the band-gap of material. The peak of steady state PL is related with the energy bandgap. Usually, for steady state PL, the emitted intensity at the wavelength for indirect band-gap is very low compared to the direct band-gap position. Meanwhile, the decay time for time-resolved PL is varied from sub-nanosecond to several milliseconds depending on the quality of the film and the material itself. The PL delay time represents the carrier (electrons/ holes) life time. Long life time give rich time for the hole-electron pairs separation and also greatly reduce the recombination rate, which are also beneficial for carriers diffusion length.

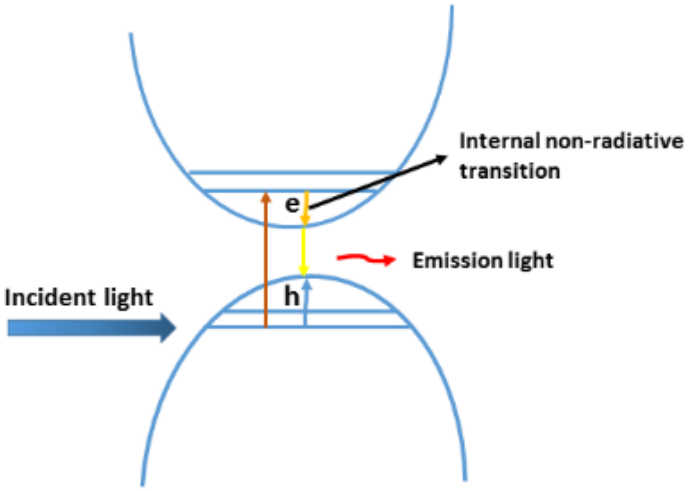

Figure 5. Schematic of the photoluminescence process.

2.4 Hall effect and carriers mobility in semiconductors

Carrier mobility μ is an important physical parameter of materials representing the carrier transportation property. It denotes the ratio of the speed of a carrier (including electron and hole) to the applied electric field E, which is defined by the following equation:

$$v = \mu E$$

There are two types of mobility called electron mobility and hole mobility in a semiconductor. Product of mobility and carrier concentration determines the conductivity. The device performance based on semiconductors are related with mobility. Higher mobility usually leads to higher short-circuit density and better power conversion efficiency. There are lots of physical factors to affect the mobility such as defect concentration, carrier concentration and temperature. Large and high quality crystals of film are beneficial for high mobility.

Hall Effect (**Figure 6**) is the frequently used technology to measure carrier mobility, which utilizes the produced Lorentz force by the applied electron field on the inside carries. It drives carriers to one surface of the material. These carriers accumulate. Meanwhile, the opposite carriers with equal amount will emerge on the other surface. Then, bias voltage is formed, which is strongly affected by the defect and impurity inside material. Hall mobility is given by $\mu = \sigma R_H$, in which hall coefficient is denoted as $R_H = \frac{E_y}{j_x B_z} = -\frac{1}{ne}$, where Ey is the applied electric field, j is the current density and B is the applied magnetic field.

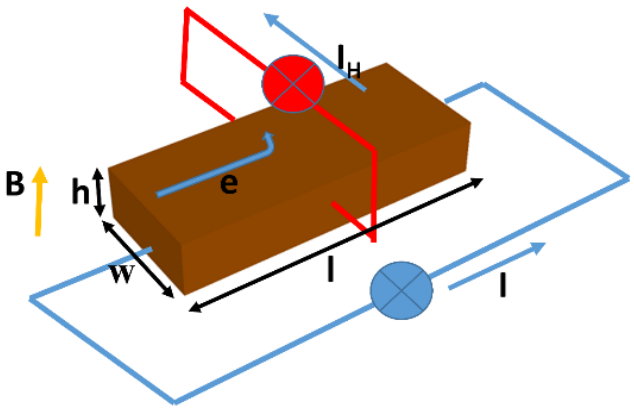

Figure 6. Schematic of Hall Effect measurement for Hall mobility, carrier concentration and resistivity.

The above equations also gives both the carrier concentration and conductivity. It should be noted, to measure the Hall Effect, four electrodes should be deposed on the sample.

2.5 Photovoltaic properties of metal halide materials

Power conversion efficiency represents the ability of the material to convert the input energy to the available target energy. For metal halide material photovoltaics, solar energy is absorbed by the devices and converted to electrical energy. And it can be expressed as follows,

$$\eta = \frac{P_{out}}{P_{in}}$$

where P_{out} is the available power, and P_{in} is the input light energy. The perfect complete conversion is expected to have perfect absorption of photons energy of incident light with the complete generation of electron-hole pairs without any loss and perfect separation, collection and transportation. Therefore, the actual efficiency of devices are lower than 100 %. Solar simulator is the frequently used machine to simulate solar spectrum and provides artificial sunlight for device photovoltaic performance. Usually,1 sun is introduced, which is the nominal full sunlight intensity 100 mW/cm^2. In addition, a shadow mask with certain area hole is needed to cover the sample. This parameter should be set before measuring. In the J-V curve as shown in **Figure 7** measured by solar simulator, $P_{out} = P_{max}$, which is the possible obtained largest value of product of current and voltage. It is the available electric power when calculating the efficiency.

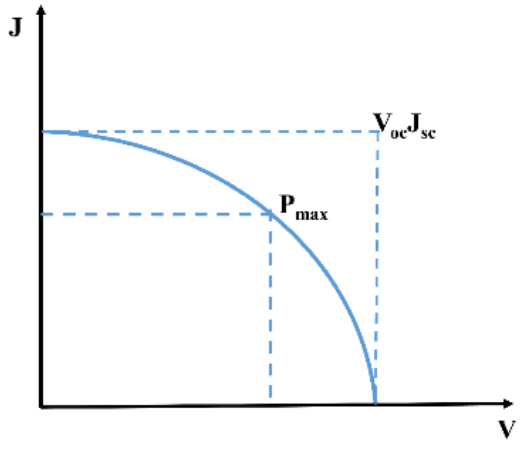

Figure 7. J-V curve of the typical metal halide photovoltaic device. Pmax is the largest value of product of current and voltage. Voc and Jsc are the open-circuit voltage and short-circuit current density respectively.

Fill factor is defined as $FF = \frac{P_{max}}{V_{oc}J_{sc}}$, where Voc and Jsc are the open-circuit voltage and the short-circuit current respectively. FF is a very important factor to investigate the performance of devices, which is affected by internal resistance of SCs strongly depending on the interface between layers and materials used in SCs. Generally, the range of FF for metal halide SCs is around 0.72, which is still lower than that of typical silicon photovoltaics (more than 0.8). The idea open-circuit voltage of devices increase with the bandgap of semiconductor. But due to the recombination and structure of the device, there exists the called open-circuit voltage loss. And the quality and size of the grains plays an important role in reducing the loss.

IPCE standing for incident photon to converted electron ratio also known as quantum efficiency indicates the intensity of the current produced by the measured solar cell when exposed to irradiation with a particular wavelength. And the collected number of carriers depending on the wavelength gives the IPCE spectrum.

There are two kinds of quantum efficiency named as External Quantum Efficiency (EQE) and Internal Quantum Efficiency (IQE). EQE and IQE are the ratio of the amount of the collected charge carriers to the incident light energy and the absorbed light energy respectively. They are slightly different. EQE is smaller than IQE, since the exposed light usually cannot be absorbed completely without any loss. Recently close to 95% IPCE is observed for $MAPbI_3$ devices. The short-circuit current Jsc can be obtained from IPCE. The equation is shown as follows:

$$Jsc = -q \int_{\lambda_{min}}^{\lambda_{max}} EQE(\lambda)\phi_{AM}\, d\lambda$$

where λ_{min} and λ_{max} are the maximum and minimum wavelength in the standard sun light. The range of 300nm-800nm is always used for $MAPbI_3$ devices. It must be noted the calculated value should match with the measured one. There is an idea value for 100% EQE, which strongly depends on the band-gap of the metal halide material. Therefore, low band-gap has larger possible Jsc, while it processes lower possible obtained Voc.

When metal halide materials devices applied with voltage V_{dark} in dark, small current named dark current will form. For the metal halide material, the dark current J_{dark} is expressed as follows:

$$J_{dark} = J_0(\exp\left[\frac{qV_{dark}}{nkT}\right] - 1)$$

where J_0 and q are the saturation current density and the one-carrier charge respectively. Other parameters are phenomenological constant n, the Boltzmann constant k and the temperature T respectively. Dark current curve reveals the property of device structure including the quality of the prepared films inside device.

Hysteresis phenomena is frequently reported in photovoltaics, which illustrates the difference of J-V curves in two scanning modes, forward (V from 0 to Voc) and reverse mode (V_{OC} to zero). Reducing hysteresis is under intensive interest since large hysteresis will greatly influence the overall efficiency. It is known to contribute to the existence of mobilized ionic and strongly affected by cell structure, the adopted material and the scanning speed during the measurement. Generally, slow scanning speed is beneficial for low hysteresis phenomena, while large accumulated ionic concentration greatly harms the performance.

2.6 XRD and characterization of structure and quality of the grown films

Generally, all three dimension crystals are within 7 crystal systems, 14 bravais lattices and 32 crystal classes corresponding to 32 space group. To determine the particular crystal structure, X-ray diffraction is the frequently used nondestructive approach, which utilizes the short wavelength of the generated X-ray. It is comparable with the dimension of space lattice. The induced X-ray will be interacted and diffracted into many particular directions, and then, collected and analyzed. The relationship between miller indices (h, k, l) and diffraction angle (θ) is known as Bragg law, which is shown as follows:

$$2d_{h,k,l}\sin\theta = n\lambda$$

The collected X-ray signal is mainly reflected through a set of angle corresponding to n = 1, which is called the first order of diffraction. In addition, the angle for n = 2 corresponds to the second order, and so on. The diffraction pattern of intensity (or counts) of X-ray depending on angle is unique for each material. All the possible peaks can be shown in powder XRD. Meanwhile, from this XRD pattern, the crystal structure including the dimension and space group can be obtained. Due to the mixed materials yields the sum of XRD peaks of each individual material, components are able to be analyzed. In addition, the existence of the disorder atoms inside crystals induced by the internal pressure or defect may lead to the shift of some observed XRD peaks compared to the standard Powder Diffraction File (PDF) card.

Quality of crystals can be characterized by the intensity and Full Width at Half Maximum (FWHM) of the peaks. FWHM represents the width of the diffraction peak at a half way height.

The strong intensity with small width is usually observed from the film with well-arranged crystals or single crystalline. These high quality films will produce low-index miller indices as well as high-miller indices.

2.7 Measurement of film thickness

The thickness of the grown film produced by spin-coating strongly relies on the concentration of precursor solution and spinning speed. The thickness is obtained via detecting the interference phenomenal with a spectrophotometer. As shown in **Figure 8,** the difference of the optical path of two reflected light rays from front surface and the opposite surface depending on the film thickness give the interference. And, number of the interference wave crests enable the calculation of thickness. This measurement requires enough flatness, and too rough surface will influence the intensity of the interference.

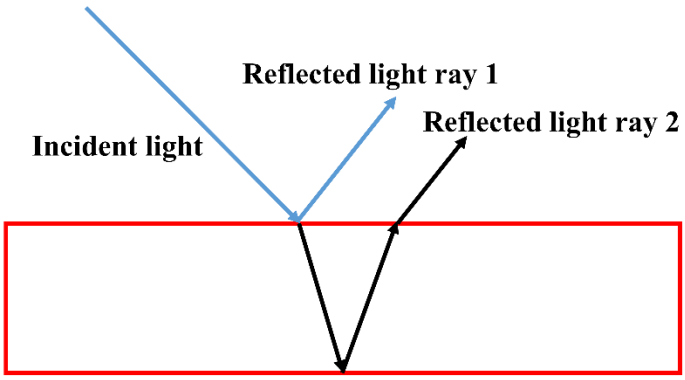

Figure 8. Schematic of the optical mechanism behind the general thin-film thickness measurement.

References

1. Foley, B. J.; Girard, J.; Sorenson, B. A.; Chen, A. Z.; Niezgoda, J. S.; Alpert, M. R.; Harper, A. F.; Smilgies, D.-M.; Clancy, P.; Saidi, W. A., Controlling nucleation, growth, and orientation of metal halide perovskite thin films with rationally selected additives. *Journal of Materials Chemistry A* **2017,** 5, (1), 113-123.

2. Venables, J.; Spiller, G.; Hanbucken, M., Nucleation and growth of thin films. *Reports on Progress in Physics* **1984,** 47, (4), 399.

3. Wang, J.; Xue, J.; Wan, D.; Gan, B., Mechanically activating nucleation and growth of complex perovskites. *Journal of Solid State Chemistry* **2000,** 154, (2), 321-328.

4. Bi, C.; Wang, Q.; Shao, Y.; Yuan, Y.; Xiao, Z.; Huang, J., Non-wetting surface-driven high-aspect-ratio crystalline grain growth for efficient hybrid perovskite solar cells. *Nature communications* **2015,** 6, 7747.

5. Ball, J. M.; Lee, M. M.; Hey, A.; Snaith, H. J., Low-temperature processed meso-superstructured to thin-film perovskite solar cells. *Energy & Environmental Science* **2013,** 6, (6), 1739-1743.

6. Zhou, H.; Chen, Q.; Li, G.; Luo, S.; Song, T.-b.; Duan, H.-S.; Hong, Z.; You, J.; Liu, Y.; Yang, Y., Interface engineering of highly efficient perovskite solar cells. *Science* **2014,** 345, (6196), 542-546.

7. Jeon, N. J.; Noh, J. H.; Kim, Y. C.; Yang, W. S.; Ryu, S.; Seok, S. I., Solvent engineering for high-performance inorganic–organic hybrid perovskite solar cells. *Nature materials* **2014,** 13, (9), 897.

8. Hanaor, D.; Triani, G.; Sorrell, C., Morphology and photocatalytic activity of highly oriented mixed phase titanium dioxide thin films. *Surface and Coatings Technology* **2011,** 205, (12), 3658-3664.

9. Eperon, G. E.; Burlakov, V. M.; Docampo, P.; Goriely, A.; Snaith, H. J., Morphological control for high performance, solution‐processed planar heterojunction perovskite solar cells. *Advanced Functional Materials* **2014,** 24, (1), 151-157.

10. Im, J.-H.; Kim, H.-S.; Park, N.-G., Morphology-photovoltaic property correlation in perovskite solar cells: One-step versus two-step deposition of CH3NH3PbI3. *Apl Materials* **2014,** 2, (8), 081510.

11. Yeh, N.-C.; Fu, C.-C.; Wei, J.; Vasquez, R.; Huynh, J.; Maurer, S.; Beach, G.; Beam, D., Effects of lattice distortion on the physical properties and surface morphology of

magnetoresistive perovskite epitaxial films. *Journal of applied physics* **1997,** 81, (8), 5499-5501.

12. Binnig, G.; Rohrer, H., Scanning tunneling microscopy. *Surface science* **1983,** 126, (1-3), 236-244.

13. Binnig, G.; Rohrer, H., Scanning tunneling microscopy. *IBM Journal of research and development* **2000,** 44, (1/2), 279.

14. Hansma, P. K.; Tersoff, J., Scanning tunneling microscopy. *Journal of Applied Physics* **1987,** 61, (2), R1-R24.

15. Park, S. i.; Quate, C., Scanning tunneling microscope. *Review of scientific instruments* **1987,** 58, (11), 2010-2017.

16. Binnig, G.; Rohrer, H., Scanning tunneling microscopy. *Physica B+ C* **1984,** 127, (1-3), 37-45.

17. Lightman, E. J.; McCarthy, P. M.; Dufty, D. F.; McNamara, D. S. In *Cohesion and Structural Organization in High School Texts*, FLAIRS Conference, 2007; 2007; pp 235-240.

18. McNaught, A. D.; McNaught, A. D., *Compendium of chemical terminology*. Blackwell Science Oxford: 1997; Vol. 1669.

19. Antoine, R.; Dugourd, P., Visible and ultraviolet spectroscopy of gas phase protein ions. *Physical Chemistry Chemical Physics* **2011,** 13, (37), 16494-16509.

20. Fabian, J.; Hartmann, H., *Light absorption of organic colorants: theoretical treatment and empirical rules*. Springer Science & Business Media: 2013; Vol. 12.

21. Rowlett, R., *How Many?: A Dictionary of Units of Measurement*. R. Rowlett: 2005.

3. Transparent conductive oxide layer less back-contacted hybrid perovskite solar cell

3.1 Introduction of TCO-less perovskite solar cells

Recent years have witnessed the hybrid perovskite (PVK) solar cells (SCs) as one of the most promising solar cells because of the high photoconversion efficiencies[1-4]. Transparent conductive oxide layer (TCO) is typically needed in the conventional perovskite SCs. However, complex equipment and process are necessary for the fabrication of the TCO layer. Meanwhile, it leads to the loss of incident light on the active layer, when passing though the TCO layer. In order to overcome these issues, initial reports provide a back-contacted architecture device[5-7], which has been frequently reported in the silicon-based solar cells[8,9] and dye-sensitized solar cells[10-12]. Both of the electrodes are located at the same side of the light absorber layer in these proposed device architectures and the recently reported Back-contacted PVK solar cells with quasi-interdigitated electrode (QIDE) have the photoconversion efficiency of 3.2 %[13]. However, the involved photolithographic technology adopted for fabrication is the bottle-necks for the large scale production. In addition, typically PVK SCs comprise the hole selective layers (HSL) such as Spiro-OMeTAD(N^2,N^2,$N^{2'}$,$N^{2'}$,N^7,N^7,$N^{7'}$,$N^{7'}$-octakis(4-methoxyphenyl)-9,9′-spirobi[9H-fluorene]-2,2′,7,7′-tetramine), PTAA(Poly(bis(4-phenyl)(2,,4,6-trymethylphenyl)amine) and PEDOT:PSS(poly(3,4-ethylene dioxythiophene):poly(styrene sulfonate), which are costly and unstable[14]. Herein, a novel back-contacted perovskite (PVK) SC without TCO and HSL is presented.

3.2 Experimental section

Figure 1 shows the detail schematic fabrication processes of TCO & HSL free back-contacted hybrid perovskite SCs, which are composed of glass/mesoporous-TiO_2 &PVK/porous-Ti with native oxide&PVK/mesoporous ZrO_2&PVK/gold. A clean glass substrate was deposited about 1 μm thick mesoporous TiO_2 layer (particle diameter: 250 nm) by spin-coating (**Figure 1i**) and then successively sintered at 500 ^{0}C for 1.3h (**Figure 1ii**). After that, network-like porous Ti with 30nm-80nm thickness was formed by sputtering (CFS-4EP-LL, Shibaura Mechatronics) with lower than $1*10^{-4}$ Pa pressure, 250 W power and Ti target in Ar atmosphere at room temperature. The deposition rate

was about 5nm/min. A thin native oxide layer (compact TiO_2) on the Ti surface was automatically formed during this step.

Then, a mesoporous ZrO_2 layer with thickness of about 150 nm (particle diameter: 30 nm) was spin coated on the sample (**Figure 1iv**) and the sample was annealled at 400 ^{0}C (**Figure 1v**) for 1-2 h.

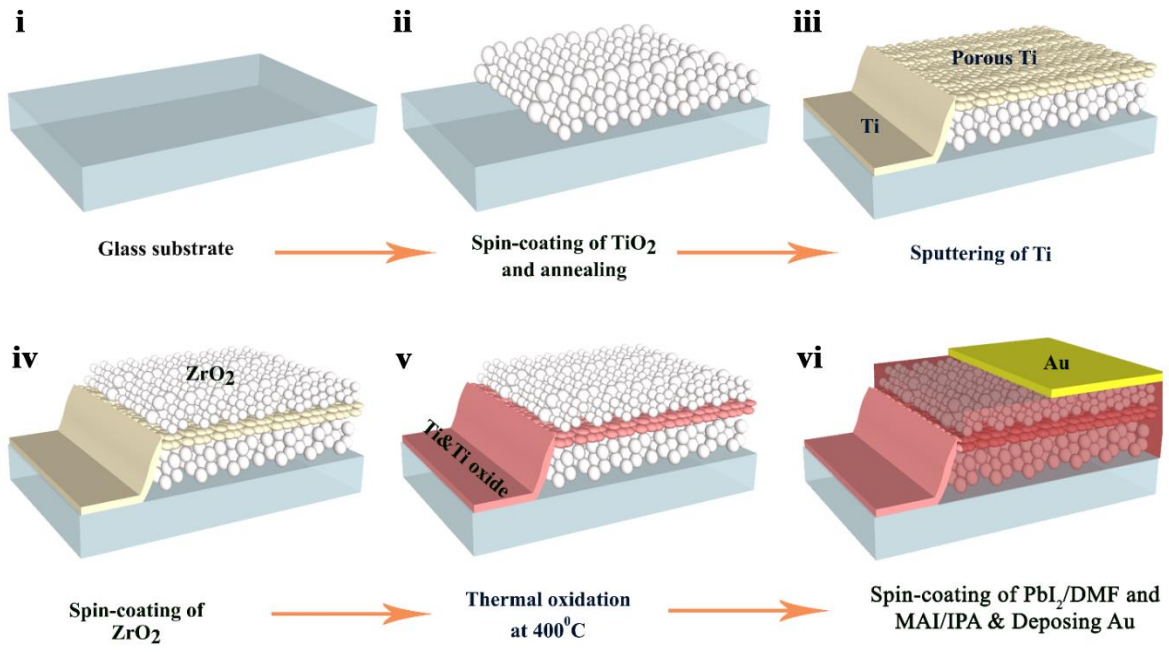

Figure 1. Fabrication process of TCO&HSL free back contacted hybrid perovskite solar cell.[26]

This annealing step forms not only solid ZrO_2 but also further thermally oxidize Ti surface to increase the thickness of the compact native oxide layer on the surface of Ti metal. [15]

Two-step spin-coating method was used to prepare $CH_3NH_3PbI_3$ perovskite layer (**Figure 1vi**). First, precursor solution were prepared by dissolving 460 mg of PbI_2 in 1 ml N,N-dimethylformamide (DMF) at 70 ^{0}C and 500 mg of CH_3NH_3I (MAI) in 60 ml isopropanol (IPA) at room temperature.

Samples were prepared by a sequential two-step deposition method, which has been reported for the preparation of PVK crystals giving the high photovoltaic performance[16,17]. First, PbI_2 solution were spin-coated at 500 rpm for 5 s, followed by 6000 rpm for 10 s and then the sample was kept at 70 ^{0}C for 30 min. The sample was then immerged in MAI solution for 30 s to completely react with PbI_2, and then quickly

immerged in IPA for 20 s for removing the remaining MAI. Finally, 100 nm thick gold was deposited by thermal evaporation. Solar cell performances were evaluated using a solar simulator (CEP-2000SRR, Bunkoukeiki Inc., AM 1.5G 100 $mWcm^{-2}$) and a black mask was employed on top of the devices with exposure area of 0.12 cm^2.

3.3 Results and discussion

Figure 2a shows the architecture of TCO&HSL free back-contacted hybrid perovskite SCs.

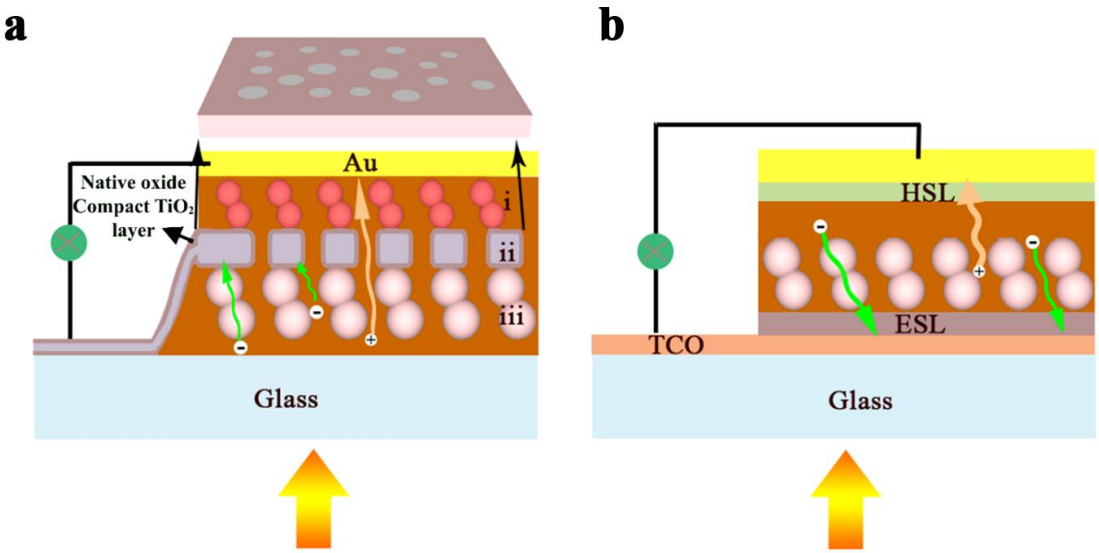

Figure 2. (a) TCO & HSL free back-contacted hybrid perovskite solar cell. In the structure, layer i ,ii and iii are mesoporous ZrO_2 filled with PVK, network-like porous Ti with native oxide filled with PVK, mesoporous TiO_2 filled with PVK, respectively. (b) Conventional PVK solar cell.[26]

Light coming from the glass side is absorbed by PVK filled in TiO_2 layer (**Figure 2a iii**). In back-contacted structures, TCO typically used in the sandwich structure of conventional PVK SCs (**Figure 2b**) is not necessary[10,11], which avoids the transmission loss caused by TCO. Compared to the initial IDE based back-contacted SCs. Network-like porous Ti (**Figure 2a ii**) is utilized as the back-contacted electrode because Ti and native oxide on the surface can selectively collect electrons. The generated hole carriers are diffused via the PVK filled in the porous ZrO_2 layer and collected by gold electrode. Mesoporous ZrO_2 is inserted between two electrodes to isolate them, (**Figure 2a i**) which effectively avoid the short circuit.

The carrier collection mechanism is shown in **Figure 3**. The conduction bands of PVK, compact native oxide layer on Ti (compact TiO_2), and Ti are -3.9 eV, -4.0 eV, -4.3 eV, respectively. Photogenerated holes diffuse in the PVK filling these triple porous layer, and are finally collected by Au electrode, since PVK fills these nanopores of consecutively fabricated TiO_2 layer, Ti layer and ZrO_2 layer. Additionally, valence band (-7.2 eV) of TiO_2 is deeper than that of PVK, holes are kicked out from the porous Ti electrode surface, and are selectively collected by Au electrode.

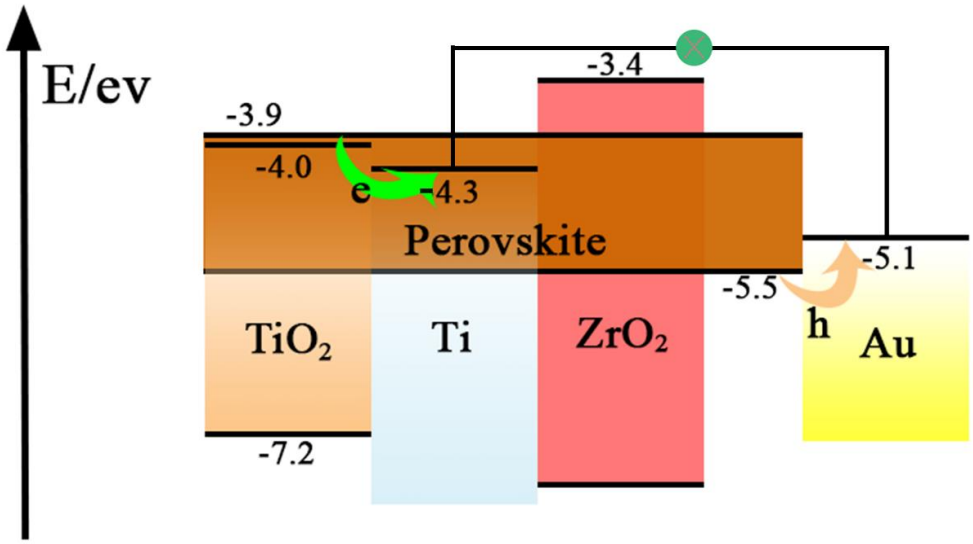

Figure 3. Band diagram of the TCO&HSL free back-contacted hybrid perovskite SC. Energies are expressed in electron volts from vacuum level.[26]

There is a possibility of the enhanced recombination of these carriers in this device architecture since the holes and electrons diffuse in the same direction as shown in **Figure 2**. Therefore, the structure of back-contacted electrode, which collects electrons selectively is very important. **Figure 4** shows the scanning electron microscopic (SEM) images of this network-like porous Ti. It possesses about 250 nm gaps shown in **Figure 4a and Figure 4b**. Considering electron diffusion length of 1 micron, it is quite suitable. The interconnected Ti allowed a high conductivity for collecting electrons.

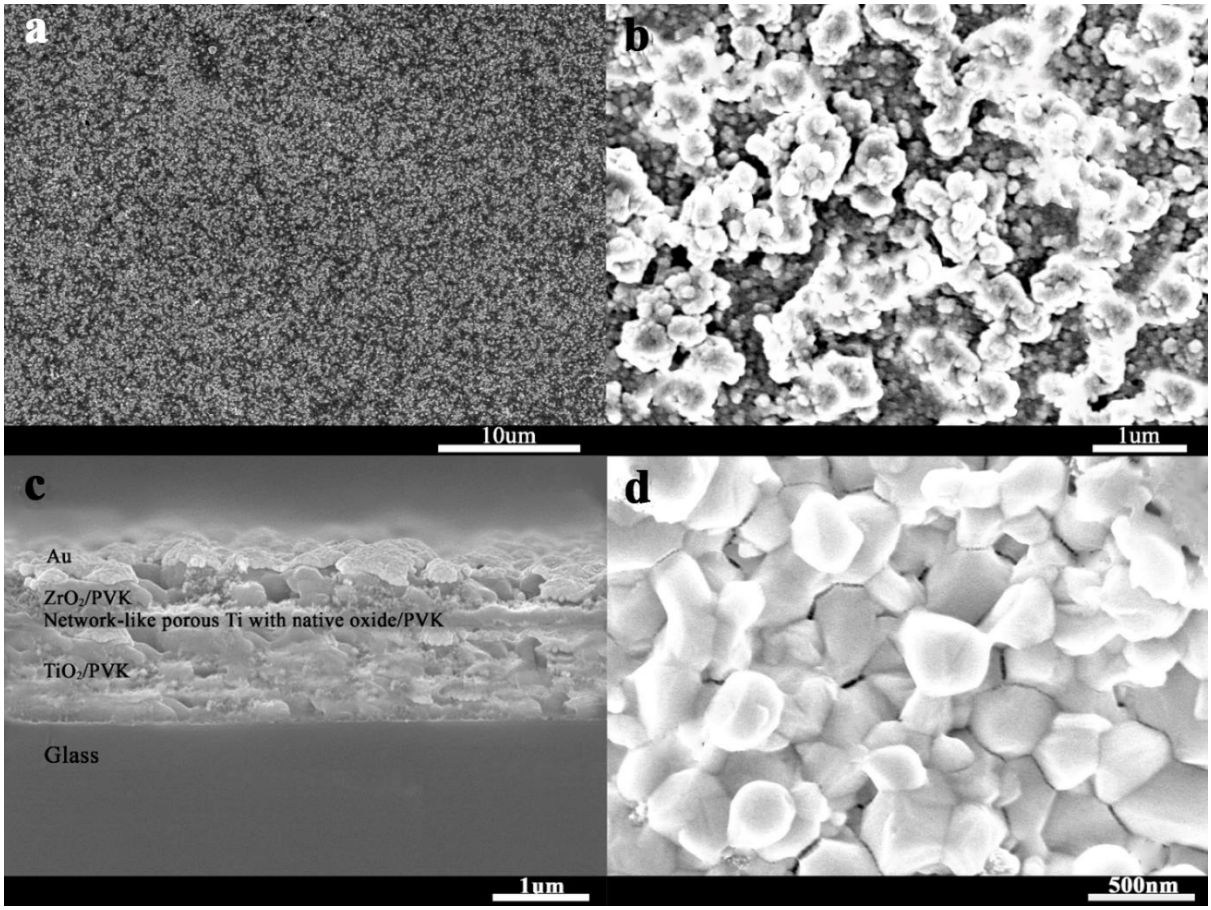

Figure 4. (a) SEM image of network-like porous Ti on porous TiO_2 layer (diameter: 250 nm), (b) Expanded SEM image of network-like porous Ti on porous TiO_2. In the SEM image of porous Ti fabricated on porous titania layer (top view), porous titania particles can be seen in the area uncovered by networked Ti. (c) Cross section SEM image of TCO & HSL free back-contacted perovskite SCs including triple mesoporous layers filled with PVK and (d) Top view SEM image of perovskite on ZrO_2/PVK layer.[26]

In addition, the nano-porous Ti was filled with PVK (**Figure 4d**) for carrying holes. [18,19]. **Figure 4c** shows the SEM cross-section of the complete device. Triple layers of 1 μm TiO_2, 30-80 nm Ti and 150 nm ZrO_2 porous layers are observed. This triple porous layers with a total thickness of about 1.2 μm is almost same as carriers diffusion length previously reported[20-23]. Sheet resistance in the back contacted solar cells plays a crucial role to effective collect carriers. Four point probe method was used to measure the sheet resistance. **Figure 5a** indicates that sheet resistance decreased with increasing thickness and saturated at 60 nm thickness with 11 ohms/sq.

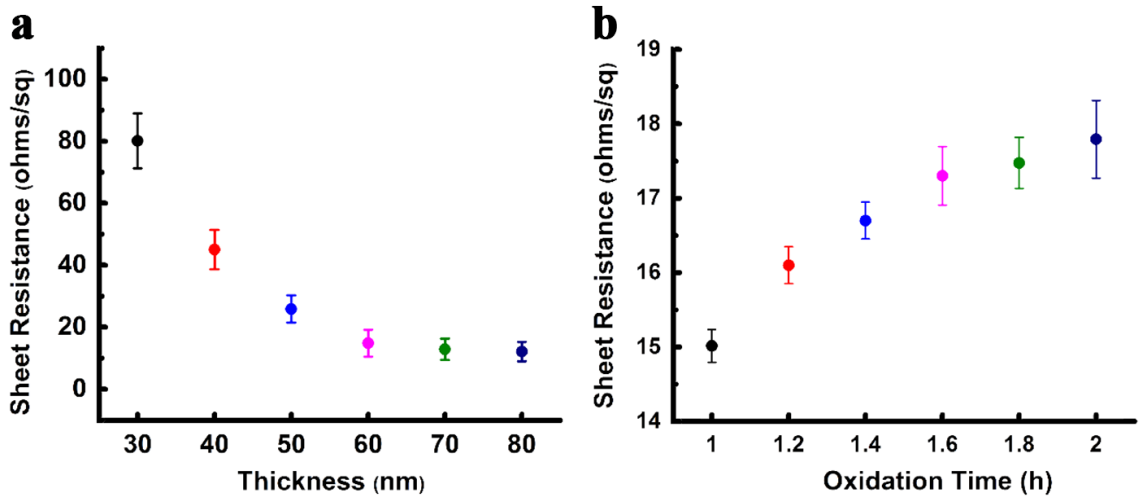

Figure 5. (a) Dependence of the thickness on the sheet resistance of Porous Ti layer on porous TiO_2 layer. (b) Dependence of baking time on the statistical sheet resistance of network-like porous Ti with 60nm thickness on porous TiO_2 layer.[26]

Figure 2 and **Figure 3** show that light is introduced from TiO_2 side and directly harvested by the perovskite filled in the mesoporous TiO_2. It must be noted that large nano-particles of TiO_2 as mesoporous layer have to be employed as shown in **Figure 6.** The average size is about 250 nm. This large size NPs lead to rough surface compared to small NPs.

The proper roughness on porous TiO_2 gives network like Ti on the porous TiO_2 layer. To suppress the charge recombination, native TiO_2 layer fabricated on Ti by thermal treatment is necessary. The resistivity is also affected by the baking conditions (**Figure 5b**). The long baking time thick the thickness, which increase the resistivity. After 1.6 h, the slow increase of the rate of the sheet resistance of the Ti electrode with the increasing oxidation time indicates that Ti surface is almost completely covered with oxide layer. Formation of enough thick TiO_2 blocking layer on Ti metal is a conflicting issue to increasing the conductivity of Ti electrode.

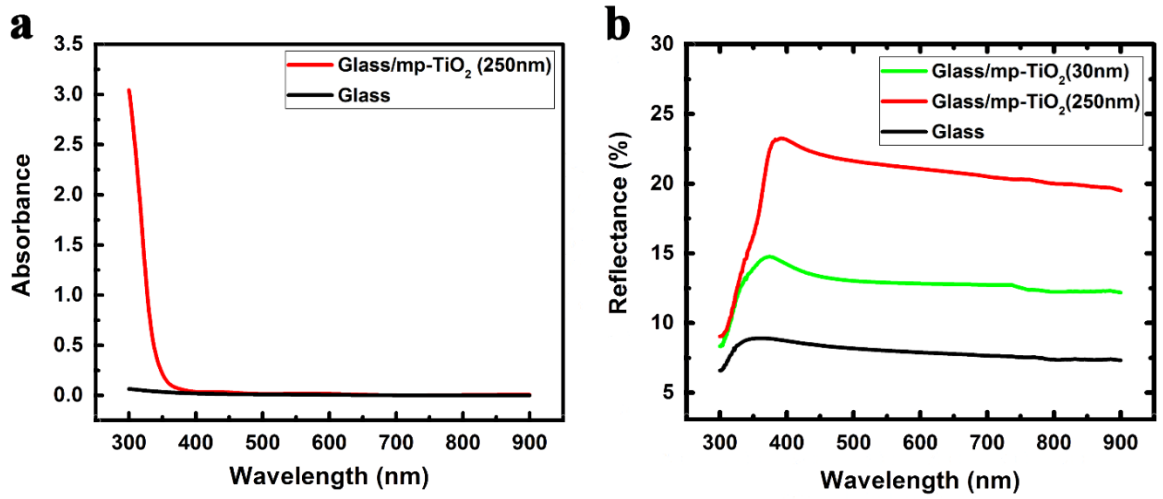

Figure 6. (a) Light absorption and (b) reflectance spectrum of mesoporous TiO_2 (250 nm) on glass.[26]

Systematic investigations concerning the Ti thickness and the thermal oxidation time was conducted aiming at their implications on the photovoltaic performances to determine the optimized parameter of TCO & HSL free back-contacted structure. Four main parameters of performance of SCs including power conversion efficiency (PCE), short-circuit current density (Jsc), fill factor (FF) and open-circuit voltage (Voc) were measured respectively. Result in **Figure 7** reveals that the optimum Ti thickness is 60 nm. As shown in **Figure 5a,** the sharp increase in the sheet resistance of the Ti layer illustrates that Ti thickness less than 60 nm drastically hampers efficiency for the electron collection. Meanwhile, thickness thicker than 60 nm obviously reduce the gap size of porous Ti layer becomes more compact, which in turn reduce the PCE, FF, Jsc and Voc (**Figure 7c**) seriously.[10,11] As shown in **Figure 7b and Figure 7d,** thermal oxidation time was also tuned to obtain high performance. Obvious change in the photovoltaic parameters were found, which demonstrates that thermal oxidation time is crucial to control the device performance by forming a compact oxide layer, which covers completely on Ti metal. The optimized thermal oxidation time was 1.8 h. Prolonged oxidation time, leads to forming thicker TiO_2 on surface which increases higher resistance and reduces the device performance.

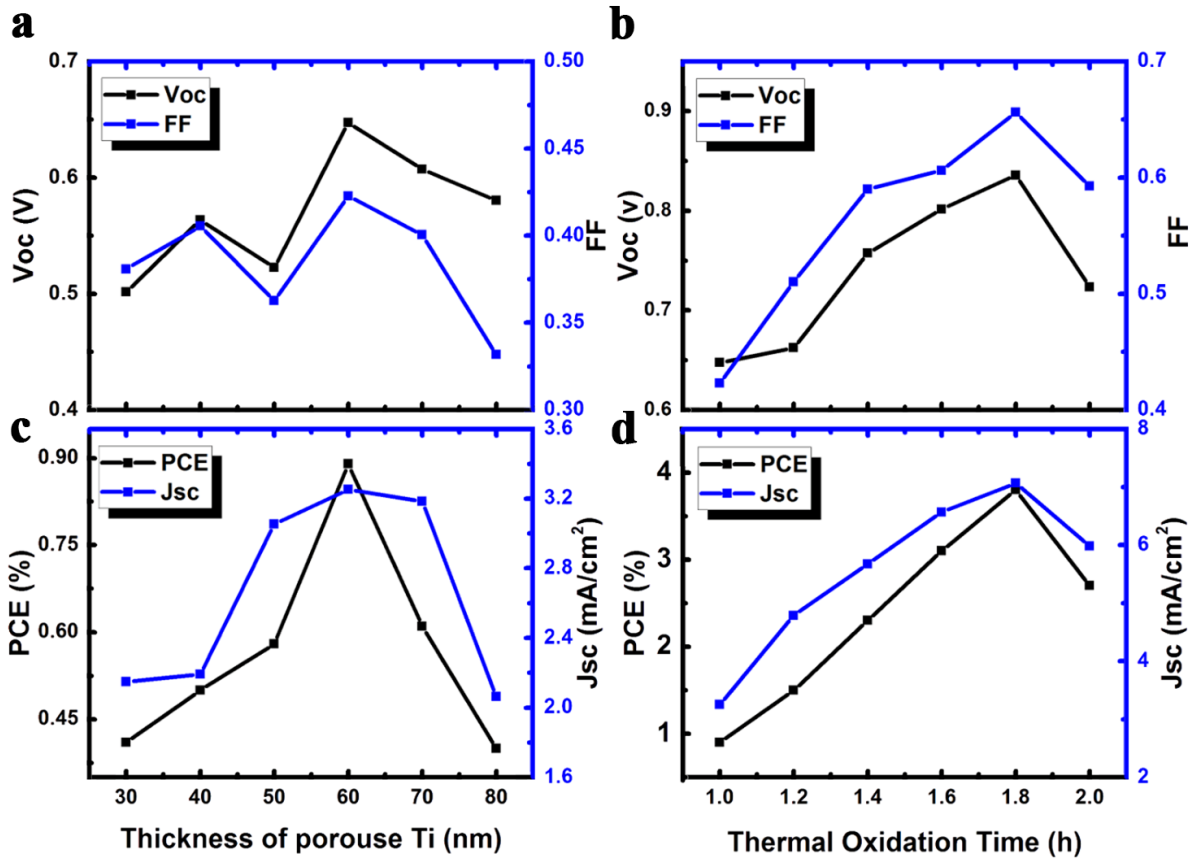

Figure 7. Dependence of thickness of porous Ti upon (a) Voc, FF and (c) PCE, Jsc. Dependence of thermal oxidation time on (b) Voc, FF and (d) PCE, Jsc.[26]

Figure 8a shows the J-V characteristics in forward and reverse scan modes with illumination at 1 Sun. A mask with light exposure area of 0.12 cm^2 covered the devices during the measurement. The values of the Jsc, Voc and FF were found to be 7.07 mA/cm^2, 0.84 V and 0.66, respectively in forward scan mode (0V → Voc). For the reverse scan mode (Voc → 0V), Jsc, Voc and FF were 7.10 mA/cm^2, 0.83 V and 0.66, respectively. Both of the forward as well as reverse scan mode gives the same PCEs of 3.88 %. It did not show hysteresis phenomenon, which has been reported frequently in the perovskite solar cells.[24,25]

To further characterize the separation of generated carriers in ZrO_2 layer, we investigated the device with the HTM (spiro-OMeTAD) inserted between mesoporous ZrO_2/PVK and gold electrode.

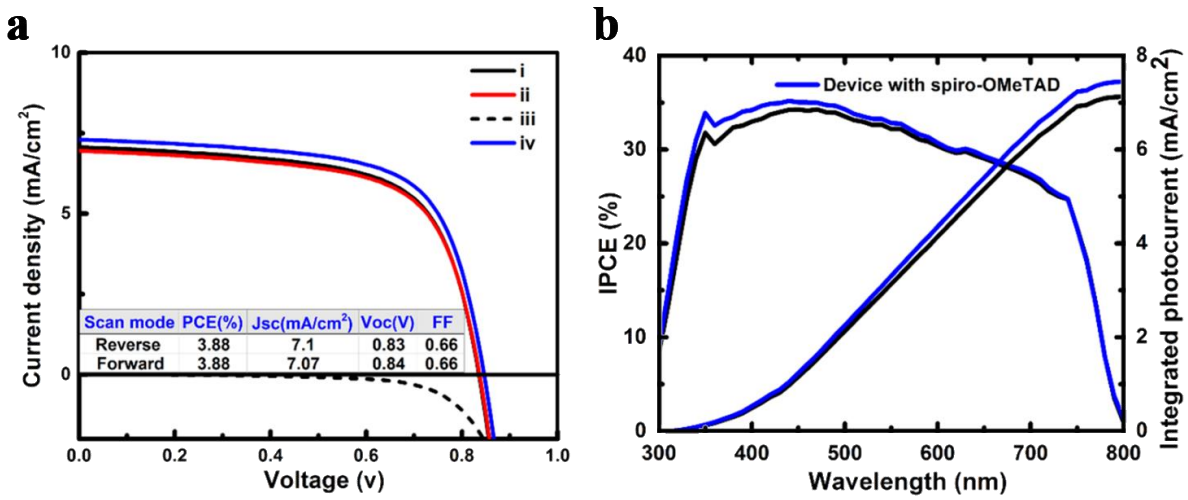

Figure 8. (a) J-V curves of the devices under simulated AM 1.5 solar irradiation measured at room temperature. i) reverse scan, ii) forward scan, iii) dark mode and iv) device with spiro-OMeTAD. (b) IPCE and integrated photocurrent of the devices in the presence and absence of spiro-OMeTAD.[26]

The IV curve in **Figure 8a** shows 4.02 % efficiency, which is little larger than 3.88 % of the device without HTM. The tiny difference in the photovoltaic performance along with the incident photon to current conversion efficiency (IPCE) as shown in the **Figure 8b** indicates that generated electron-hole pairs are completely separated in TCO & HSL free back-contacted structure.

Finally, to test the stability of this new structure, data including PCE, Voc , FF and Jsc were recorded every 120 hours under light intensity of 100 mW cm^{-2} in ambient conditions with complete devices without encapsulation. **Figure 9a-b** and **Figure 9c-d** demonstrate that for the absence of HTM, only 9.6 % of PCE of devices decayed over 1080 hours presenting an excellent stability, while more sharply decays were observed in the devices with Spiro-OMeTAD. The performance of the device without HTM even exceeded the devices with Spiro-OMeTAD after the storage for 480 hours. This is mainly attributable to the unstable HTM (Spiro-OMeTAD). Compared to the conventional structure of perovskite solar cells, the obtained performance is still low. One of these reasons may be the relatively high sheet resistance, 17.5 ohms/sq of porous Ti with oxide on the surface, compared to that of around 10 ohms/sq for the usually employed TCO substrate. Additionally, the diffusion length for the hole carrier via PVKs filled in the porous may be shorter than the whole thickness of triple layers. Therefore, higher efficiency can be expected by optimization the triple layers.

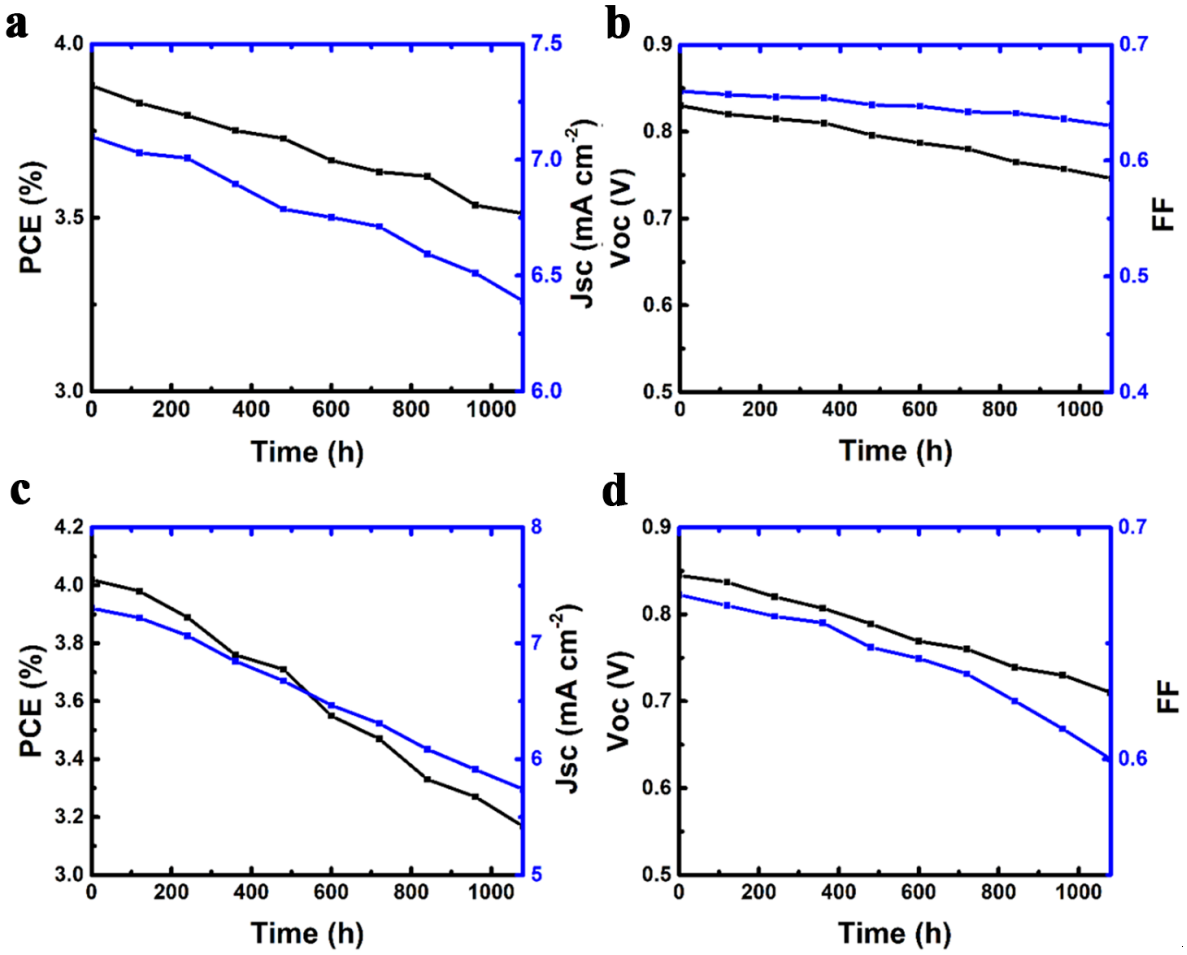

Figure 9. Photovoltaic performance change during storage of (a)-(b) TCO and HSL free back-contacted perovskite solar cells and (c)-(d) perovskite solar cells with sipro-OMeTAD under light intensity of 100 mW cm^{-2}.[26]

3.4 Conclusions

In conclusion, a novel back-contacted perovskite solar cell device architecture without employing TCO and HSL was presented. The highest PCE of 3.88% under air conditions. The cells showed an excellent long-term stability. We also gave a fabrication method of porous Ti electrode, which was accomplished by sputtering Ti on mesoporous TiO_2 layer with big particle size. We confirmed that large particles of TiO_2 gave the porous Ti with appropriate nano-space. PVK filled in the nanopores in triple porous layers were crucial for collection and separation of the generated carriers. The influence of Ti thickness and thermal oxidation time on the performance of SCs were investigated, which indicates that the completely porous Ti electrode with native oxide was very important for the reduction of charge recombination between

electrons in Ti and holes in PVK. Better performance can be expected by optimization triple porous structures.

References

1. Xiao, Y.; Han, G.; Chang, Y.; Zhou, H.; Li, M.; Li, Y. An all-solid-state perovskite-sensitized solar cell based on the dual function polyaniline as the sensitizer and p-type hole-transporting material. *J. Power Sources* **2014**, (267), 1-8.

2. Sheikh, A. D.; Bera, A.; Haque, M. A.; Rakhi, R. B.; Gobbo, S. D.; Alshareef, H. N.; Wua, T. Atmospheric effects on the photovoltaic performance of hybrid perovskite solar cells. *Sol. Energ. Mat. Sol. C* **2015**, (137), 6-14.

3. Lang, L.; Yang, J.-H.; Liu, H.-R.; Xiang, H. J.; Gong, X. G. First-principles study on the electronic and optical properties of cubic ABX3 halide perovskites. *Phys. Lett. A* **2014**, (378), 290-293.

4. Sakai, N.; Pathak, S.; Chen, H.-W.; Haghighirad, A. A.; Stranks, S. D.; Miyasak, T.; Snaith, H. J. The mechanism of toluene-assisted crystallization of organic–inorganic perovskites for highly efficient solar cells. *J. Mater. Chem. A* **2016**, (4), 4464-4471.

5. Nie, W.; Tsai, H.; Asadpour, R.; Blancon, J.-C.; Neukirch, A. J.; Gupta, G.; Crochet, J. J.; Chhowalla, M.; Tretiak, S.; Alam, M. A.; et al. High-efficiency solution-processed perovskite solar cells with millimeter-scale grains. *Science* **2015**, (347), 522-525.

6. Zhang, W.; Anaya, M.; Lozano, G.; Calvo, M. E.; Johnston, M.l B.; Míguez, H.; Snaith, H. J. Highly Efficient Perovskite Solar Cells with Tunable Structural Color. *Nano Lett.* **2015**, (15), 1698-1702.

7. Nagarjuna, P.; Narayanaswamy, K.; Swetha, T.; Hanumantha Rao, G.; Singh, S. P.; Sharma, G.D. CH3NH3PbI3 Perovskite Sensitized Solar Cells Using a D-A Copolymer as Hole Transport Material. *Electrochim. Acta* **2015**, (151*)*, 21-26.

8. Savin, H.; Repo, P.; Gastrow, G. v.; Ortega, P.; Calle, E.; Garín, M.; Alcubilla, R.; Black silicon solar cells with interdigitated back-contacts achieve 22.1% efficiency. *Nat. Nanotechnology* **2015**, (10), 624-628.

9. Jeong, S.; McGehee, M. D.; Cui, Y. All-back-contact ultra-thin silicon nanocone solar cells with 13.7% power conversion efficiency. *Nat. Commun.* **2013**, (4), 1-7.

10. Fuke, N.; Fukui, A.; Komiya, R.; Islam, A.; Chiba, Y.; Yanagida, M.; Yamanaka, R.; Han, L. New Approach to Low-Cost Dye-Sensitized Solar Cells With Back Contact Electrodes. *Chem. Mater.* **2008**, (20), 4974-4979.

11. Nishio, Y.; Yamaguchi, T.; Yamguchi, T.; Nishio, K.; Hayase, S. Transparent conductive oxide-less dye-sensitized solar cells (TCO-less DSSC) with titanium nitride compact layer on back contact Ti metal mesh. *J. Appl. Electrochem.* **2016**, (46), 551-557.

12. Fu, D.; Zhang, X. L.; Barber, R. L; Bach, U.; Adv. Mater. Dye-Sensitized Back-Contact *Solar Cells* **2010**, (22), 4270-4274.

13. Jumabekov, A. N.; Della Gaspera, E.; Xu, Z.-Q.; Chesman, A. S. R.; van Embden, J.; Bonke, S. A.; Bao, Q.; Vaka, D.; Bach, U. Back-Contacted Hybrid Organic-Inorganic Perovskite Solar Cells. *J. Mater. Chem. C* **2016**, (*0*0), 1-3.

14. Mei, A.; Li, X.; Liu, L.; Ku, Z.; Liu, T.; Rong, Y.; Xu, M.; Hu, M.; Chen, J.; Yang, Y.; et al. A hole-conductor–free, fully printable mesoscopic perovskite solar cell with high stability. *Science* **2014**, (345), 295-298.

15. Sartale, S.D.; Ansari, A.A.; Rezvani, S.-J. Influence of Ti film thickness and oxidation temperature on TiO2 thin film formation via thermal oxidation of sputtered Ti film. *Mat. Sci. Semicon. Proc* **2013**, (16), 2005-2012.

16. El-Henawey, M. I.; Gebhardt, R. S.; El-Tonsy, M. M.; Chaudhary, S. Organic solvent vapor treatment of lead iodide layers in the two-step sequential deposition of CH3NH3PbI3-based perovskite solar cells. *J. Mater. Chem. A* **2016**, (4), 1947-1952.

17. Burschka, J.; Pellet, N.; Moon, S.-J.; Humphry-Baker, R.; Gao, P.; M. Nazeeruddin, K.; Gra¨tzel, M. Sequential deposition as a route to high-performance perovskite-sensitized solar cells. *Nature* **2013**, (499), 316-319.

18. Xie, W.; Chen, J.; Jiang, L.; Yang, P.; Sun, H.; Huang, N. Nanomesh of Cu fabricated by combining nanosphere lithography and high power pulsed magnetron sputtering and a preliminary study about its function. *Appl. Surf. Sci.* **2013**, (283), 100-106.

19. Torrisi, V.; Ruffino, F. Metal-Polymer Nanocomposites: (Co-)Evaporation/(Co)Sputtering Approaches and Electrical Properties. *Coatings* **2015**, (5), 378-424.

20. Xing, G.; Mathews, N.; Sun, S.; Lim, S. S.; Lam, Y. M.; Grätzel, M.; Mhaisalkar, S.; Sum, T. C. Long-Range Balanced Electron- and Hole-Transport Lengths in Organic-Inorganic CH3NH3PbI3. *Science* **2013**, (342), 344-347.

21. Stranks, S. D.; Eperon, G. E.; Grancini, G.; Menelaou, C.; M. Alcocer, J. P.; Leijtens, T.; Herz, L. M.; Petrozza, A.; Snaith, H. J. Electron-Hole Diffusion Lengths Exceeding 1 Micrometer in an Organometal Trihalide Perovskite Absorber. *Science* **2013**, (342), 341-344.

22. Dong, Q.; Fang, Y.; Shao, Y.; Mulligan, P.; Qiu, J.; Cao, L.; Huang, J. Electron-hole diffusion lengths > 175 μm in solution-grown CH3NH3PbI3 single crystals. *Science* **2015**, (347), 967-970.

23. Shi, D.; Adinolfi, V.; Comin, R.; Yuan, M.; Alarousu, E.; Buin, A.; Chen, Y.; Hoogland, S.; Rothenberger, A.; Katsiev, K.; et al. Low trap-state density and long carrier diffusion in organolead trihalide perovskite single crystals. *Science* **2015**, (347), 519-522.
24. Tripathi, N.; Yanagida, M.; Shirai, Y.; Masuda, T.; Han, L.; Miyano, K. Hysteresis-free and highly stable perovskite solar cells produced via a chlorine-mediated interdiffusion method. *J. Mater. Chem. A* **2015**, (3), 12081-12088.
25. Yoon, H.; Kang, S. M.; Lee, J.-K.; Choi, M. Hysteresis-free low-temperature-processed planar perovskite solar cells with 19.1% efficiency. *Energy Environ. Sci.* **2016**, (9), 2262-2266.
26. Hu, Z.; Kapil, G.; Shimazaki, H.; Pandey, S.-S.; Ma, T.; Hayase, S.; Transparent Conductive Oxide Layer and Hole Selective Layer Free Back-Contacted Hybrid Perovskite Solar Cell, *The Journal of Physical Chemistry C* **2017**, (8), 4214-4219.

4. Interparticle coupling effect of silver-gold hetero-dimer to enhance light-harvesting in ultrathin perovskite solar cell

4.1 Introduction

The metallic nanoparticles (NPs) and their applied plasmonic solar cells are under intensive interest to enhance the performance of all types of photovoltaics including silicon solar cells,[1-3] dye sensitized solar cells,[4-6] and organic solar cells.[7, 8] Metal halide organic-inorganic perovskite are no exception.[9-11] Since the extinction coefficient rapidly decays for long-wavelength regions, it is needed to uptake these weak light effectively. [12-16].

Initial studies are forced on the incorporating noncoupling NPs in a perovskite film and utilizes the light scattering of NPs to enhance the absorption[17]. However, the recent plasmonic perovskite devices by incorporating noncoupling metal NPs cannot give comparable power conversion efficiency with the normal devices. Large size NPs are definitely needed to support the obvious absorption enhancement for the scattering cross section is directly proportional to the size of NP. And larger than 120 nm diameter silver NPs have been theoretically suggested for the better scattering.[17] But, the thickness of the thin perovskite film limit the maximum size of the embedded particles. All the above factors motivated the development of new method to further enhance the optical absorption. Interparticle plasmon coupling including dimers and multi-body of metal NPs is the more effective method and has been introduced to high-performance polymer solar cells,[18] utilizing the produced enhanced electromagnetic field near the surface and especially strong coupling of localized surface plasmon resonance (LSPR) of NPs inside the gap.[19] But the recently reported perovskite films with the embedded gold homo-dimer[20] in 200 nm thickness perovskite film having only 10% improvement of performance and the efficency is still incomparable with the perovskite with normal thickness.

Herein, an ultrathin perovskite film with the embedded hetero-dimer was investigated to enhance the absorption of the surrounding perovskite and compared to the reported homo-dimer.

4.2 Computational details

4.2.1 Plasmon dipolar-dipolar coupling of dimers in perovskite

The interaction of dipolar moment of each nanosphere $\mu = \alpha\epsilon_p E$, can be applied in the plasmon coupling of dimers surrounded with perovskite [21]. The scattering cross scattering of dimers can be obtained by

$$\begin{cases} S_{cs} = k^4|\alpha_{total}|^2/(6\pi) \\ \alpha_{total} = \frac{\alpha_1[1+\kappa\alpha_2/(4\pi\varepsilon_0 d^3)]+\alpha_2[1+\kappa\alpha_1/(4\pi\varepsilon_0 d^3)]}{1-[\kappa/(4\pi\varepsilon_0 d^3)]^2\alpha_1\alpha_2} \end{cases} \quad (1)$$

where κ is the orientation factor relating to the arrangement of dipolar moments, which equals to -1 for side-by-side (the polarity of light perpendicular with dimer) and $\kappa = 2$ for head-to-tail arrangement (the polarity of light parallel with dimer). α is the clausius-Mossotti dipole polarizability, which can be estimated by

$$\alpha = 3\varepsilon_0 v(\frac{\varepsilon_m - \varepsilon_p}{\varepsilon_m + 2\epsilon_p}) \quad (2)$$

where ϵ_0, ϵ_m and ε_p are the dielectric constant of vacuum, metal and perovskite respectively. In addition, we selected silver and gold as the metal materials, which are the reported to be best metal in plasmonic solar cells (SCs).[17, 22] $\alpha_1 = \alpha_2 = \alpha_{ag}$ *or* α_{au} for homo-dimer is expected while for hetero-dimer there is relationship of $\alpha_1 = \alpha_{ag}$ and $\alpha_2 = \alpha_{au}$. **Figure 1** shows the optical constants for perovskite films in highly performing devices.[23, 24]

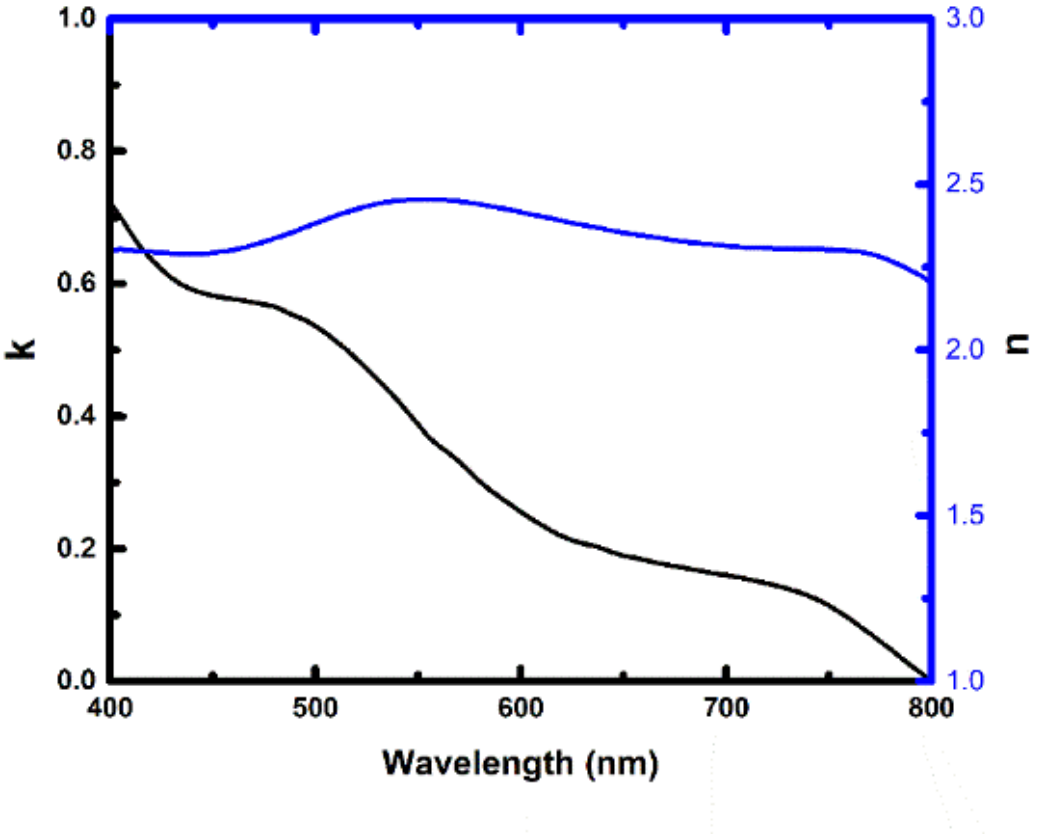

Figure 1. Optical constants for MAPI thin films.[25]

4.2.2 Parameters of Lorentz model for perovskite, gold and silver.

The dispersive materials are expressed through Lorentz model which is the sum of multi-oscillators with multi-frequency. The dispersive material dielectric constant depending on frequency ω is given by

$$\tilde{\varepsilon}(\omega) = \varepsilon_\infty + \sum_{j=1}^{N} \frac{\sigma_j \cdot \omega_j^2}{\omega_j^2 - \omega^2 - i\omega\gamma_j} \quad (3)$$

where the constant ε_∞, σ_j, ω_j and γ_j are the high frequency dielectric constant, oscillator strength term, resonant (peak) energy of the oscillator and the broadening parameter corresponding to each oscillator, respectively. **Table 1-3** give the fitted parameters of perovskite, silver and gold, respectively.

Table 1. Parameters of $MAPbI_3$.[25]

ε_∞=1.7494

σ_j	$\gamma_j(ev)$	$\omega_j(ev)$
0.357894475761153	0.297453902501477	3.57448626772940
0.275388281112334	0.465511818333739	3.15393896290633
0.259294192264127	0.661800902669850	2.88036427571432
0.204848368997525	0.551021804246366	2.61721865958346
1.12088308072804	0.00217811229401565	4.25507506941361
0.134035733893159	0.426903447139061	2.44095769324199
0.0604380089428242	0.332571184013103	2.30214361794593
0.0385139716176764	0.313306792916730	2.15378440491449
0.0373404246293125	0.396537906957354	1.95839427627934
0.0169933561723172	0.230987993919101	1.79017182358615
0.00174215931410905	0.236317889591005	4.39443006654756
0.0181575119991169	0.202613947809829	2.24009760156930
0.00645887756524636	0.113471616209497	1.54980055148749

Table 2. Parameters of silver.[25]

ε_∞=1.0001

σ_j	$\gamma_j(ev)$	$\omega_j(ev)$
4.4625e+39	0.048	1e-20
7.92469618055556	3.886	0.816
0.501327328095750	0.452	4.481
0.0133292250190222	0.065	8.185
0.826552111456641	0.916	9.083
1.11333628041501	2.419	20.29

Silver and Gold parameters are obtained by converting Lorentz-Drude expression mentioned in reference 31

Table 3. Parameters of gold.[25]

ε_∞=1

σ_j	$\gamma_j(ev)$	$\omega_j(ev)$
4.0314e+39	0.053	1e-20
11.3629356945856	0.241	0.415
1.18363913485266	0.345	0.83
0.656770222806431	0.87	2.969
2.64548587658580	2.494	4.304
2.01482623163704	2.214	13.32

4.2.3 FDTD calculation of light absorption

Absorption spectra of a series of perovskites with different thickness can be obtained by

$$Ap = 1 - R - T \quad (4)$$

where R and T are the calculated reflectance and transmittance respectively. Perovskite films with embedded metal NPs with certain period are considered. In this work, we are aiming to discuss the role of inter-particle coupling of the embedded metal nanoparticles on the absorption enhancement. We got rid of the influence of metal reflectance layer, which will reflect the light back into the perovskite and affect the light absorption. Single computational unit cell was therefore designed with three layers, perovskite with the embedded metal NPs (150 nm), hole transport material (Spiro-OMeTAD) of reflective index with n_s=1.732 (thickness: 50 nm) and glass substrate with n_g=1.5 (thickness: 50 nm).[20] Two kinds of models (**Figure 2**) were established, in which noncoupling nanospheres and dimers (hetero-dimer: Ag-Au and homo-dimers: Ag-Ag Au-Au) were put in the center and centrosymmetric positions respectively. The volume concentration of the embedded metal particles in perovskite film was expressed by the filling factor (FF). It can be calculated using

$$FF = \frac{v_{sphere}}{l_x \cdot h_z \cdot w_y} \quad (5)$$

where $v_{sphere} = n \cdot \frac{4}{3}\pi(\frac{d}{2})^3$ is the whole volume of metal nanospheres, n is the number of nanospheres per unit cell and d is the diameter of nanosphere. For the sake of

comparison, same volume concentration of both models are satisfied. The length of the model contained noncoupling nanoparticles is half with the model contained dimers. Three dimensions length l_x=250 nm, thickness h_z=150 nm, width w_y=250 nm. The range of diameter was from 50 nm to 90 nm and FF was from 1.40 % to 8.14 %. Absorption depending on frequency was calculated as follows:

$$A(\omega) = \omega\varepsilon_0 \int |E(r,\omega)|^2 n(\omega) k(\omega)\, dV \quad (6)$$

where ω is the angular frequency, E is the electric field vector, n(ω) and k(ω) are the spectral-dependent real and imaginary parts of the refractive index $\tilde{n} = n + ik$ over volume V. The integral was calculated.[17] Wavelength λ is within the range of 400 nm to 800 nm. Because of the polarity of dimers model, we divided nature light into two components as p- and s-polarization, which parallel and perpendicular to the two spheres plane respectively. And then, we depicted the calculated integrated solar absorption by the following equation.

$$\int A_P = \int_{400}^{800} 1/2 \{A_{p_s}(\lambda) + A_{p_p}(\lambda)\} \cdot AM1.5D(\lambda) d\lambda \quad (7)$$

where $A_{p_s}(\lambda)$ and $A_{p_p}(\lambda)$ are the corresponding calculated absorption, AM1.5D is the standard direct solar spectrum. In addition, noncoupling-NPs is nonpolar model, $A_{p_s}(\lambda) = A_{p_p}(\lambda) = A_P(\lambda)$. To exactly indicate the capability of absorption, $\int A_P$ is normalized by $\int A_{MAX}$, where A_{MAX} is the maximum achievable absorption of 100% in the range of wavelength (400-800 nm), which is considered to be the infinite thickness of absorber layer. It must be noticed that, because of the highly dispersive material of perovskite and the long x,y dimensions of the unit cell, the influence between unit cells is very week. Therefore, these calculations are not limited to period NPs and they are also suitable for random NPs with certain concentration.

The open source software package MIT Electromagnetic Equation Propagation 3D (MEEP) was used to realize Finite-difference time-domain (FDTD) simulations.[26] The parameters of silver, gold,[27] and perovskite for Lorentz model in this software are illustrated in **Table 1-3**. Soft gauss source with multiple frequencies with small step was introduced to obtain continuous curve of absorption as a function of wavelength. After that, calculation results were dealt with fast Fourier transform (FFT) to extract single frequency and normalized to the incident light. Compared to the reported calculation method with only serval single frequencies, this method gives more reality and is convenient.

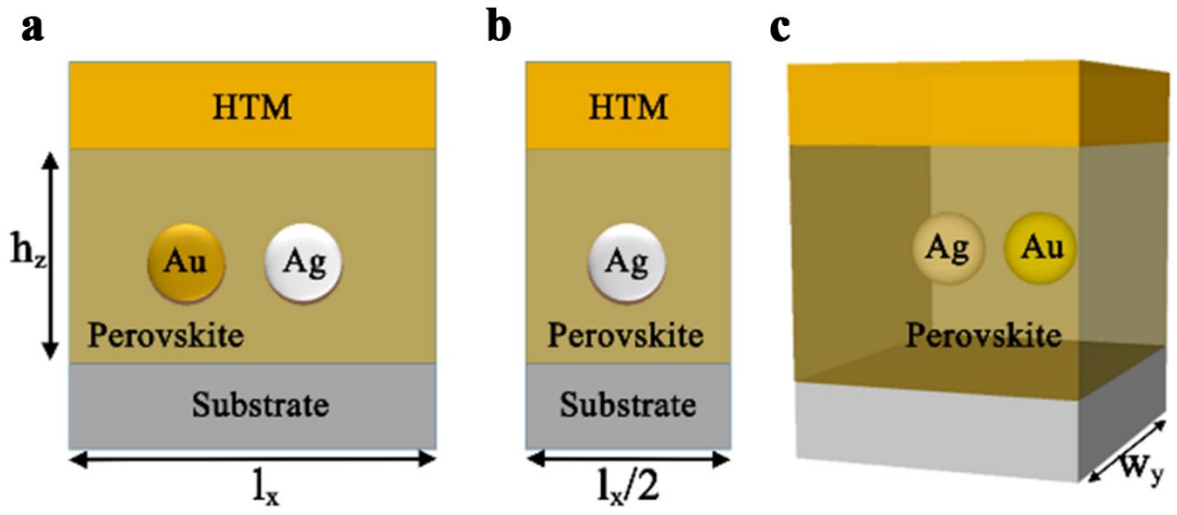

Figure 2. Modeled perovskite unit cell (a) dimers and (b) noncoupling-NPs. (c) 3D view of dimer unit cell.[25]

4.3 Results and discussion

Plasmonic perovskite photovoltaics have the enhanced optical performance of devices, which is attributed to the utilized surface plasmon of the embedded NPs excited by the incoming visible light. The initial report demonstrated that the enhanced near field induced by the plasmon of noncoupling NPs inside films contributes to the enhanced light absorption of perovskite, which is the called radiation effect. For dimers, plasmon will be coupled and form two enhanced optical field areas called junction area and ends area (no-junction area near the surface of NPs). According to plasmon hybridization theory, the inter-coupling of dimers can be viewed as the interaction of each plasmon mode of NP (ψ). There are two-phases called in-phase mode ($\psi_A + \psi_B$) and out-of-phase mode ($\psi_A - \psi_B$). Under longitudinal polarization (the p-component of nature light which is parallel to the dimer), plasmon modes σ ($\psi_A + \psi_B$) and $\sigma^*(\psi_A - \psi_B)$ contribute to the mainly enhanced optical field in junction and ends area respectively. The inter-coupling (π and π^*) under transverse polarization is very weak.[21, 28]. **Figure 3a** shows that, the σ^* hybridization mode of homo-dimers, which is supposed to form enhanced optical field in ends area is vanished because of cancelation of out-of-phase equation ($\psi_A - \psi_B$), where $\psi_A = \psi_B = \psi_{Au}/\psi_{Ag}$ condition is expected. Homo-dimers including gold homo-dimer and silver homo-dimer cannot

establish strong enhanced optical field in nonjunction area near the surface of NPs. Likewise, π mode is absent under transverse polarization. As shown in **Figure 3b,** hetero-dimer have both plasmon modes in ends area and junction area because $\psi_{Au} \neq \psi_{Ag}$.

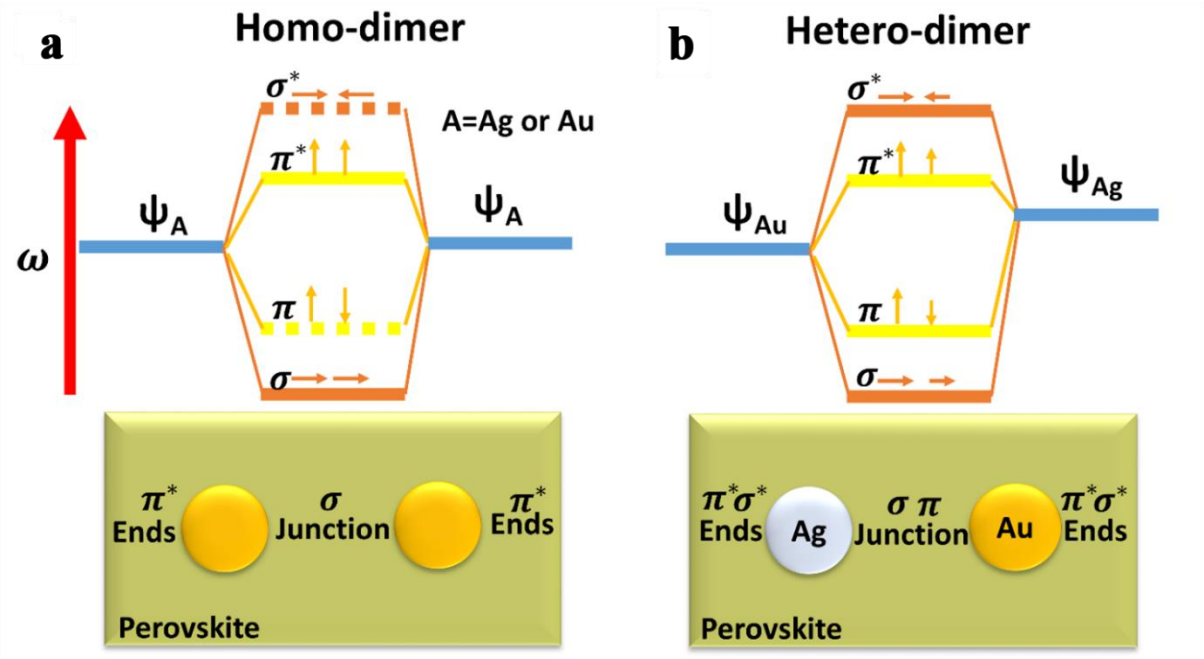

Figure 3. Plasmon hybridization of homo-dimers and silver-gold hetero-dimer (Dash lines represent the vanished coupling mode).[25]

These results also match with the absent of σ^* and π in the scattering cross section spectra (**Figure 4)** of homo-dimers evaluated by dipolar-dipolar coupling. According to the above factors, the antisymmetric silver (ψ_{ag})-gold (ψ_{au}) hetero-dimers (**Figure 3b**), which provide enhanced optical field in both junction and ends area, show the significant advantage over the homo-dimers. **Figure 4** also gives the frequency of the localized surface plasmon resonance of homo-dimers and hetero-dimer. The plasmon resonance wavelength of Ag-Au hetero-dimer is around 750 nm.

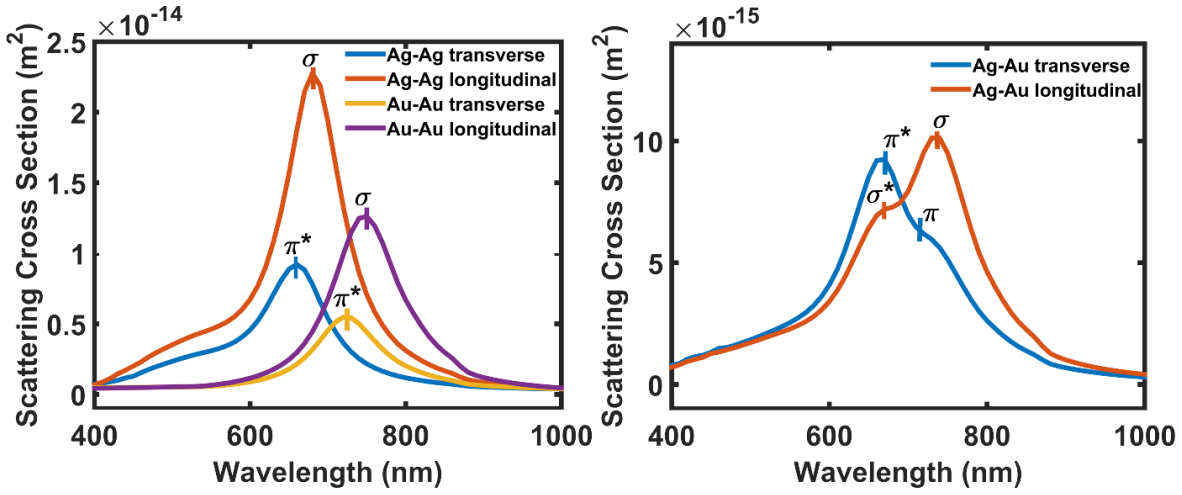

Figure 4. Scattering cross section spectrum of homo-dimers and hetero-dimer (size: 60 nm diameter, gap: 15 nm) simulated by DDA method.[25]

We calculated and compared the light absorption of perovskite film with the embedded homo-dimers and hetero-dimer by using FDTD simulation to precisely evaluate the effect of inter-particle coupling on the light absorption of the surrounding perovskite. Meanwhile, two kinds of non-coupling NPs (Ag, Au) with same volume concentration are analyzed. **Figure 5a** shows the absorption of perovskite as a function of thickness (150-350 nm), in which the results for thickness >300 nm closely match with the reported results.[17]

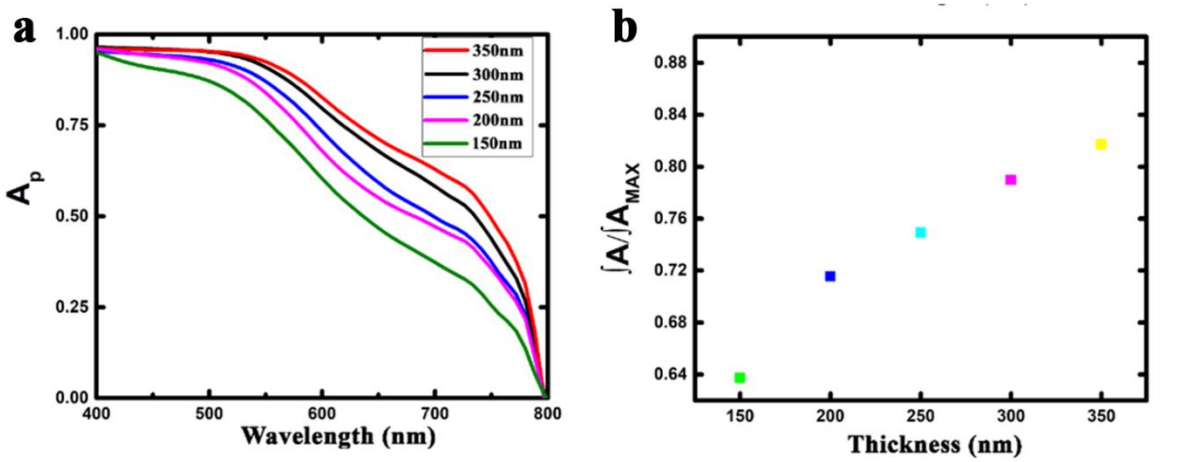

Figure 5. (a) Absorption of perovskite. (b) Normalized absorption $\int A_P / \int A_{MAX}$ of perovskite depends on thickness.[25]

As shown in **Figure 5b**, thin thickness usually leads to the decrease of light-harvesting properties of perovskite film. Precisely, the decrease in absorption for thickness from 200 nm to 150 nm is four times larger than that from 250 nm to 200 nm. A 150 nm film only absorbs 63.7 % of the total light. Moreover, the relatively low absorption lies at long wavelength >650 nm. Therefore, it is a challenge to fabricate thin perovskite devices without impacting the performance. We selected 150 nm perovskite as the reference film to outline whether or not the incorporating hetero-dimer can actually enhance the absorption of the thin perovskite layer.

We evaluate the absorption of the PVK with same size of NPs (diameter: 50 nm) in all cases for the sake of comparison. **Figure 6a** gives the relationship between Ap (light absorption) and wavelength. Perovskite with hetero-dimer (diameter: 50 nm, gap distance: 10 nm) induced enhanced light-harvesting properties compared to noncoupling Ag or Au NPs. In addition, this enhancement was especially localized in the range of $650\ \text{nm} < \lambda < 800\ \text{nm}$, where light absorption of PVK was low.[29] **Figure 6b** demonstrates that the absorption of PVK with Ag-Au is obvious higher than that of Ag-Ag and Au-Au, among which Ag-Au hetero-dimer yields the best performance.

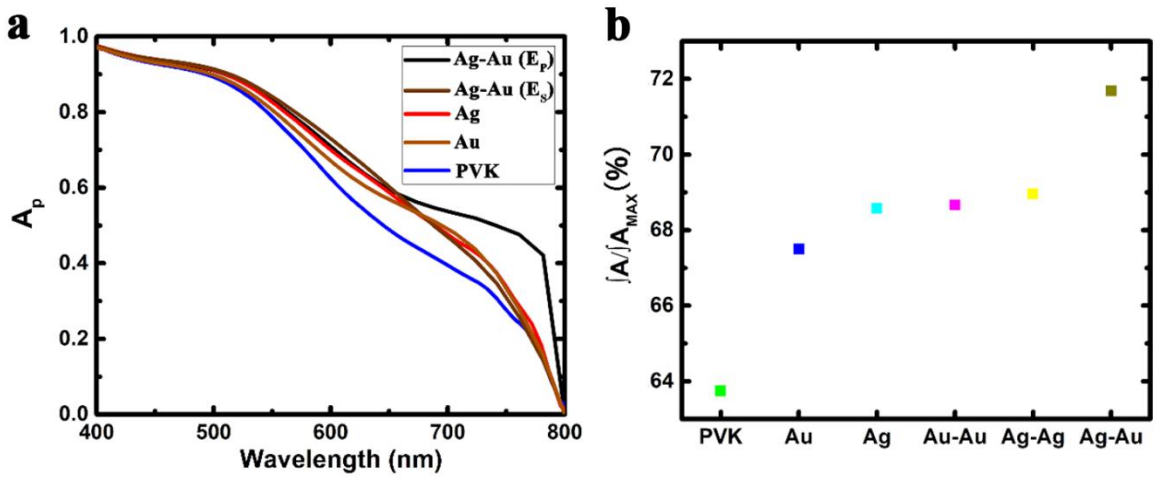

Figure 6. (a) Absorption spectra of PVK with NPs and (b) The relationship between normalized absorption $\int A_P / \int A_{MAX}$ of PVK with NPs. Perovskite thickness: 150 nm, nanoparticle diameter: 50 nm, gap distance: 10 nm.[25]

The squared amplitude of the electric field $|E|^2/|E_0|^2$ are analyzed in all cases at $\lambda = 750$ nm, which is around the plasmon resonance frequency inside the junction area of hetero-dimer. **Figure 7a-7b** shows the optical field inside perovskite descends along the

central of NPs like radiation. This special optical field distribution attributing to the absorption enhancement of perovskite is the reported radiation effect.[17] **Figure 7d-7f** shows the electric field of perovskite with dimers. Besides radiation effect, the enhanced optical field in the junction area induces the more important inter-coupling effect under longitudinal polarization.

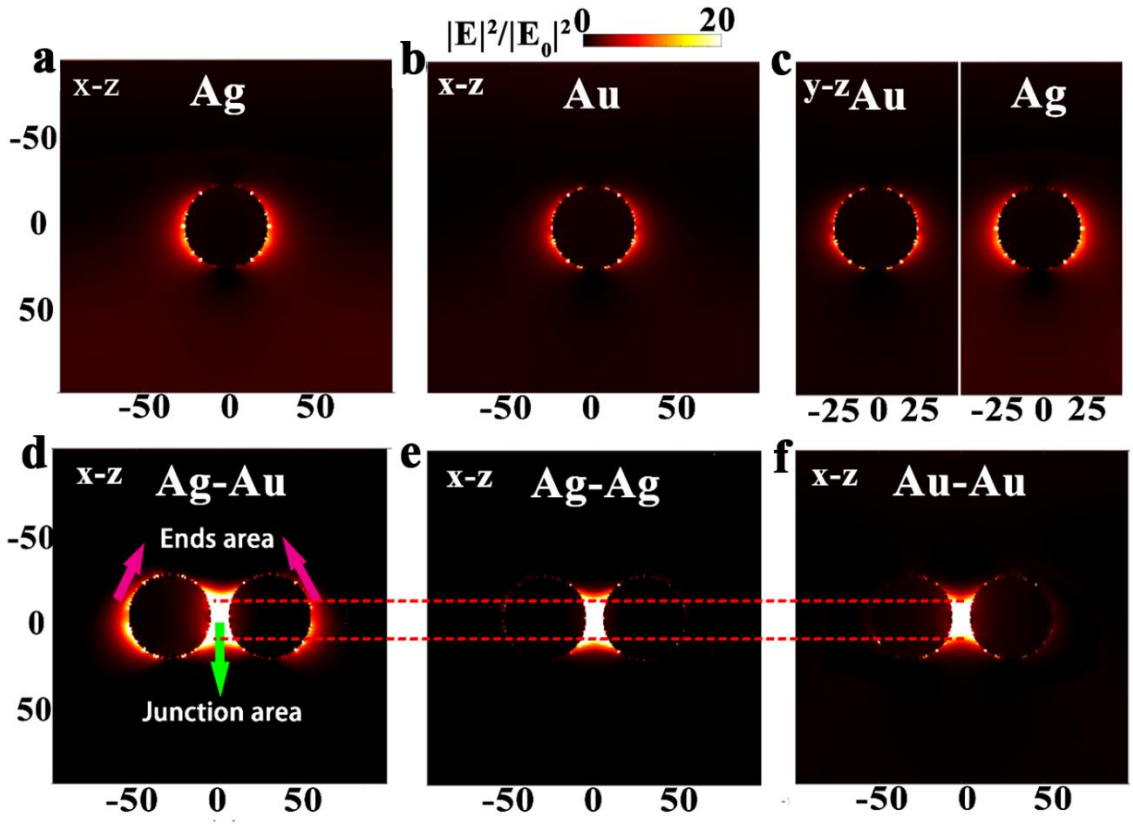

Figure 7. Spatial distribution of the normalized electric field intensity (wavelength: $\lambda =$ 750 nm) in perovskite (150 nm thickness) with (a) Ag, (b) Au, (c) Ag-Au, (d) Ag-Au, (e) Ag-Ag and (f) Au-Au. (c) is electric filed in the y-z planes under E_s and (d)-(f) are electric field in the x-z planes under E_p. All NPs are 50 nm diameter. Dimer gap distance is 10 nm.[25]

Hetero-dimer (**Figure 7d)** under longitudinal polarization induces relatively large total junction area than gold/silver homo-dimer (**Figure 7e-7f**). **Figure 8** shows the relationship between intensity and wavelength for PVK with dimer NPs. Among them, Ag-Au end position gave the best results.

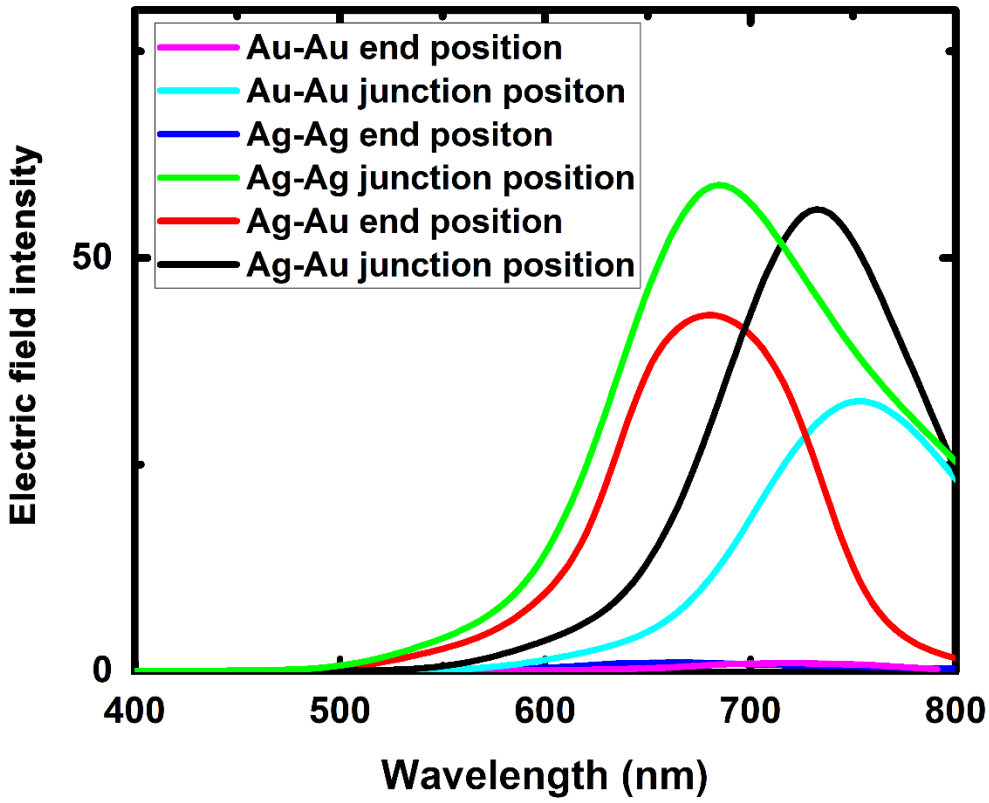

Figure 8. The relationship between electric field intensity and wavelength. Diameter: 60 nm, gap distance: 15 nm.[25]

Figure 9 shows the normalized electric field intensity of perovskite with homo-dimers and hetero-dimer under Ey and Ez. Inter-coupling of dimer under vertical polarization behaves similar to that of individual NPs. Intensity of electric field near silver and gold NP surface in hetero-dimer is slightly stronger than that of Ag-Ag and Au-Au respectively, which are beneficial for light-harvesting.

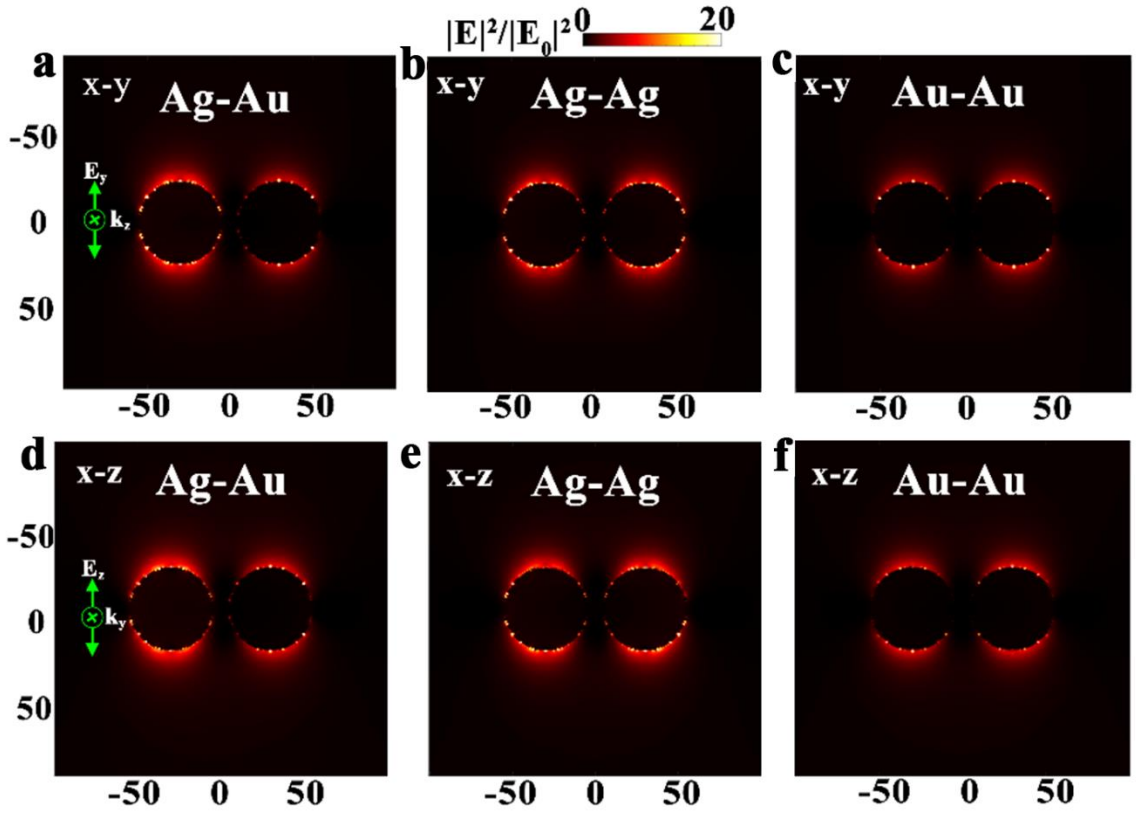

Figure 9. Normalized electric field intensity of perovskite with homo-dimers and hetero-dimer (a-c) at x-y plane under Ey and (d-f) x-z plane under Ez. Dimer diameter : 50 nm, gap distance: 10 nm.[25]

We have tuned the size of NPs and the gap distance (**Figure 10a)** to obtain the maximum absorption of perovskite with hetero-dimer. The maximum enhancement was obtained by 80 nm diameter hereo-dimer with 25 nm gap distance. The normalized absorption was 81.68 %. The value was 28.15 % higher than that of perovskite (150nm thickness) and equals to the absorption of perovskite film with about 350 nm thickness. **Figure 10a** also shows that every size hetero-dimer has an optimization gap distance. For example, absorption of PVK with 80 nm Ag-Au dimer was highest when the gap distance was 30 nm. **Figure 10b** shows that, the absorption of perovskite under p-polarization of incident light induces higher absorption compared to that under s-polarization. This would be explained the difference of the polarity and asymmetric of dimers.

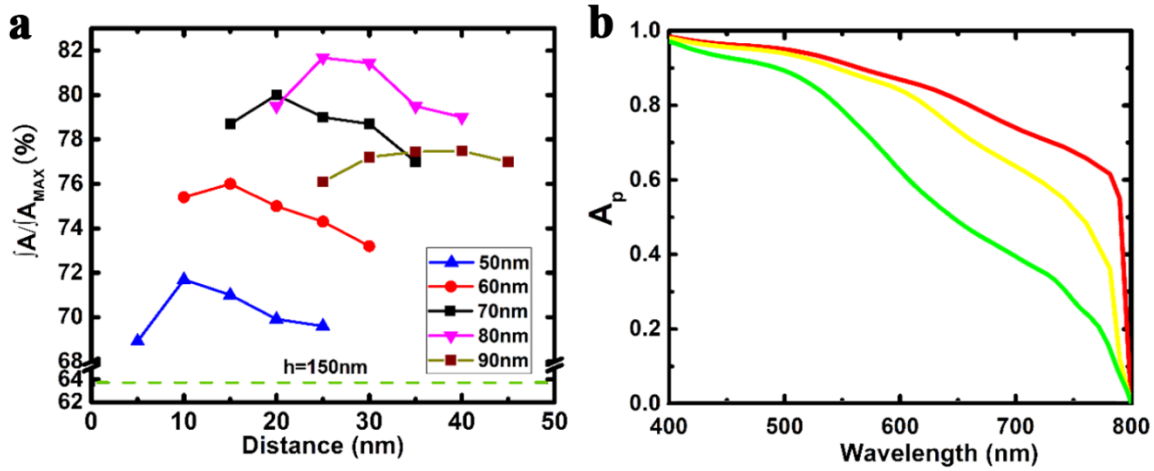

Figure 10. Normalized absorption of perovskite (150 nm thickness) with (a) hetero-dimer with various diameter and gap distance. (b) Absorption $A_{p_p}(\lambda)$ (yellow) and $A_{p_s}(\lambda)$ (red) of perovskite (150 nm thickness) with hetero-dimer (diameter: 80 nm, gap distance: 25 nm) and reference film (green).[25]

Figure 11 shows the normalized absorption of NPs of hetero-dimers. The absorption of NPs was low. For example, NP with 50 nm size with 10nm gap distance has only 0.15 % absorption. All of the absorption was lower than 1 %. The volume concentration of the filled NPs in perovskite is within the range 1.4 %-8.14 %.

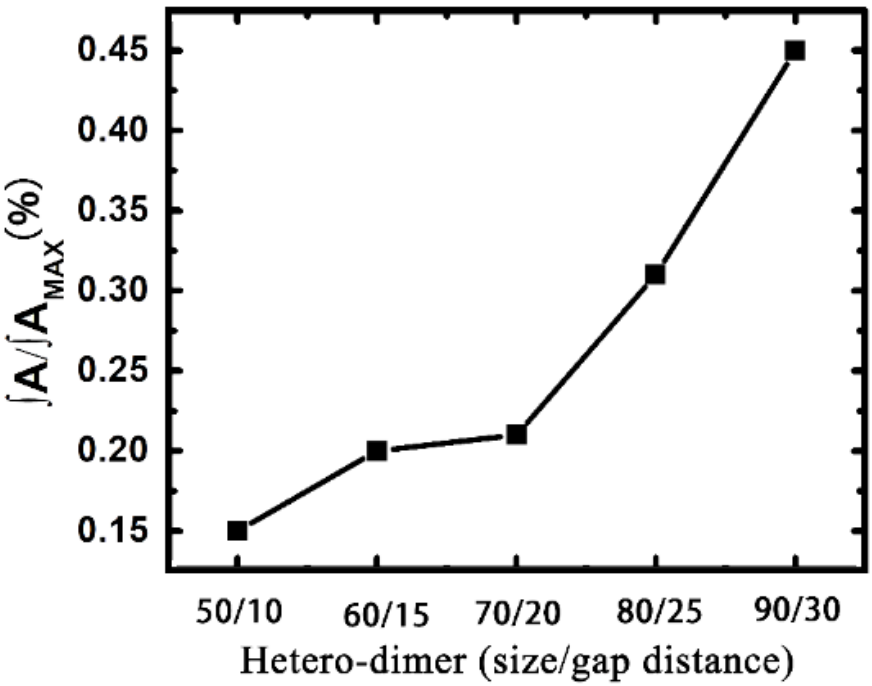

Figure 11. Normalized absorption of NPs embedded in perovskite with 150 nm thickness.[25]

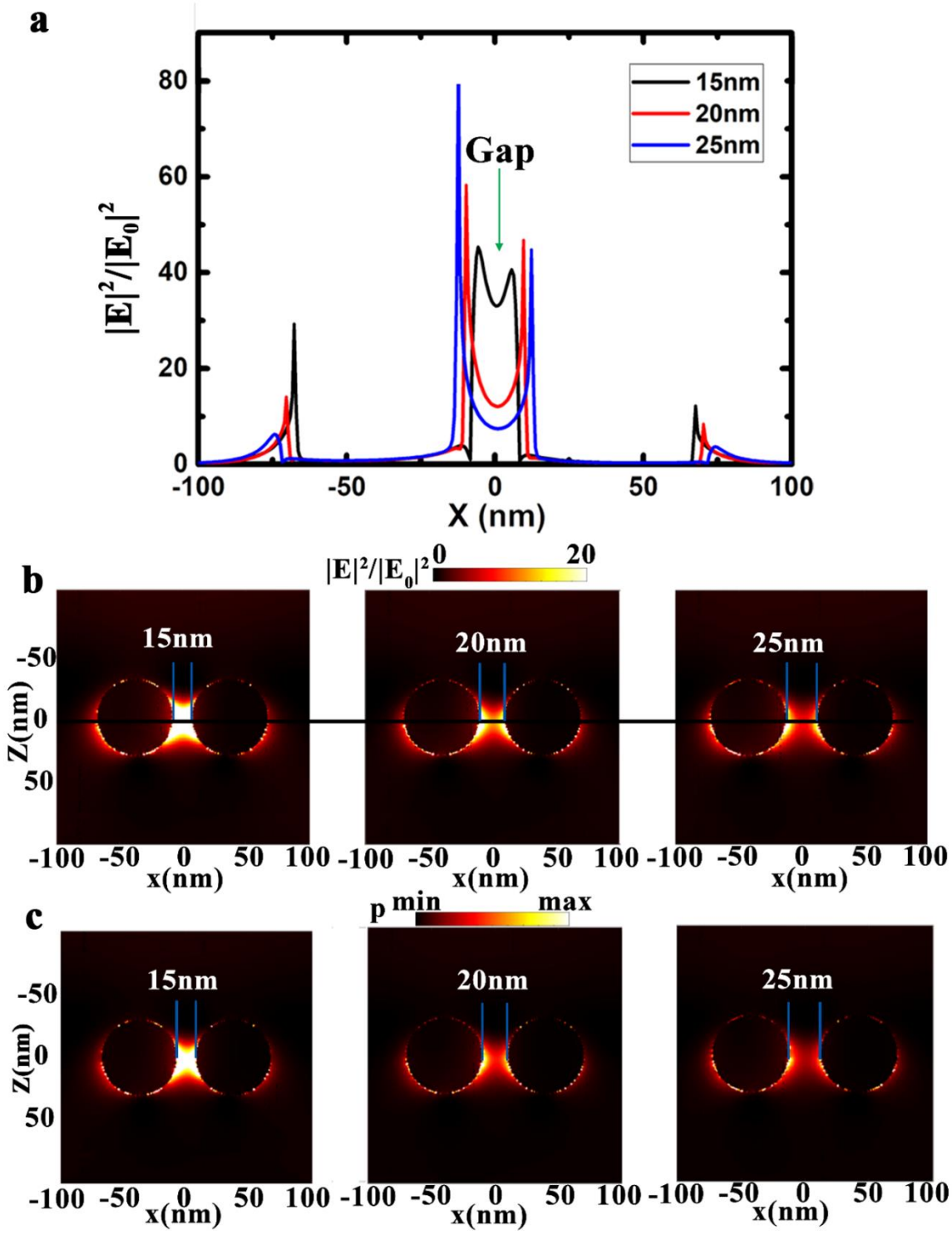

Figure 12. (a) The relationship between normalized electric field intensity with x axis. (b) Spatial distribution of the normalized electric field intensity and (c) normalized power absorption per unit volume of perovskite (150 nm thickness) with hetero-dimer (60 nm diameter) with gap distance from 15 nm to 25 nm (wavelength: $\lambda = 750$ nm).[25]

Figure 10 shows the relationship between $|E|^2/|E_0|^2$ and gap distance from the center of the dimer. The gap distance becomes wider than 20 nm, the value decrease in the gap regions. 15 nm gap distance is best for 60 nm diameter hetero-dimer. **Figure 12** shows that the field intensity actually sharply reduce from 33.1 to 7.4 when gap distance is increased from 15 nm to 25 nm. The capability of light-harvesting is very sensitive to gap distance and the junction area.[29, 30]

As shown in **Figure 13a-13b and 13d-13e,** hetero-dimer with larger particle size (<90 nm) establishs obvious larger junction area and ends area. Antibonding mode in ends area supports a large radiation effect. Bonding mode localized in junction area favors a very strong and large enhanced optical field, leading to the significant inter-coupling effect.

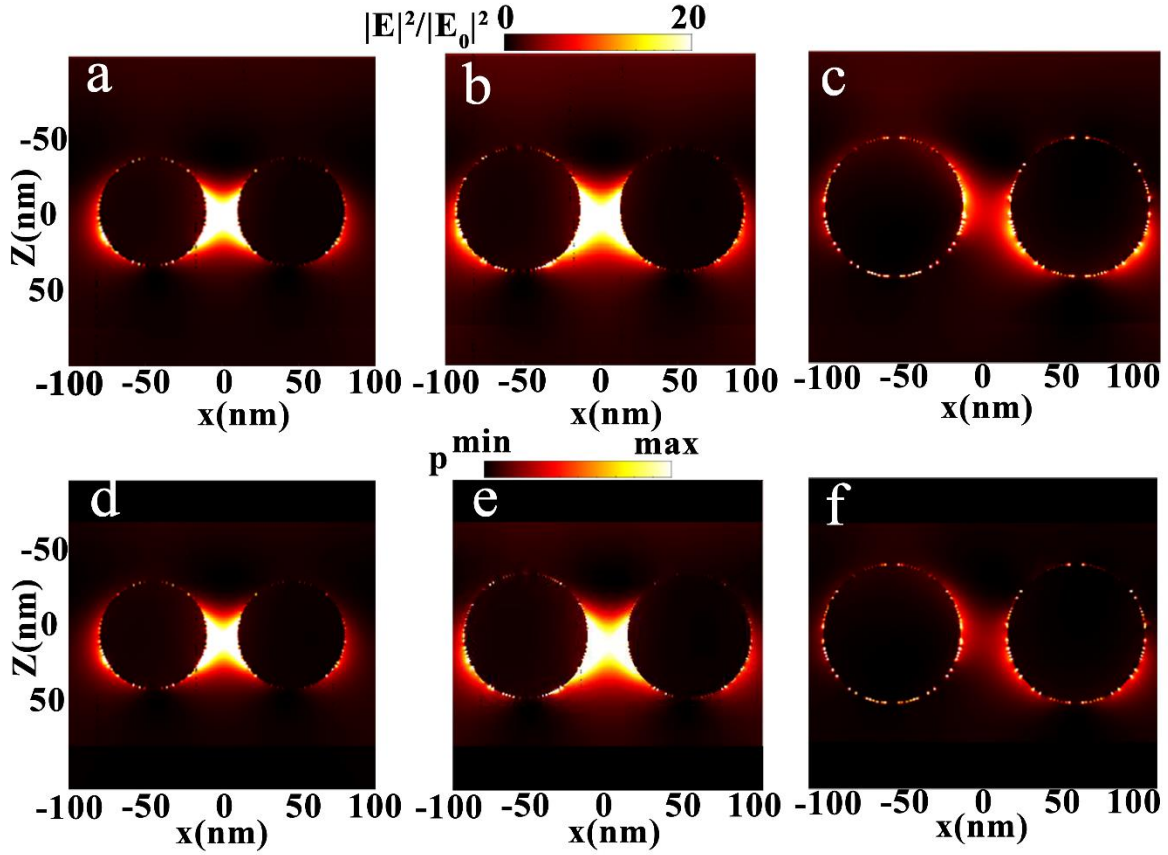

Figure 13. Normalized spatial distribution of electric field intensity of perovskite (150 nm thickness) with hetero-dimer (size/gap distance) (a) 70 nm/20 nm, (b) 80 nm/25 nm and (c) 90 nm/30 nm. Normalized power absorption per unit volume for hetero-dimer (d) 70 nm/20 nm, (e) 80 nm/25 nm and (f) 90 nm/30 nm (wavelength: $\lambda = 750$ nm).[25]

As shown in **Figure 13c and 13f,** for hetero-dimer with too large size (diameter: 90nm), the junction area is vanished and becomes less sensitive to gap distance.[31]

The relationship between performance and incident angle was analyzed. In order to simulate the absorption as the function of angle, (**Figure 14**) the following unit cell was added, where the angle of x-y dimension is 90^0. This maintains the same volume and FF as the normal incident situation.

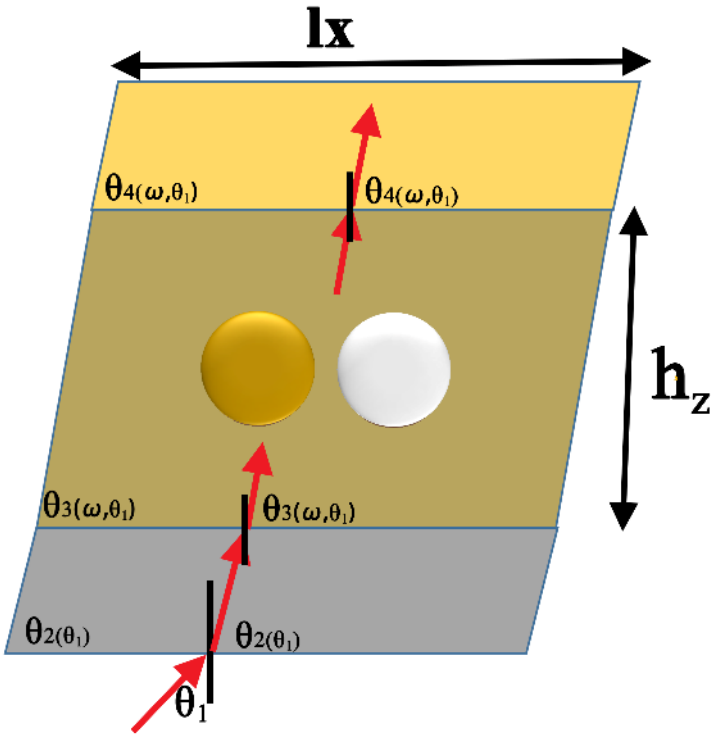

Figure 14. The unit cell for simulating absorption as the function of incident angle.[25]

To make the model along the main direction of incident light, θ_3 was taken as a function of incident angle θ_1 and frequency of incident light. This is because the refractive index of perovskite depends on frequency.

According to the influence of absorption as a function of the incident angle. As shown in **Figure 15a**, the $\int A / \int A_{MAX}$ decrease sharply after the incident angle became larger than 50^0, which is consistent with the reported result.[33] The incorporating of hetero-dimer in perovskite film enables a wider serviceable angle than the reference film. It will be very beneficial for the industrial applications.

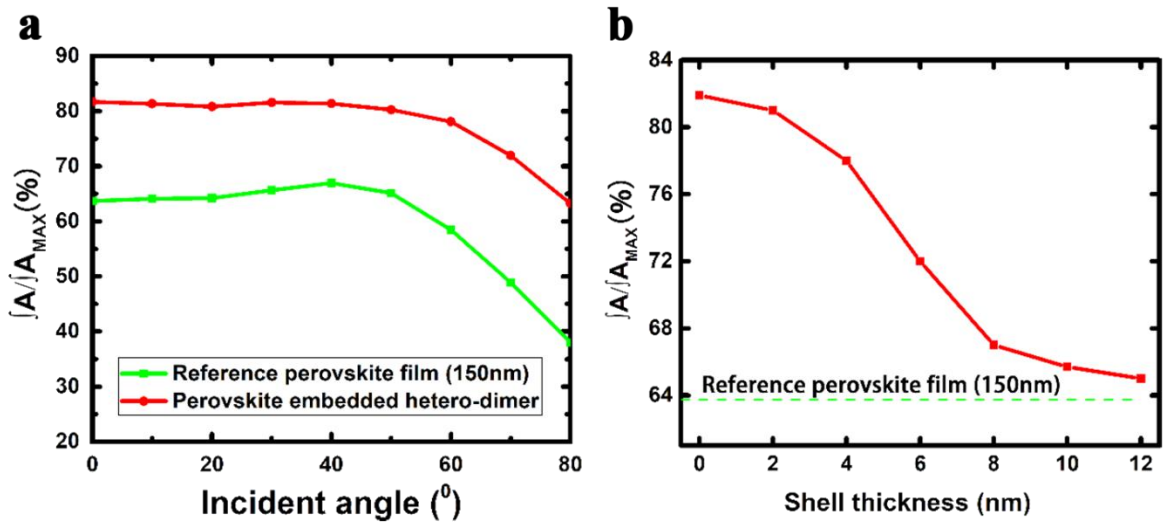

Figure 15. (a) The relationship between $\int A / \int A_{MAX}$ and incident angle. (b) The relationship between $\int A / \int A_{MAX}$ and shell thickness. Perovskite (150 nm thickness) with hetero-dimer (diameter: 80 nm, gap distance: 25 nm) (red) and reference film (green).[25]

Due to exciton quenching induced by the direct integration of metal NPs into the active layer, surface passivation of the metal NPs is required by shielding metal particles with dielectric coatings.[34] In order to overcome these challenges associated with plasmonic metal NPs, a series of thickness of uniform SiO_2 shell coated on dimers were examined. As shown in **Figure 15b,** the normalized absorption decreased with the thickness of coated shell and rapidly approached the performance of the reference perovskite film without NPs. Therefore, thin silica shell is suggested. Taking 80 nm size hetero dimer as example, 4 nm thickness silica on each nanosphere of dimer can preserve 95 % of the performance.

Although the optimize size and distance of hetero-dimer seems difficult to realize, the recent colloidal conjugation technology open up new opportunities for a possible low-cost and easy preparation method. Metal dimers can be synthesized by colloidal approach in buffer solution, in which gap distance can be tuned by changing the length of conjugated molecular (ss-DNA),[21] and silica shell can be introduced by adding a silane coupling agent (e.g. 3-aminopropyltrimethoxysilane, APS).[32] Then random hetero-dimer with silica shell may can be dispersed on substrate and the gap may be filled with perovskite by spin-coating.

4.4 Conclusions

In conclusion, we confirm that interparticle coupling of hetero-dimer play an important role in the enhancement of absorption of perovskite by a series of theoretical modeling and calculations including plasmon hybridization, DDA and FDTD. Perovskite with hetero-dimer processes higher light absorption than that of homo-dimers, because of the both radiation effect in the ends area and the strongly enhanced optical field localized in junction area.

In addition, compared to noncoupling NPs with the same concentration, all dimers lead to higher enhancement on optical absorption of perovskite especially within the range of 650-800 nm, which demonstrates that the strong coupling of LSPR in the gap of the embedded dimer plays an important role on the light-harvesting of perovskite.

The more interesting thing is that the relatively larger total area of overlap optical field inside the gap of hetero-dimer than homo-dimer enhanced the absorption of perovskite. For the sake of finding the optimization dimer, gap distance and size of NP of hetero-dimer were tuned. The result shows that proper distance of hetero-dimer is needed, because short distance reduce the area of overlap area. Too long distance will separate the LSPR of each NP. In addition, this distance increases with the size of NP of the dimer.

Our results suggest that the maximum absorption of perovskite film with 150 nm thickness may be produced by embedding 80 nm diameter silver-gold hetero-dimer with 25 nm gap distance. About 28.15 % improvement of light-harvesting of perovskite with hetero-dimer compared to the reference film were obtained, which was higher than 10 % of homo-dimers reported previously. In addition, thin silica shell of dimer is suggested, because of the confinement effect.

Our work provides a significant meaning to further optimize the optical property of devices and also reduce the amount of absorbing material. Although, all these examples herein chosen was $MAPbI_3$, obvious absorption-enhancing effects should be expected for other absorber based photovoltaics.

References

1. Heidarzadeh, H.; Rostami, A.; Dolatyari, M.; Rostami, G., Plasmon-enhanced performance of an ultrathin silicon solar cell using metal-semiconductor core-shell hemispherical nanoparticles and metallic back grating. *Appl Opt* **2016,** 55, (7), 1779-85.

2. Tsai, F. J.; Wang, J. Y.; Huang, J. J.; Kiang, Y. W.; Yang, C. C., Absorption enhancement of an amorphous Si solar cell through surface plasmon-induced scattering with metal nanoparticles. *Opt Express* **2010,** 18 Suppl 2, A207-20.

3. Zhou, Z. Q.; Wang, L. X.; Shi, W.; Sun, S. L.; Lu, M., A synergetic application of surface plasmon and field effect to improve Si solar cell performance. *Nanotechnology* **2016,** 27, (14), 145203.

4. Tripathi, B.; Yadav, P.; Kumar, M.; Mukhopadhyay, I., Plasmon enhanced light trapping to improve efficiency of dye-sensitized solar cell. *J Nanosci Nanotechnol* **2014,** 14, (3), 2624-9.

5. Yen, Y. C.; Chen, P. H.; Chen, J. Z.; Chen, J. A.; Lin, K. J., Plasmon-induced efficiency enhancement on dye-sensitized solar cell by a 3D TNW-AuNP layer. *ACS Appl Mater Interfaces* **2015,** 7, (3), 1892-8.

6. Dang, X.; Qi, J.; Klug, M. T.; Chen, P.-Y.; Yun, D. S.; Fang, N. X.; Hammond, P. T.; Belcher, A. M., Tunable localized surface plasmon-enabled broadband light-harvesting enhancement for high-efficiency panchromatic dye-sensitized solar cells. *Nano letters* **2013,** 13, (2), 637-642.

7. Uddin, A.; Yang, X., Surface plasmon enhanced organic solar cell with different silver nanosphere sizes. *J Nanosci Nanotechnol* **2014,** 14, (8), 5752-60.

8. Baek, S.-W.; Park, G.; Noh, J.; Cho, C.; Lee, C.-H.; Seo, M.-K.; Song, H.; Lee, J.-Y., Au@ Ag core–shell nanocubes for efficient plasmonic light scattering effect in low bandgap organic solar cells. *ACS nano* **2014,** 8, (4), 3302-3312.

9. Mali, S. S.; Shim, C. S.; Kim, H.; Patil, P. S.; Hong, C. K., In situ processed gold nanoparticle-embedded TiO 2 nanofibers enabling plasmonic perovskite solar cells to exceed 14% conversion efficiency. *Nanoscale* **2016,** 8, (5), 2664-2677.

10. Omelyanovich, M.; Makarov, S.; Milichko, V.; Simovski, C., Enhancement of perovskite solar cells by plasmonic nanoparticles. *arXiv preprint arXiv:1601.06778* **2016**.

11. Zhang, C.; Luo, Q.; Shi, J.; Yue, L.; Wang, Z.; Chen, X.; Huang, S., Efficient perovskite solar cells by combination use of Au nanoparticles and insulating metal oxide. *Nanoscale* **2017,** 9, (8), 2852-2864.

12. Anaya, M.; Lozano, G.; Calvo, M. E.; Zhang, W.; Johnston, M. B.; Snaith, H. J.; Míguez, H., Optical Description of Mesostructured Organic–Inorganic Halide Perovskite Solar Cells. *The Journal of Physical Chemistry Letters* **2015,** 6, (1), 48-53.
13. Lin, Q.; Armin, A.; Nagiri, R. C. R.; Burn, P. L.; Meredith, P., Electro-optics of perovskite solar cells. *Nat Photon* **2015,** 9, (2), 106-112.
14. Ha, S.-T.; Shen, C.; Zhang, J.; Xiong, Q., Laser cooling of organic–inorganic lead halide perovskites. *Nature Photonics* **2016,** 10, (2), 115-121.
15. Grancini, G.; Roldán-Carmona, C.; Zimmermann, I.; Mosconi, E.; Lee, X.; Martineau, D.; Narbey, S.; Oswald, F.; De Angelis, F.; Graetzel, M., One-Year stable perovskite solar cells by 2D/3D interface engineering. *Nature Communications* **2017,** 8.
16. Younts, R.; Duan, H. S.; Gautam, B.; Saparov, B.; Liu, J.; Mongin, C.; Castellano, F. N.; Mitzi, D. B.; Gundogdu, K., Efficient Generation of Long‐Lived Triplet Excitons in 2D Hybrid Perovskite. *Advanced Materials* **2017,** 29, (9).
17. Carretero-Palacios, S.; Jiménez-Solano, A.; Míguez, H., Plasmonic Nanoparticles as Light-Harvesting Enhancers in Perovskite Solar Cells: A User's Guide. *ACS Energy Letters* **2016,** 1, (1), 323-331.
18. Seo, E.; Ko, S.-J.; Min, S. H.; Kim, J. Y.; Kim, B.-S., Plasmonic transition via interparticle coupling of Au@ Ag core–shell nanostructures sheathed in double hydrophilic block copolymer for high-performance polymer solar cell. *Chemistry of Materials* **2015,** 27, (13), 4789-4798.
19. Hu, Z.; Liu, Z.; Li, L.; Quan, B.; Li, Y.; Li, J.; Gu, C., Plasmonic Coupling: Wafer‐Scale Double‐Layer Stacked Au/Al2O3@ Au Nanosphere Structure with Tunable Nanospacing for Surface‐Enhanced Raman Scattering (Small 19/2014). *Small* **2014,** 10, (19), 3932-3932.
20. Carretero-Palacios, S.; Calvo, M. E.; Míguez, H., Absorption Enhancement in Organic–Inorganic Halide Perovskite Films with Embedded Plasmonic Gold Nanoparticles. *The Journal of Physical Chemistry C* **2015,** 119, (32), 18635-18640.
21. Sheikholeslami, S.; Jun, Y.-w.; Jain, P. K.; Alivisatos, A. P., Coupling of Optical Resonances in a Compositionally Asymmetric Plasmonic Nanoparticle Dimer. *Nano Letters* **2010,** 10, (7), 2655-2660.
22. Mandal, P.; Sharma, S., Progress in plasmonic solar cell efficiency improvement: A status review. *Renewable and Sustainable Energy Reviews* **2016,** 65, 537-552.
23. De Wolf, S.; Holovsky, J.; Moon, S.-J.; Löper, P.; Niesen, B.; Ledinsky, M.; Haug, F.-J.; Yum, J.-H.; Ballif, C., Organometallic halide perovskites: sharp optical absorption edge and

its relation to photovoltaic performance. *The Journal of Physical Chemistry Letters* **2014,** 5, (6), 1035-1039.

24. Anaya, M.; Lozano, G.; Calvo, M. E.; Zhang, W.; Johnston, M. B.; Snaith, H. J.; Míguez, H., Optical description of mesostructured organic–inorganic halide perovskite solar cells. *The journal of physical chemistry letters* **2014,** 6, (1), 48-53.

25. Hu, Z.; Ma, T.; Hayase, S., Interparticle coupling effect of silver-gold heterodimer to enhance light harvesting in ultrathin perovskite solar cell, *Journal of Photonics for Energy* **2018,** 8, (1), 015502.

26. Oskooi, A. F.; Roundy, D.; Ibanescu, M.; Bermel, P.; Joannopoulos, J. D.; Johnson, S. G., MEEP: A flexible free-software package for electromagnetic simulations by the FDTD method. *Computer Physics Communications* **2010,** 181, (3), 687-702.

27. Rakić, A. D.; Djurišić, A. B.; Elazar, J. M.; Majewski, M. L., Optical properties of metallic films for vertical-cavity optoelectronic devices. *Applied Optics* **1998,** 37, (22), 5271-5283.

28. Prodan, E.; Radloff, C.; Halas, N. J.; Nordlander, P., A hybridization model for the plasmon response of complex nanostructures. *science* **2003,** 302, (5644), 419-422.

29. Gunnarsson, L.; Rindzevicius, T.; Prikulis, J.; Kasemo, B.; Käll, M.; Zou, S.; Schatz, G. C., Confined Plasmons in Nanofabricated Single Silver Particle Pairs: Experimental Observations of Strong Interparticle Interactions. *The Journal of Physical Chemistry B* **2005,** 109, (3), 1079-1087.

30. Jain, P. K.; Huang, W.; El-Sayed, M. A., On the Universal Scaling Behavior of the Distance Decay of Plasmon Coupling in Metal Nanoparticle Pairs: A Plasmon Ruler Equation. *Nano Letters* **2007,** 7, (7), 2080-2088.

31. Ben, X.; Park, H. S., Size Dependence of the Plasmon Ruler Equation for Two-Dimensional Metal Nanosphere Arrays. *The Journal of Physical Chemistry C* **2011,** 115, (32), 15915-15926.

32. Ung, T.; Liz-Marzán, L. M.; Mulvaney, P., Controlled method for silica coating of silver colloids. Influence of coating on the rate of chemical reactions. *Langmuir* **1998,** 14, (14), 3740-3748.

33. Wang, D.-L.; Cui, H.-J.; Hou, G.-J.; Zhu, Z.-G.; Yan, Q.-B.; Su, G., Highly efficient light management for perovskite solar cells. *Scientific reports* **2016,** 6, 18922.

34. Arinze, E. S.; Qiu, B.; Nyirjesy, G.; Thon, S. M., Plasmonic nanoparticle enhancement of solution-processed solar cells: practical limits and opportunities. *ACS Photonics* **2016,** 3, (2), 158-173.

5. Bismuth based nontoxic metal halide solar cell

The performance of solution-processed solar cells (SCs) has been greatly improved within past decade, especially $MAPbI_3$ SCs with high-performance.[1-5] However, the toxicity of lead limits their commercial application. A series of candidates are under intensive interest. For example, $MASnI_3$ SCs with about 8 % power conversion efficiency (PCE) has been reported.[6-9] But all materials and devices processing was usually conducted in a nitrogen-filled glovebox because of the instability of tin cation, which is prone to oxidation when they are exposed to air and moisture. Compared to the instability as well as toxicity concerns, bismuth based materials are the most promising light-harvesting materials to replace lead and tin.[10, 11] So far, incorporation of methylammonium (MA) and cesium in bismuth iodide complex have been synthesized.[12-15] Silver bismuth iodide including $AgBi_2I_7$ and $AgBiI_4$ have been reported.[16, 17] However Ag^+ ion is sensitive to light exposure. As the stable monovalent cation, we selected Cu^+. In this section, synthesis and photovoltaic performance of $CuBiI_4$ is reported.

5.1 Experiment section

5.1.1 Preparation of precursor solution

N,N-dimethylacetamide (DMA) with Hydroiodic acid (HI) was employed to dissolve the BiI_3 and CuI powder. First, CuI and BiI_3 were mixed with molar ration of 1:1 and 1 ml DMA was added to the mixture by stirring for 2 h at room temperature. The concentration of CuI and BiI_3 was varied from 0.4 M to 0.7 M. After that, HI acid (57 wt. % without stabilizer) was added dropwise with stirring (4 h). The amount of the added HI in molar is two times of that of BiI_3. The solution became clear and the color turned purple-black during the stirring.

5.1.2 Fabrication of devices

Figure 1 illustrated the fabrication of $CuBiI_4$ devices. F-doped tin oxide (FTO) substrates were cleaned in an ultrasonic bath by acetone, isopropyl alcohol and deionized water in turn for 30 min respectively. Then, they were dried with nitrogen gas and cleaned by plasma sequentially. Compact-TiO_2 with about 50 nm thickness was sprayed on the substrates under 300 ^{0}C.

After that, a mesoporous TiO_2 layer with thickness of about 250 nm (particle diameter: 18 nm) was spin-coated and annealed at 500 ^{0}C for 1.5 h. Then, the absorber layer was

deposed by one-step method, in which about 80ul solution was casted on the surface and spin-coated with 500 rpm for 5 s and 5 krpm for 30 s. Solvent vapour annealing method was carried out with TBP solvent at room temperature. As-prepared samples were put on the holder in a chamber and exposed to vapour of TBP. The distance between sample and the solvent and the amount of TDP were precisely tuned to co-crystallize $CuBiI_4$ crystals. The random holes inside the cap of the chamber for SVA can avoid the too much accumulation of TBP on the surface of samples. After being annealed in TBP for about 2-3 h, samples were taken out from the chamber and dried on a hot plate under 70 ^{0}C for 30min to completely remove the remaining solvent. Then, HTM layer was fabricated by spin-coating Spiro-MeOTAD solution. The solution was prepared by dissolving 72.3 mg of 2,2',7,7'-tetrakis-(N,N-di-p-methoxyphenyl-amine)-9,9'-spirobifluorene (spiro-MeOTAD, Merck), in 1ml of chlorobenzene, in which 80µl ethanol and 17.5 µl lithium bis(trifluoromethanesulfonyl)imide (Li-TFSI) solution (520 mg Li-TSFI in 1 ml acetonitrile (Sigma-Aldrich, 99.8 %)) were added.

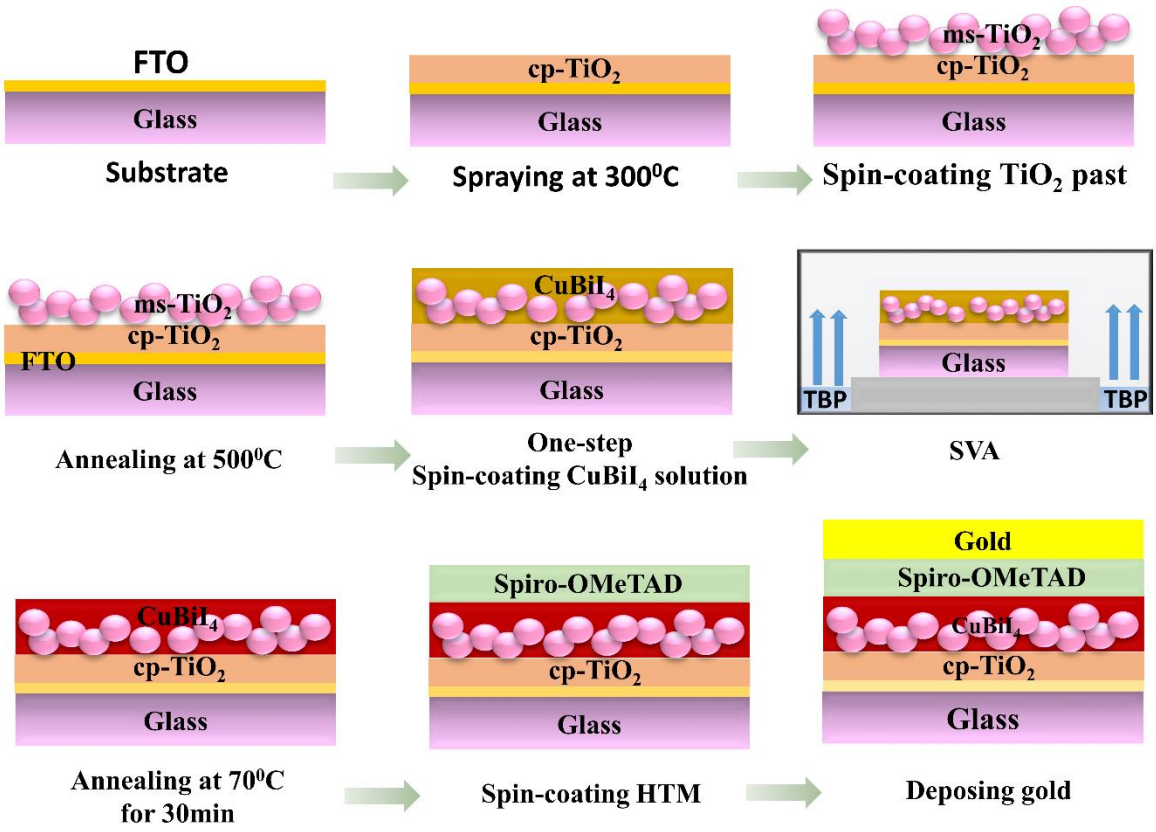

Figure 1. Schematic of fabrication process of $CuBiI_4$ solar cells.[33]

4-tert-butyl pyridine (TBP) was not used because it dissolved the $CuBiI_4$ layer. The added ethanol actually played the same role as TBP to dissolve Li-TSFI in chlorobenzene. Finally, about 100 nm gold electrode was deposited by thermal evaporator to complete the devices.

Characterization

Solar cell performances: The photovoltaic performance of cells were evaluated by using a solar simulator (CEP-2000SRR, Bunkoukeiki Inc., AM 1.5G 100 $mWcm^{-2}$) and a black mask on top of the devices with an exposure area 0.12 cm^2 during the photovoltaic measurements. The current-voltage (J-V) curves of these solar cells were measured with a 0.01 V/s scanning rate in reverse, forward and dark modes under standard global AM 1.5 illumination.

IPCE: The IPCE spectra were recorded by using CEP-2000SRR (Bunko Keiki) equipped with 300 W Xe lamp. Monochromatic light was exposed by DC mode and the current was taken every 100msec after the light exposure (10 nm interval).

XRD: X-ray Diffraction patterns were measured by X-ray diffraction analyses (SmartLab, Rigaku, Japan) with SmartLab(In-plane) goniometer were performed in the range 3°−80° with 0.0100 deg step width.

SEM: The surface morphology of the samples were observed through an S-5200 Ultra-High Resolution FE SEM (HITACHI).

FTIR: Attenuated Total Reflectance Fourier transform IR spectras (FT-IR) were tested by FT-IR spectrometer (JASCO, FT/IR-4100 Series) via an attenuated total reflectance (ATR) crystal.

Absorbance: Absorbance of films were measured by Electronic Absorption Spectroscopy (V-570, V550, JASCO, Japan).

PL: Photoluminescence lifetime were obtained from Compact NIR PL lifetime spectrometer (Hamamatsu, Japan).

PESA: The valence band level for $CuBiI_4$ film on a FTO-glass substrate (not device structure) were measured by using Photo-Electron Spectroscopy in Air (PESA) (AC3, RIKEN-KEIKI)

5.2 Results and discussion

Bismuth based devices, unlike lead or tin based solar cells, always suffered low coverage, poor morphology and pinholes in the resulting film.[18] Herein, we used concentrated HI acid assisted organic solvent to dissolve CuI and BiI_3. HI acid has been reported to dissolve BiI_3 or CuI to synthesize or make bulk crystals.[19] This is also used as the additive to improve the morphology in $MAPbI_3$ SCs[20]. To investigate whether the added concentrated HI acid (57 wt. %) in Dimethylacetamide (DMA) have influence on Fluorine-doped tin oxide (FTO) substrates, we measured the sheet resistance of FTO glasses after immerging the substrate in HI/DMA co-solvent with a series of HI concentrations (0-6 M) for 12h. **Figure 2a** illustrates that the conductivity of substrates were almost not affected even under high HI concentration (6 M). As shown in **Figure 2ai** (inserted photo)**,** HI acid assisted DMA completely dissolved CuI and BiI_3 powders with the exact molar ratio (HI: CuI: BiI_3=2: 1: 1). And high concentration of CuI/BiI_3 was obtained compared to other organic solvent includes DMF, Dimethyl sulfoxide (DMSO) and Tetrahydrofuran (THF) without HI. The HI produced complexes of hydrogen diiodocuprate(I) ($HCuI_2$) and hydrogen tetraiodobismuthanuide ($HBiI_4$) in DMA, which increase the solubility.

After that, solvent vapor annealing (SVA)[21, 22] using Tributyl phosphate (TBP) at room temperature was applied immediately to avoid low coverage and poor morphology.

During the SVA, TBP evaporates and its vapor will gradually penetrate the intermediate film and more importantly, simultaneously replace inside solvents because of their excellent miscibility, which benefits the co-crystallization of $CuBiI_4$. Additionally, high vapor pressure of TBP, enables the whole low-temperature film preparation. After SVA and following post-annealing at 70 ^{0}C for 30min to completely evaporate the remaining solvent, the color was obviously changed.

The FTIR spectrum of as-prepared film (that is, non-SVA) in **Figure 2b** illustrates the strong transmittance peaks of C=O stretching (1650 cm^{-1}), C-H stretching (2937 cm^{-1}), N-CH_3 (1397 cm^{-1}), C-CH_3 rocking (1014 cm^{-1}).[23, 24] This also includes the peaks associated with hydrogen bond of the added HI (1180-1360 cm^{-1})[25] and water (1634 cm^{-1})[26]. The final film shows no peaks for organic molecular, which demonstrates that this low-temperature SVA with post-annealing method removed all the solvent.

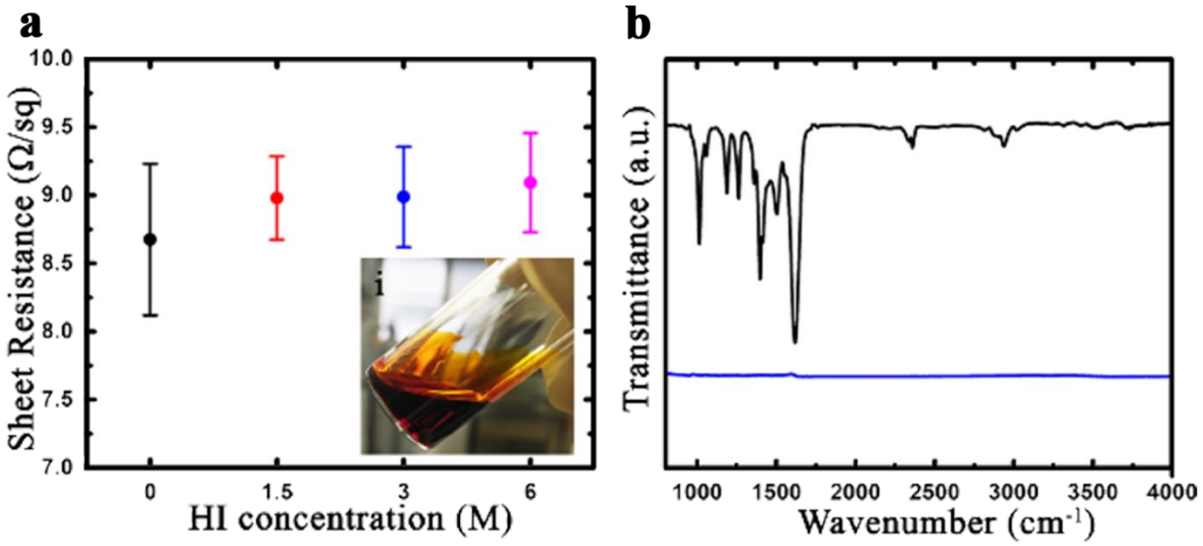

Figure 2. (a) Sheet resistance of FTO glasses after immerging the substrate in HI/DMA with different concentration of HI for 12 h. The inserted optical image is 0.7 M copper bismuth iodide solution in concentrated HI acid assisted DMA. (b) FTIR spectrum of the sample after one-step spin-coating precursor solution before SVA (black line) and sample dealt with SVA and the following post-annealing at 70 ^{0}C for 30 min.[33]

To precisely characterize the grown crystal grains, XRD patterns of $CuBiI_4$ films were measured. Fitting the experimental data to the calculated XRD pattern from reference cif file indicates a CuBiI4 film with cubic structure (space group Fd3m o2) with the lattice parameters of a = 12.134 Å. As shown in **Figure 3a,** X-ray diffraction spectra reveals the existence of high-index crystal planes as well as the low-index planes in [1, 1, 1] crystal direction with 2θ peaks at 12.8^0, 25.5^0, 38.6^0, 52.1^0, which are (1, 1, 1), (2, 2, 2), (3, 3, 3) and (4, 4, 4) crystal planes respectively. Low-index crystal phases processes very strong intensity and small full width at half maximum (FWHM) (0.10^0 for (1, 1, 1) and 0.15^0 for (2, 2, 2)). It also shows weak peak of (3, 1, 1) crystal plane at 24.4^0. Crystals were well arranged in [1 1 1] direction. The structure of $CuBiI_4$ crystal cell is illustrated using the computer program VESTA (**Figure 3b**).

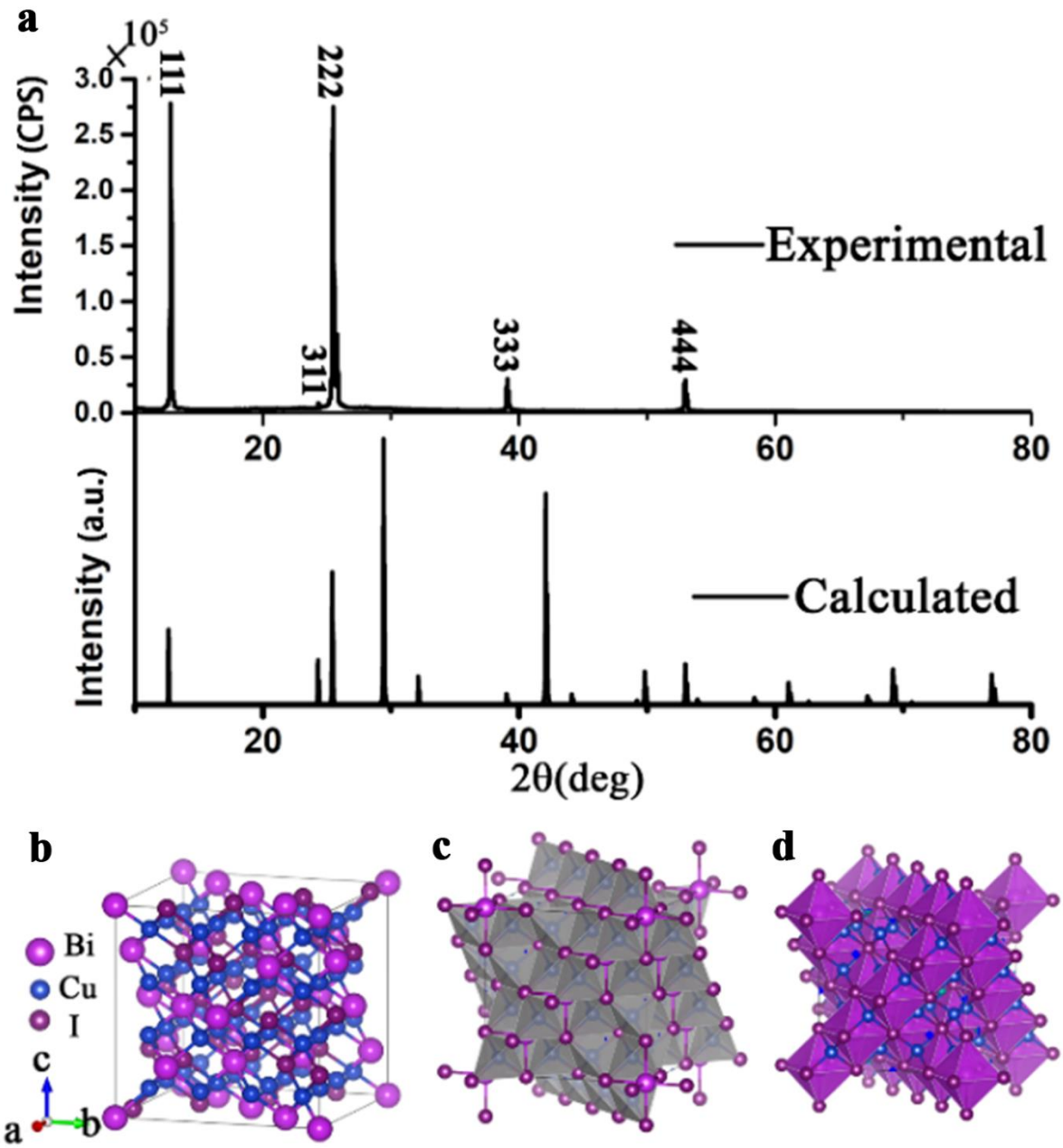

Figure 3. (a) Experiment and calculated XRD spectra from cif No.1123303 of $CuBiI_4$. (b) Schematic of crystal cell of $CuBiI_4$ with cubic structure and the dimensions (a= 12.134 Å). (c)-(d) Copper and bismuth ions are represented in polyhedral respectively.[33]

The unit cell of $CuBiI_4$ with the cubic structure is densely and symmetrically. Both copper and bismuth metal ion in the unit cell displays a polyhedron of iodides.[27] Copper is in the form of a cation of four-coordinated with the tetrahedral iodide groups and a bismuth cation is six-coordinated with the hexahedral iodide groups (**Figures 3c-3d**).

The absorbance increased with the increase of the precursor concentration as shown in **Figure 4a**. As shown in the Tauc plot from the UV absorbance spectrum (**Figure 4b**), we obtained an energy band gap (Eg) of 2.67 eV for $CuBiI_4$ assuming a direct band gap. In order to determine the energy band structure of $CuBiI_4$, photoelectron spectroscopy in air (PESA) was used to measure valence band energy (E_v) level (**Figure 4c**).

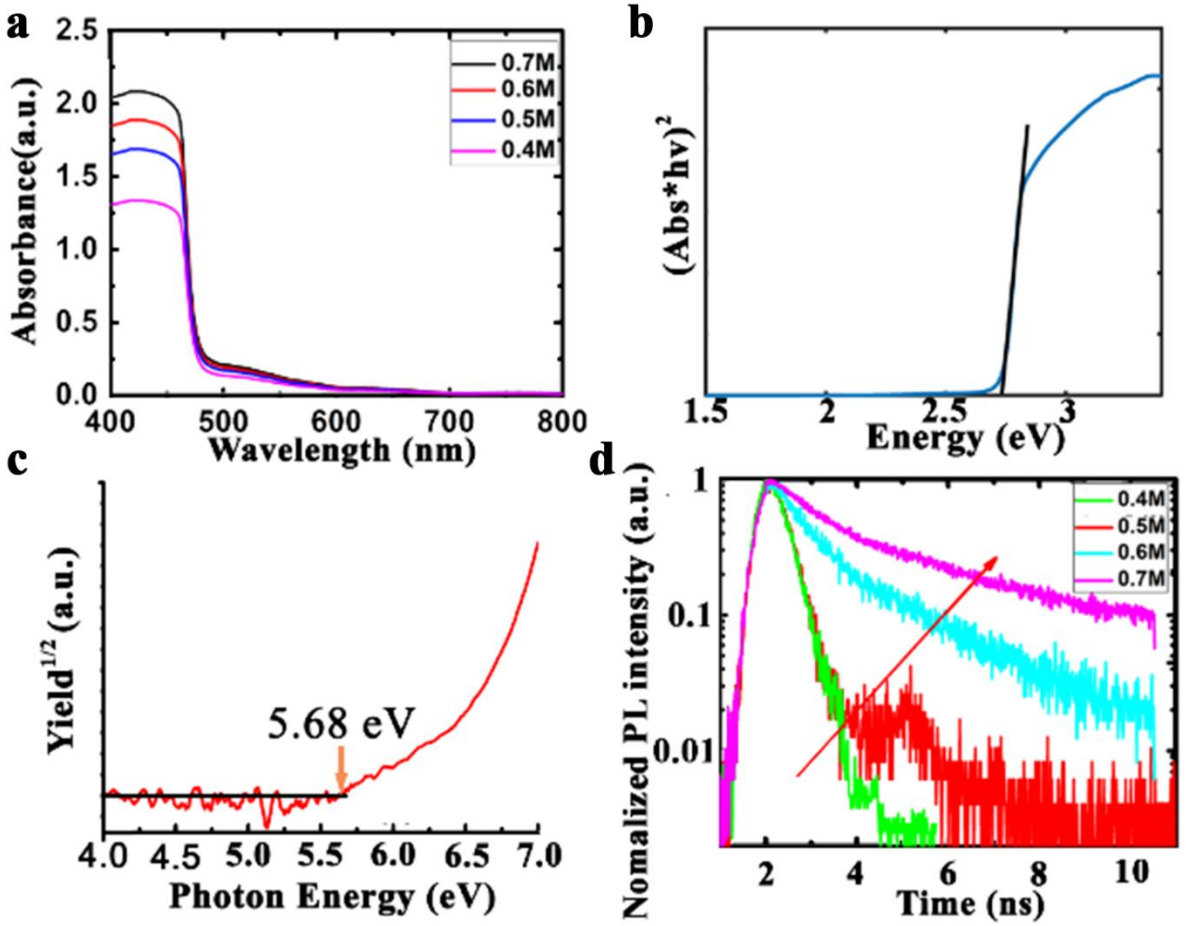

Figure 4. (a) UV/Vis spectra of copper bismuth iodide film. (b) Tauc plot from absorbance spectra. (c) Photon energy yield spectra in air. (d) PL decay curves of $CuBiI_4$ depending on varied precursor solution concentration.[33]

The spectrum shows that E_v is at -5.68 eV. The conduction band energy level was found to be about -3.01 eV estimated by the equation $E_g = E_v - E_c$. Additionally, as many other bismuth based active materials, such as silver bismuth iodide[16] and double perovskite $Cs_2AgBiBr_6$,[11] $CuBiI_4$ also presented weak indirect absorption from around 500 nm to 680 nm below the direct energy gap, which is mainly due to the involved change of momentum during the transition of carriers.

As shown in **Figure 5a**, the scanning electron microscopic (SEM) images illustrates a dense, uniform and pin-holes free copper bismuth iodide film with about 300nm size crystal grains at 0.7 M precursor solution concentration, which demonstrates that SVA after one-step spin-coating leaded to high quality crystals. **Table 1** shows that the average grain size increased with the concentration, which is consistent with the reported $MAPbI_3$ film dealt with SVA.[29] Precisely, the average grain size increased from 130 nm for 0.4 M to 300 nm for 0.7 M. Large grain size made the photoluminescence life time larger, which were obtained by the fitted stretch exponential decay function with curves (**Figure 4d**). As shown in Table 1, the obvious increase from 0.23 ns to the highest 3.03 ns at 0.7 M was observed, because of the smaller defect densities in the larger crystallites.[30]

Table 1. Average PL life time, grain size and thickness of $CuBiI_4$ as a function of concentration.[33]

Concentration (M)	0.4	0.5	0.6	0.7
Thickness (nm)	150	196	245	303
Average in-plane grain size (nm)	130	191	242	300
$\langle\tau\rangle$ (ns)	0.23028	0.823027	1.66747	3.03371

Table 2. Carrier mobility, carrier density and resistivity of $CuBiI_4$ as a function of precursor concentration.[33]

Concentration (M)	0.4	0.5	0.6	0.7
Carrier (cm^{-3})	2.47×10^{14}	5.75×10^{14}	6.03×10^{14}	6.56×10^{14}
Mobility (cm^2/Vs)	33.3	48.2	88.4	110
Resistivity (Ωcm)	7.59×10^{2}	2.25×10^{2}	1.17×10^{2}	0.862×10^{2}

Moreover, mobility and carriers density were also measured by Hall Effect. As shown in **Table 2**, hall mobility increase with the increase in precursor concentration. An excellent carrier mobility μ=110 cm^2/Vs was obtained. It demonstrates that gain size of copper bismuth iodide plays an important role in the carrier life time and mobility, which are beneficial for photovoltaic performance.

The energy band diagram of devices illustrates (**Figure 5b)** that the energy level for TiO_2 and Spiro-OmeTAD are suitable for $CuBiI_4$ as electron selective layer and hole transport layer respectively. When exposed to light, the generated electron-hole pairs inside absorber layer can be separated and transported in devices. Precisely, electrons are selectively injected from the conductive band of $CuBiI_4$ (E_c: -3.01 eV) into TiO_2 (E_c: -4.0 eV) and then collected by FTO electrode (E_c: -4.4 eV), meainwhile holes are selectively transported from valence band of $CuBiI_4$ to Spiro-OMeTAD and finally collected by gold electrode.[3, 28]

The structure of the device is composed of five layers including FTO, compact-TiO_2, mesoporous-TiO_2 with the filled $CuBiI_4$, Spiro-OMeTAD and gold electrode. The performance of devices is as a function of the concentration of the precursor solution (0.4-0.7 M). **Figure 5c** and **Figure 5d** illustrate the relationship between the power conversion efficiency (PCE) and the precursor concentration.

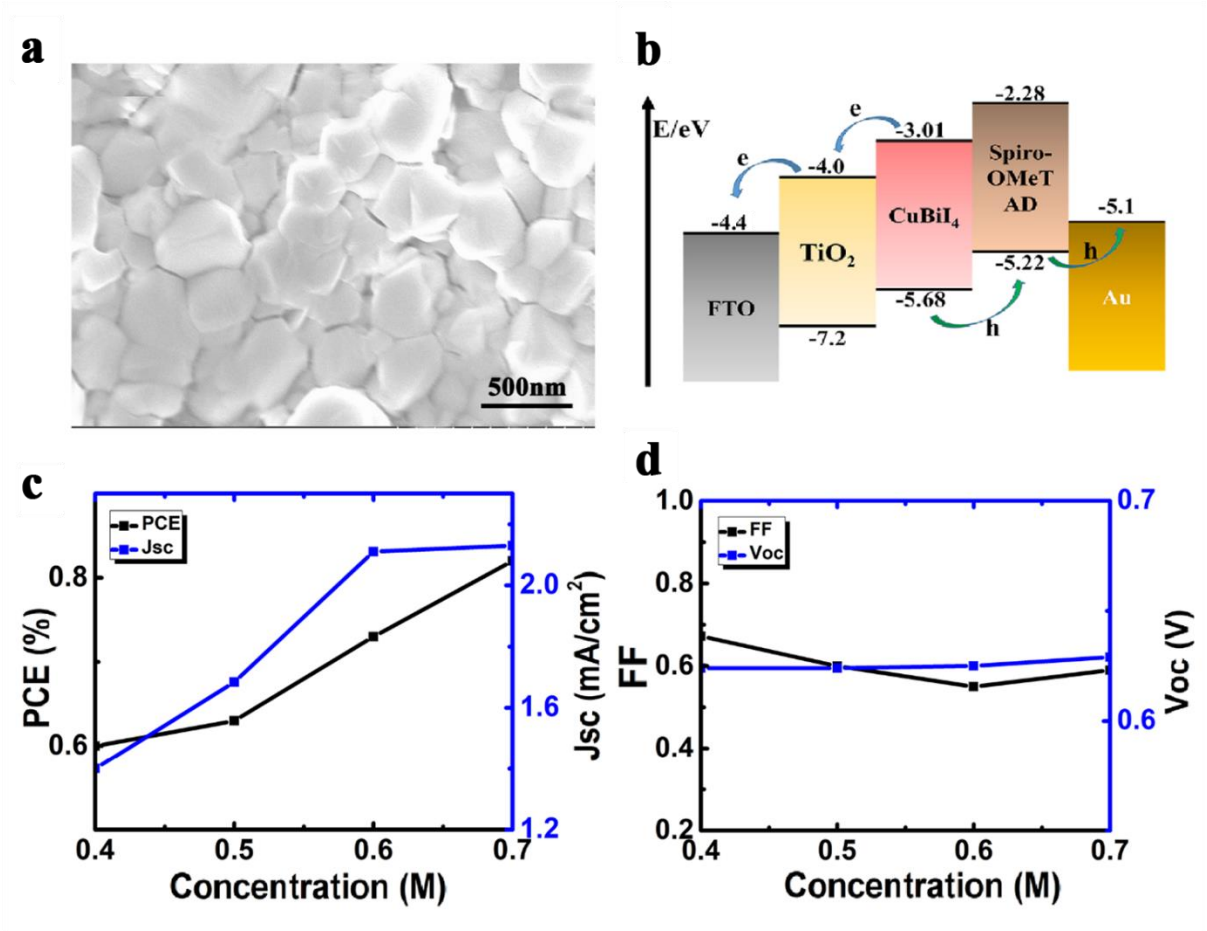

Figure 5. (a) SEM image of $CuBiI_4$ film and (b) Band structure of devices, mesoporous TiO_2, $CuBiI_4$ and FTO layers. Devices performance including (c) PCE, Jsc and (d) FF, Voc as a function of concentration of the precursor solution.[33]

The increase in PCE is mainly due to the enhancement of short-circuit current density (Jsc). Crystal size has great effect on the amount of generated electron-hole pairs when exposed to light. J-V curves in two scan modes (forward and reverse) with illumination at 1 Sun are shown in **Figure 6a**. During the measurement, devices were covered with mask with light exposure area of 0.12 cm^2. In forward scan mode (0V →0.7 V), the values of the Jsc, Voc and FF were found to be 2.19 mA/cm^2, 0.63 V and 0.57, respectively. In reverse scan mode (0.7 V → 0V), Jsc, Voc and FF were 2.17 mA/cm^2, 0.63 V and 0.59, respectively. The PCEs of the device in the forward as well as reverse scan mode were 0.82 % and 0.81 % respectively, which does not show obvious hysteresis phenomena reported frequently in the perovskite solar cells[31, 32]. The Incident Photon to Current Efficiency (IPCE) also emerged at about 465 nm wavelength, which closely supports the direct energy gap with 2.67 eV (**Figure 6b**).

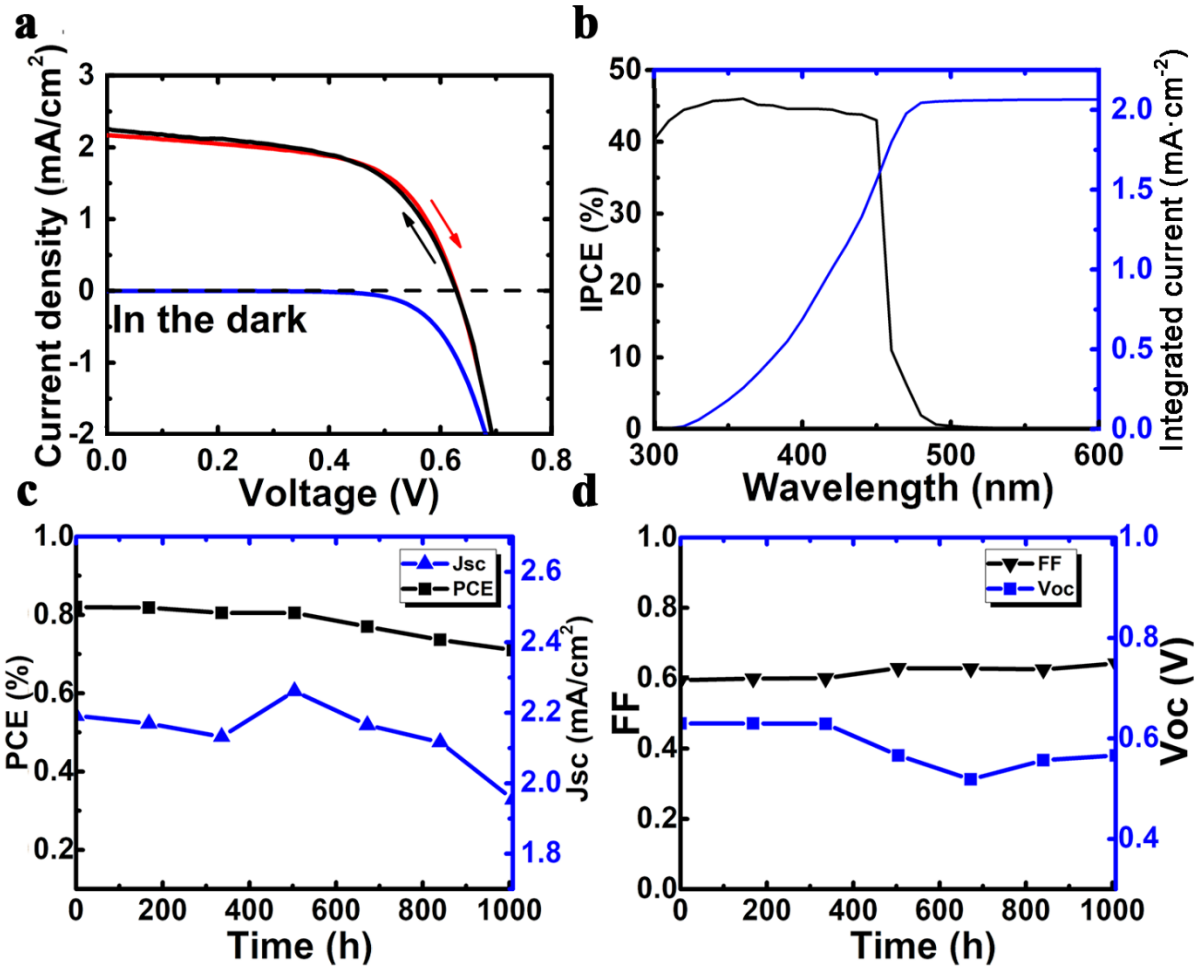

Figure 6. (a) J-V curve of $CuBiI_4$ device (using 0.7 M $CuBiI_4$ solution). (b) IPCE and integrated photocurrent of the devices. (c)-(d) Photovoltaic performance change during storage of devices.[33]

The integrated photocurrent density closely matched with the Jsc. The copper bismuth iodide with relatively wide energy gap (2.67 eV) possessed comparable efficiency of 0.82 % with other bismuth based material, which as well as the >40 % appreciable IPCE within the range 300-465 nm.

Finally, the operational stability were tested in ambient conditions with complete devices without encapsulation. Data were recorded every 168 hours. As shown in **Figure 6c** and **Figure 6d**, the PCE of devices maintaining 89 % level over 1008 hours showed an excellent stability. Since, $CuBiI_4$ film shows almost no degradation after such long-term storage in air, the mainly reason for the decrease of PCE may be the instability of Spiro-OMeTAD. Under encapsulation, more stable cell performance is expected.

5.3 Conclusions

Solution-processed copper bismuth iodide films were fabricated using a single-step spin-coating followed by SVA and post-annealing under low temperature. The HI acid assisted DMA solvent dissolved CuI and BiI_3 powder and made solution clear. To overcome the reported pinhole inside the final film, SVA was applied. These devices showed a very long-term stability under air atmosphere. X-ray diffraction spectrum illustrated the high-index facets as well as low-index facets in [1, 1, 1] direction, which demonstrates the high quality crystal grains. Also, the cubic crystal cell with lattice constant observed showed that both copper and bismuth ions are in the form with four-coordinated and six-coordinated of iodide respectively. The average grain size of $CuBiI_4$ increased with an increase in concentration of the precursor solution, which, greatly made PL life time longer from 0.23ns to 3.03 ns at 0.7 M and increased the carrier mobility to an appreciable value of 110 cm^2/Vs. We also notice that the concentration of precursor solution played an important role in the performance of devices by obviously increasing short-circuit current density.

The obtained 0.8 % efficiency is also comparable with those bismuth based solar cells recently reported. The novel preparation method on $CuBiI_4$, may provide a general method for other high quality light absorber films.

References

1. Burschka, J.; Pellet, N.; Moon, S.-J.; Humphry-Baker, R.; Gao, P.; Nazeeruddin, M. K.; Grätzel, M., Sequential deposition as a route to high-performance perovskite-sensitized solar cells. *Nature* **2013,** 499, (7458), 316-319.

2. Bach, U.; Lupo, D.; Comte, P.; Moser, J.; Weissörtel, F.; Salbeck, J.; Spreitzer, H.; Grätzel, M., Solid-state dye-sensitized mesoporous TiO2 solar cells with high photon-to-electron conversion efficiencies. *Nature* **1998,** 395, (6702), 583-585.

3. Hu, Z.; Kapil, G.; Shimazaki, H.; Pandey, S. S.; Ma, T.; Hayase, S., Transparent Conductive Oxide Layer and Hole Selective Layer Free Back-Contacted Hybrid Perovskite Solar Cell. *The Journal of Physical Chemistry C* **2017,** 121, (8), 4214-4219.

4. Jeon, N. J.; Lee, H. G.; Kim, Y. C.; Seo, J.; Noh, J. H.; Lee, J.; Seok, S. I., o-Methoxy substituents in spiro-OMeTAD for efficient inorganic–organic hybrid perovskite solar cells. *Journal of the American Chemical Society* **2014,** 136, (22), 7837-7840.

5. Dualeh, A.; Gao, P.; Seok, S. I.; Nazeeruddin, M. K.; Grätzel, M., Thermal behavior of methylammonium lead-trihalide perovskite photovoltaic light harvesters. *Chemistry of Materials* **2014,** 26, (21), 6160-6164.

6. Stoumpos, C. C.; Malliakas, C. D.; Kanatzidis, M. G., Semiconducting tin and lead iodide perovskites with organic cations: phase transitions, high mobilities, and near-infrared photoluminescent properties. *Inorganic chemistry* **2013,** 52, (15), 9019-9038.

7. Todorov, T. K.; Reuter, K. B.; Mitzi, D. B., High‐efficiency solar cell with earth‐abundant liquid‐processed absorber. *Advanced materials* **2010,** 22, (20).

8. Kumar, M. H.; Dharani, S.; Leong, W. L.; Boix, P. P.; Prabhakar, R. R.; Baikie, T.; Shi, C.; Ding, H.; Ramesh, R.; Asta, M., Lead‐free halide perovskite solar cells with high photocurrents realized through vacancy modulation. *Advanced Materials* **2014,** 26, (41), 7122-7127.

9. Sabba, D.; Mulmudi, H. K.; Prabhakar, R. R.; Krishnamoorthy, T.; Baikie, T.; Boix, P. P.; Mhaisalkar, S.; Mathews, N., Impact of Anionic Br– Substitution on Open Circuit Voltage in Lead Free Perovskite (CsSnI3-xBr x) Solar Cells. *The Journal of Physical Chemistry C* **2015,** 119, (4), 1763-1767.

10. Lehner, A. J.; Wang, H.; Fabini, D. H.; Liman, C. D.; Hébert, C.-A.; Perry, E. E.; Wang, M.; Bazan, G. C.; Chabinyc, M. L.; Seshadri, R., Electronic structure and photovoltaic application of BiI3. *Applied Physics Letters* **2015,** 107, (13), 131109.

11. Slavney, A. H.; Hu, T.; Lindenberg, A. M.; Karunadasa, H. I., A bismuth-halide double perovskite with long carrier recombination lifetime for photovoltaic applications. *Journal of the American Chemical Society* **2016,** 138, (7), 2138-2141.

12. Hoye, R. L.; Brandt, R. E.; Osherov, A.; Stevanović, V.; Stranks, S. D.; Wilson, M. W.; Kim, H.; Akey, A. J.; Perkins, J. D.; Kurchin, R. C., Methylammonium bismuth iodide as a lead‐free, stable hybrid organic–inorganic solar absorber. *Chemistry-A European Journal* **2016,** 22, (8), 2605-2610.

13. Park, B. W.; Philippe, B.; Zhang, X.; Rensmo, H.; Boschloo, G.; Johansson, E. M., Bismuth based hybrid perovskites A3Bi2I9 (A: methylammonium or cesium) for solar cell application. *Advanced Materials* **2015,** 27, (43), 6806-6813.

14. Xiao, Z.; Meng, W.; Mitzi, D. B.; Yan, Y., Crystal Structure of AgBi2I7 Thin Films. *The Journal of Physical Chemistry Letters* **2016,** 7, (19), 3903-3907.

15. Leng, M.; Chen, Z.; Yang, Y.; Li, Z.; Zeng, K.; Li, K.; Niu, G.; He, Y.; Zhou, Q.; Tang, J., Lead-Free, Blue Emitting Bismuth Halide Perovskite Quantum Dots. *Angewandte Chemie International Edition* **2016,** 55, (48), 15012-15016.

16. Kim, Y.; Yang, Z.; Jain, A.; Voznyy, O.; Kim, G. H.; Liu, M.; Quan, L. N.; García de Arquer, F. P.; Comin, R.; Fan, J. Z., Pure Cubic‐Phase Hybrid Iodobismuthates AgBi2I7 for Thin‐Film Photovoltaics. *Angewandte Chemie International Edition* **2016,** 55, (33), 9586-9590.

17. Zhu, H.; Pan, M.; Johansson, M. B.; Johansson, E. M. J., High Photon-to-Current Conversion in Solar Cells Based on Light-Absorbing Silver Bismuth Iodide. *ChemSusChem* **2017,** 10, (12), 2592-2596.

18. Lehner, A. J.; Fabini, D. H.; Evans, H. A.; Hébert, C.-A.; Smock, S. R.; Hu, J.; Wang, H.; Zwanziger, J. W.; Chabinyc, M. L.; Seshadri, R., Crystal and Electronic Structures of Complex Bismuth Iodides A3Bi2I9 (A= K, Rb, Cs) Related to Perovskite: Aiding the Rational Design of Photovoltaics. *Chem. Mater* **2015,** 27, (20), 7137-7148.

19. Gu, M.; Gao, P.; Liu, X. L.; Huang, S. M.; Liu, B.; Ni, C.; Xu, R. K.; Ning, J. M., The influence of concentration and supersaturation ratio of CuI· HI on CuI crystal growth by decomplexation method. *Crystal Research and Technology* **2010,** 45, (4), 365-370.

20. Heo, J. H.; Song, D. H.; Han, H. J.; Kim, S. Y.; Kim, J. H.; Kim, D.; Shin, H. W.; Ahn, T. K.; Wolf, C.; Lee, T. W., Planar CH3NH3PbI3 perovskite solar cells with constant 17.2% average power conversion efficiency irrespective of the scan rate. *Advanced Materials* **2015,** 27, (22), 3424-3430.

21. Gholamkhass, B.; Servati, P., Solvent–vapor induced morphology reconstruction for efficient PCDTBT based polymer solar cells. *Organic Electronics* **2013,** 14, (9), 2278-2283.
22. Wessendorf, C. D.; Schulz, G. L.; Mishra, A.; Kar, P.; Ata, I.; Weidelener, M.; Urdanpilleta, M.; Hanisch, J.; Mena‐Osteritz, E.; Lindén, M., Efficiency Improvement of Solution‐Processed Dithienopyrrole‐Based A‐D‐A Oligothiophene Bulk‐Heterojunction Solar Cells by Solvent Vapor Annealing. *Advanced Energy Materials* **2014,** 4, (14).
23. Verbovy, D. M.; Smagala, T. G.; Brynda, M. A.; Fawcett, W. R., A FTIR study of ion-solvent interactions in N,N-dimethylacetamide. *Journal of Molecular Liquids* **2006,** 129, (1), 13-17.
24. Konstantatos, G.; Howard, I.; Fischer, A.; Hoogland, S.; Clifford, J.; Klem, E.; Levina, L.; Sargent, E. H., Ultrasensitive solution-cast quantum dot photodetectors. *Nature* **2006,** 442, (7099), 180-183.
25. Zhu, C.; Tsuge, M.; Räsänen, M.; Khriachtchev, L., Experimental and theoretical study of the HXeI··· HCl and HXeI··· HCCH complexes. *The Journal of chemical physics* **2015,** 142, (14), 144306.
26. Mojet, B. L.; Ebbesen, S. D.; Lefferts, L., Light at the interface: the potential of attenuated total reflection infrared spectroscopy for understanding heterogeneous catalysis in water. *Chemical Society Reviews* **2010,** 39, (12), 4643-4655.
27. Fourcroy, P.; Carre, D.; Thevet, F.; Rivet, J., Structure du tétraiodure de cuivre (I) et de bismuth (III), CuBiI4. *Acta Crystallographica Section C: Crystal Structure Communications* **1991,** 47, (10), 2023-2025.
28. Xiao, Z.; Dong, Q.; Bi, C.; Shao, Y.; Yuan, Y.; Huang, J., Solvent Annealing of Perovskite-Induced Crystal Growth for Photovoltaic-Device Efficiency Enhancement. *Advanced Materials* **2014,** 26, (37), 6503-6509.
29. D'Innocenzo, V.; Srimath Kandada, A. R.; De Bastiani, M.; Gandini, M.; Petrozza, A., Tuning the Light Emission Properties by Band Gap Engineering in Hybrid Lead Halide Perovskite. *Journal of the American Chemical Society* **2014,** 136, (51), 17730-17733.
30. Ye, M.; He, C.; Iocozzia, J.; Liu, X.; Cui, X.; Meng, X.; Rager, M.; Hong, X.; Liu, X.; Lin, Z., Recent advances in interfacial engineering of perovskite solar cells. *Journal of Physics D: Applied Physics* **2017,** 50, (37), 373002.
31. Meloni, S.; Moehl, T.; Tress, W.; Franckevičius, M.; Saliba, M.; Lee, Y. H.; Gao, P.; Nazeeruddin, M. K.; Zakeeruddin, S. M.; Rothlisberger, U., Ionic polarization-induced

current–voltage hysteresis in CH3NH3PbX3 perovskite solar cells. *Nature communications* **2016,** 7, 10334.

32. Unger, E.; Hoke, E.; Bailie, C.; Nguyen, W.; Bowring, A.; Heumüller, T.; Christoforo, M.; McGehee, M., Hysteresis and transient behavior in current–voltage measurements of hybrid-perovskite absorber solar cells. *Energy & Environmental Science* **2014,** 7, (11), 3690-3698.

33. Hu, Z.; Wang, Z.; Kapil, G.; Ma, T.; Iikubo, S.; Minemoto, T.; Yoshino, K.; Toyoda, T.; Shen, Q.; Hayase, S., Solution‐proceed Air‐stable Copper Bismuth Iodide $CuBiI_4$ for Photovoltaics. *ChemSusChem* **2018**, doi:10.1002/cssc.201800815.

General conclusions

In this thesis, the harvesting layer of devices were optimized in three different ways including incorporation mesoporous Ti electrode, hetero-dimer plasmon and using bismuth copper iodide material with the aim of reducing the cost and toxic lead, which are environment friendly and beneficial for commercial application.

The incorporation of mesoporous Ti electrode enabled the effective TCO less back-contacted SCs with 3.9 % efficiency, in which the native oxide on the Ti surface immediately made a role of selective electron collection, while the filled perovskite crystal inside porous Ti paved the way to transport holes, which were finally collected by back electrode. This architecture avoided the transmission loss caused by TCO, and showed a long-term stability. The formation of network-like porous Ti electrode. This was accomplished by sputtering Ti on TiO_2 layer with bigger particle size.

Ultralthin perovskite layer with the embedded silver-gold hetero-dimer greatly enhanced the absorption especially within the range 550-800 nm. The 150 nm thickness perovskite with Ag-Au NPs was comparable with the absorption of perovskite with 350 nm thickness. Perovskite film with the hetero-dimer processed higher light absorption than that with homo-dimers, because of the both radiation effect in the ends area and the strongly enhanced optical field localized in junction area. It overcame the vanished σ^* mode of homo-dimers. About 28.15 % improvement of light-harvesting of perovskite embedded hetero-dimer compared to the reference film were obtained, which was higher than the reported 10 % of homo-dimers. In addition, thin silica shell of dimer was recommended, because of the confinement effect. These results provide a significant meaning to further optimize the optical property of devices and also reduce the amount of absorbing material, especially to reduce the toxicity of lead in perovskite-based devices.

The non-toxic bismuth based metal halide material were prepared to replace the toxic lead based material. X-ray diffraction spectrum illustrated the high-index facets as well as low-index facets in [1, 1, 1] direction, which demonstrated the high quality crystal grains. High concentration of the precursor solution increased the average grain size, which meanwhile, greatly enlarged PL life time and carrier mobility. The concentration of the precursor solution played an important role in the performance of devices by increasing short-circuit current density. These devices showed very long-term stability under air atmosphere.

These studies on the harvesting layer of metal halide SCs may provide a great meaning in the future economic, non-toxic SCs with high performance.

Future prospects

The future studies on the active layers to further reduce the cost of device and overcome the toxic lead in conventional perovskite SCs may be focused on the following three aspects.

The possibility of incorporation of high conductivity porous metal electrode such as Zn instead of Ti could further improve the power conversion efficiency. The native oxide (ZnO), which has higher mobility than TiO_2, may enhance the extraction of the generated electrons and reduce the carriers recommendation rate. Due to the directly exposed to light without the energy loss by TCO, the high photovoltaic performance could be expected.

To reduce the thickness of $MAPbI_3$ layer and realize the ultralthin devices, the recent colloidal technology opens up new opportunities for a possible low-cost and easy preparation method. Metal dimers can be synthesized by colloidal approach in buffer solution, in which gap distance can be tuned by changing the length of conjugated molecular (ss-DNA), and silica shell can be introduced by adding a silane coupling agent (e.g. 3-aminopropyltrimethoxysilane, APS). Random hetero-dimer with silica shell may can be dispersed on substrate and the space will be filled with perovskite by spin-coating.

The completely replacement of lead-base metal halide material depends on the improvement of efficiency of non-toxic bismuth based materials. Relatively low bandgap by developing other possible cation in bismuth based materials is needed to overcome the lack of absorption for long wavelength.

Achievements

Journal Publications：

1. **Zhaosheng Hu**, Gaurav Kapil, Hiromitsu Shimazaki, Shyam Sudhir Pandey, Tingli Ma, Shuzi Hayase, Transparent Conductive Oxide Layer and Hole Selective Layer Free Back-Contacted Hybrid Perovskite Solar Cell. ***The Journal of Physical Chemistry C*** 121, 4214-4219 (2017).

2. **Zhaosheng Hu,** Tingli Ma, Shuzi Hayase, Interparticle coupling effect of silver-gold heterodimer to enhance light harvesting in ultrathin perovskite solar cell. ***Journal of Photonics for Energy*** 8(1), 015502 (2018).

3. **Zhaosheng Hu**, Zhen Wang, Gaurav Kapil, Tingli Ma, Satoshi Iikubo, Takashi Minemoto, Kenji Yoshino, Taro Toyoda, Qing Shen and Shuzi Hayase. Solution-proceed Air-stable Copper Bismuth Iodide $CuBiI_4$ for Photovoltaics. ***ChemSusChem,*** doi:10.1002/cssc.201800815.

Conferences:

1. 2016 The 26th Annual Meeting of MRS-J (in oral, title: Fabrication of TCO-less hybrid perovskite solar cell)

2. 2016 The 77th JSAP Autumn Meeting (in oral, title: Fabrication of TCO-less hybrid perovskite solar cell)

Acknowledgements

First and foremost, I am very grateful to my supervisor, **Prof. Shuzi Hayase**, for selecting me to study in my favorite research under his extreme kind supervision. His great kindness and great help motive the whole progress of the research.

At the same time, I am extremely thankful to Prof. Tingli Ma for her precious suggestions, comments regarding my research work. I am greatly thankful to Prof. Shyam S. Pandey for his suggestion of my research.

I sincerely thank Dr. Teresa and Dr. Yuhei Ogomi for their advices during my research.

I would like to thank Dr. Kapil, Dr. Nishimura, Dr. Suvratha Krishnamurthy, Mr. Pandey, Mr. Nam, Mr. Atul, Miss. Anusha, Mr. Wang, Mr. Zhang, Mr. Yang, Mr. Hamada, Mr. Sannoe, Ito San, Kawano San, Sato San, Hoshiba San, Yamaguchi San, Yamasuso San, Shifumi San for their help and support.

I would like to thank all the members of Hayase, Pandey & Ma lab, all the staffs members and students of K.I.T., who directly or indirectly help me for my life or my research in Japan.

I give my grateful thanks to all the professors and the staffs in other universities, who give their help for my experiments during my research.

Finally, I would like to give my special thanks to all my beloved family, my girlfriend and friends for their continued encouragement and support for my achievement in my life.